Experimental Study of the Role of Grain Size

in Erosion of Bedrock Channels by Abrasion

by

Mark Adams

A Thesis Presented in Partial Fulfillment
of the Requirements for the Degree
Master of Science

Approved November 2016 by the
Graduate Supervisory Committee:

Kelin Whipple, Chair
Arjun Heimsath
Mark Schmeeckle

ARIZONA STATE UNIVERSITY

December 2016

ABSTRACT

The morphology of mountainous areas is strongly influenced by stream bed incision rates, but most studies of landscape evolution consider erosion at basin scales or larger. The research here attempts to understand the smaller-scale mechanics of erosion on exposed bedrock channels in the conceptual framework of an established saltation-abrasion model by Sklar and Dietrich [2004]. The recirculating flume used in this experiment allows independent control of bed slope, water discharge rate, sediment flux, and sediment grain size – all factors often bundled together in simple models of river incision and typically cross-correlated in natural settings. This study investigates the mechanics of erosion on exposed bedrock channels caused by abrasion of transported particles. Of particular interest are saltating particles, as well as sediment near the threshold between saltation and suspension - sediment vigorously transported but with significant interaction with the bed. The size of these erosive tools are varied over an order of magnitude in mean grain diameter, including a sand of D_{50} = 0.56 mm, and three gravel sizes of 3.39, 4.63, and 5.88 mm. Special consideration was taken to prevent any flow conditions that created a persistent alluvial cover. The erodible concrete substrate is fully exposed at all times during experiments reported here. Rates of erosion into the concrete substrate (a bedrock proxy) were measured by comparing topographic data before and after each experimental run, made possible by a precision laser mounted on a high speed computer-controlled cart. The experimental flume was able to produce flow discharge as high as 75 liters per second, sediment fluxes (of many varieties) up to 215 grams per second, and bed slopes up to 10%. I find a general positive correlation is found between erosion rate and bed slope, shear stress, grain size, and sediment flux.

TABLE OF CONTENTS

LIST OF FIGURES

CHAPTER 1: INTRODUCTION

The study of stream bed erosion is important because fluvial channels set the boundary condition on all hill slopes and control the shape and structure of many landscapes. In addition, there is great recent interest in the degree of coupling among erosion rates, climate, and tectonics [Whipple 2009]. Larger-scale studies of landscape evolution typically use a stream-power model, where erosion rates are theorized as a function of slope and drainage area (larger catchment area = increased water discharge rates). These models do not account for possible independently varying controls on erosion, including; channel slope, bed roughness, rock strength, bedrock exposure, sediment flux, grain size, channel width, or the dominant process driving erosion [Sklar and Dietrich, 2004; Whipple 2004]. There are many physical processes by which exposed bedrock channels may be incised (e.g., plucking, cavitation, and abrasion), but the scope of this study is restricted to conditions that lead to a dominance of abrasion by saltating sediment (Sklar and Dietrich, 2004).

With independent control over many variables of the flow regime, the flume is capable of determining whether and how erosion rates may change with increases in shear stress, water discharge, and sediment flux across a wide range of grain sizes. The experiments were set up to test predictions of the saltation-abrasion model of *Sklar and Dietrich* [2004] and further explore interpretations of earlier experimental results (Johnson et al., 2010). Tensile strength of the substrate is measured to gauge the substrate's resistance to abrasion by saltating grains, following Sklar and Dietrich (2001). Although this study relates to erosion controls in bedrock channels, the size of the flume and desired run time of each erosion experiment makes the use of real rock unfeasible. The bedrock proxy used is a weak concrete mix that allows measurable rates in experimental runs lasting only 15 minutes.

Experimental conditions were selected to minimize any sediment cover on the bed. As soon as a solid particle enters the stream system (such as from the adjacent hillside) it is immediately transported downstream. This detachment-limited environment is required to study the effect of varying slope, discharge, and shear stress on erosion independent of the complicating factor of partial bed cover. This environment contrasts with the more typical transport-limited environment, where alluvial cover persists on the river bed until an infrequent flood event can transport that material. The saltation-abrasion model of *Sklar and Dietrich* [2004] predicts that erosion rates increase with increases in grain size, all else held equal, until grain sizes become large enough that deposition begins. As these grains start covering the stream bed, abrasion of the bed is reduced and erosion decreases in their model. Similar effects are anticipated as flow discharge, bed slope, and shear stress decrease. In order to simplify this problem, experimental conditions were chosen in the attempt to avoid, and test for, any influence of partial sediment cover on the bed.

The process by which this specific process of erosion occurs is explained by the saltation-abrasion model, where the bedrock channel is eroded by the impact force of particles bouncing downstream. As a useful indicator of flow intensity, basal shear stress (τ_b) is, in the ideal conditions of a steady, uniform flow (no flow acceleration or flow variance), measured as the product of fluid density, gravitational acceleration, water depth, and bed slope – ρghS. The transport process (suspension or saltation) of the bedload particles is determined by the Rouse number that relates near-bed shear stress and particle settling velocity, and backed by observations of particle impact angle and velocity that preceded the erosion experiments [Chatanantavet et al., 2013].

Grain sizes used in the experiments ranged over an order of magnitude in size and were chosen from durable quartz source to minimize wear of the transported particles themselves. The median grain size diameter (D_{50}) for the saltating bedload particles was selected as 3.39 mm, 4.63 mm, and 5.88 mm. A sand of D_{50} = 0.56 mm was also included to assess erosion done by particles near the transition to suspension.

Given the same flow conditions and sediment flux, the role of grain size in the rate of erosion depends on how these differently-sized particles impact the bed. Important considerations include the competition between the amount of energy transferred during each particle impact on the concrete bed, and how frequently those collisions occur.

CHAPTER 2: BACKGROUND

Modes of sediment transport were observed on a Plexiglas bed (no concrete), but it is useful to categorize this motion as a function of flow conditions. *Chatanantavet et al.* [2013] studied saltation dynamics over a smooth, hard bed, including measurements of hop length, hop height, impact angle, and impact velocity. Each of these traits are affected by discharge rate and bed slope, but it is also theorized that bed roughness plays a strong role in that local impact angle influences how efficiently the kinetic energy of a saltating particle is transferred to the bed surface [Johnson and Whipple, 2010].
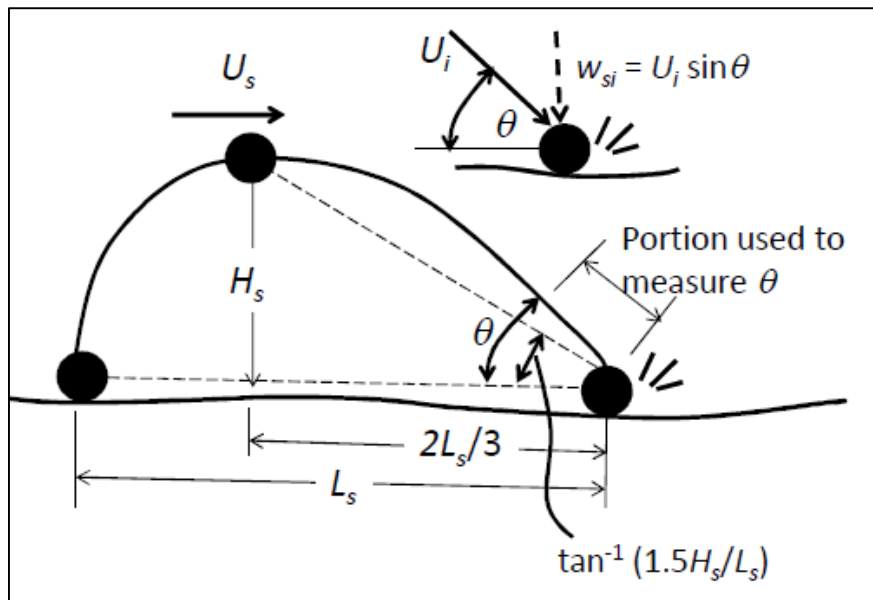
Figure 1: Saltation trajectory and important vector components [Chatanantavet 2008]

For the saltation-abrasion model of *Sklar and Dietrich* [2004], particles abrade the bed surface by rolling, sliding, or hopping (saltation), and defined by flow conditions through a Rouse number above 2.5. Rouse numbers are calculated as a ratio between a particles setting velocity and the shear velocity of the flow [Eq. 1]. In observations of our flow conditions (without a concrete bed for visual clarity), it was apparent that most sediment of our range of sizes will move downstream via

saltation. For a Rouse number between 2.5 to 1.2, 50% of particles are suspended. Only between values of 1.2 to 0.8 can all sediment be defined as in suspension. Below this range, the particles are considered wash load and no longer interact with the bed surface. The definition of the Rouse number (P) is:

$$P = \frac{\omega_s}{\kappa\, u_*} \qquad (1)$$

Here ω_s is particle settling velocity, k is the von Karman constant (0.4), and u* is shear velocity. For this experiment, settling velocity was calculated following *Dietrich [1983].* In simple terms, settling velocity is a function of gravitational acceleration, mean grain diameter, water viscosity, and constants that describe the shape and smoothness of the grains (e.g., sphericity and roundness).

Following *Sklar and Dietrich* [2004] and *Sklar and Dietrich* [2008], the basic formula for erosion in a bedrock channel can be expressed as:

$$E = V_i\, I_r\, F_e \qquad (2)$$

V_i is the average volume of bed detached per particle impact and I_r is the frequency of particle impacts per area. F_e, the fraction of the bed surface not covered by alluvium, is not generally considered in this study since all flow conditions planned in this study were chosen to disallow any alluvial cover ($F_e = 1$). We test this assumption as noted below. V_i is further elaborated by Sklar and Dietrich [2004] as:

$$V_i = \frac{1}{2}\frac{Vp\,\rho_s\,\omega i^{\,2}}{\varepsilon v} = \frac{1}{2}\frac{\pi\rho_s R_b g D_s^{\,4} Y}{9.4 k_v \sigma_T^{\,2}}\left(\frac{\tau^*}{\tau_c^*}-1\right)^{0.36} \qquad (3)$$

Equation 3 covers variables of the *type* of sediment used, as v_p, ρ_s, and ω_i represent the particle volume, density, and impact velocity normal to the bed surface, respectively, and ε_v is kinetic energy required to erode a unit volume of bedrock.

Particle impact velocity normal to the bed (ω_i) is expressed below in Equation 4 as mean descent velocity (ω_d), which should scale with vertical impact velocity. In

Equation 4, H_s is mean saltation hop height, L_s is mean saltation hop length, Us is mean saltation velocity of grains, R is the submerged specific gravity of those grains, g is gravitational acceleration τ^* is dimensionless bed shear stress, τ^*_c is critical dimensionless shear stress for initial motion of grains, u^* is shear velocity ($u^* = \sqrt{\tau_b/\rho}$), in which τ_b is bed shear stress and ρ is water density), and w_f is particle settling velocity. Note that if shear stress does not exceed the critical shear stress, particle motion on the bed does not occur. Similarly, if shear velocity exceeds particle settling velocity those particles become suspended within the flow.

$$\omega_d = \frac{3H_sU_s}{L_s} = 0.4\sqrt{RgD}\left(\frac{\tau^*}{\tau^*_c} - 1\right)^{0.18}\left(1 - \left(\frac{u^*}{\omega_f}\right)^2\right)^{1/2} \qquad (4)$$

Also, according to Equation 4, increases in impact velocity of sediment (and therefore increases in erosion) are positively correlated with changes in saltation hop height, mean particle velocity, specific gravity of submerged saltation particles, diameter of spherical saltation particles, and negatively correlated with changes in saltation hop length and fall velocity of submerged saltation grains. With increasing grain size, it can be expected that a decrease in saltation length (as particles move further from conditions that allow suspension) and therefore an increase in erosion rates, in addition to the fact that mean descent velocity increases with the square root of grain size diameter.

The resistance to erosion of the bed by these particles is factored into ε_v; a value of kinetic energy required to erode a unit volume of the bedrock (Equation 5). Here, σ_T and Y represent the tensile strength and Young's modulus of elasticity of the bedrock material.

$$\varepsilon_v = k_v \frac{\sigma_T{}^2}{Y} \qquad (5)$$

The dimensionless k_v was used by Sklar and Dietrich [2006] as a coefficient on the order of 10^6. This experiment measured representative samples of the concrete "bedrock" for tensile strength further covered in the lab design section.

The other relevant factor to the original erosion Equation 2, the frequency of particle impacts per area, is defined as:

$$I_r = \frac{q_s}{V_p L_b} = \frac{3q_s}{4\pi \rho_s D_s^4}\left(\frac{\tau^*}{\tau_c^*} - 1\right)^{-0.88} \qquad (6)$$

In Equation 6, q_s represents the mass flux of sediment per unit channel width (travelling as bed load), and L_b is the hop length of those saltating particles. Note that *Sklar and Dietrich [2004]* state that erosion is proportional to mass sediment flux (q_s) in bed conditions without alluvial cover and was later given experimental confirmation [Johnson 2010].

$$F_e = \left(1 - \frac{q_s}{q_t}\right) = \left(1 - \frac{q_s}{5.7\rho_s(R_b g D_s^3 \tau_c^{*3})^{0.5}}\right) \qquad (7)$$

In Equation 7, the fraction of bedrock exposed (F_e) introduces the mass bed load sediment transport capacity per unit channel width, q_t [Sklar et al., 1996; Slingerland et al., 1997; Sklar and Dietrich, 2004]. Flow conditions used for experiment runs in this study were selected on the basis that they would not allow any alluvial cover, and so F_e can be ignored as long as sediment transport capacity stayed significantly higher than sediment flux ($F_e \sim 1$).

The equation for erosion from Equation 2 can then be represented below as Equation 8 to more clearly show all quantified factors contributing to erosion:

$$E = \frac{\rho_s q_s \omega_i^2 Y}{L_b k_v \sigma_T^2}\left(1 - \frac{q_s}{q_t}\right) = \frac{0.08 R_b g Y}{k_v \sigma_T^2} q_s \left(\frac{\tau^*}{\tau_c^*} - 1\right)^{-0.5}\left(1 - \frac{q_s}{q_t}\right) \qquad (8)$$

In general, then, increases in sediment particle density, sediment flux, or saltation impact velocity (normal to the bed surface) are predicted to increase rates or erosion, where increases in saltation hop length, tensile strength of the bed substrate, or the ratio of sediment flux to transport capacity are expected to

7

decrease erosion rates. For each controlled experiment in the flume, many of these factors collapse into a single coefficient to terms describing shear stress, sediment flux, and bedrock exposure (Equation 9). As a result, the analysis of experiments can be greatly simplified when comparing experiments of the same grain size and sediment flux rate because other than confirming the bed is free from alluvial cover, shear stress (in excess of what is required for transport initiation) is the only remaining control on erosion rate:

$$E = K\, q_s \left(1 - \frac{q_s}{q_t}\right)\left(\frac{\tau^*}{\tau_c^*} - 1\right)^{-0.5} \tag{9}$$

According to this simplified equation, on a smooth bed free from alluvial cover, the saltation-abrasion model predicts that erosion rates will decrease as shear stress increases [Fig. 2]. This can be observed in Eq. 9 as the "excess shear stress" term $\left(\frac{\tau^*}{\tau_c^*} - 1\right)$ raised to a negative ½ power. Furthermore, this same term predicts that there must be an increase in erosion rates with increasing grain sizes (with shear stress constant), as this will cause τ_c^* to increase [Fig. 3]. With these concepts in mind, erosion experiments can be designed to test this theory by varying conditions affecting τ^* (bed slope, discharge) as well as τ_c^* (grain size, bed roughness).
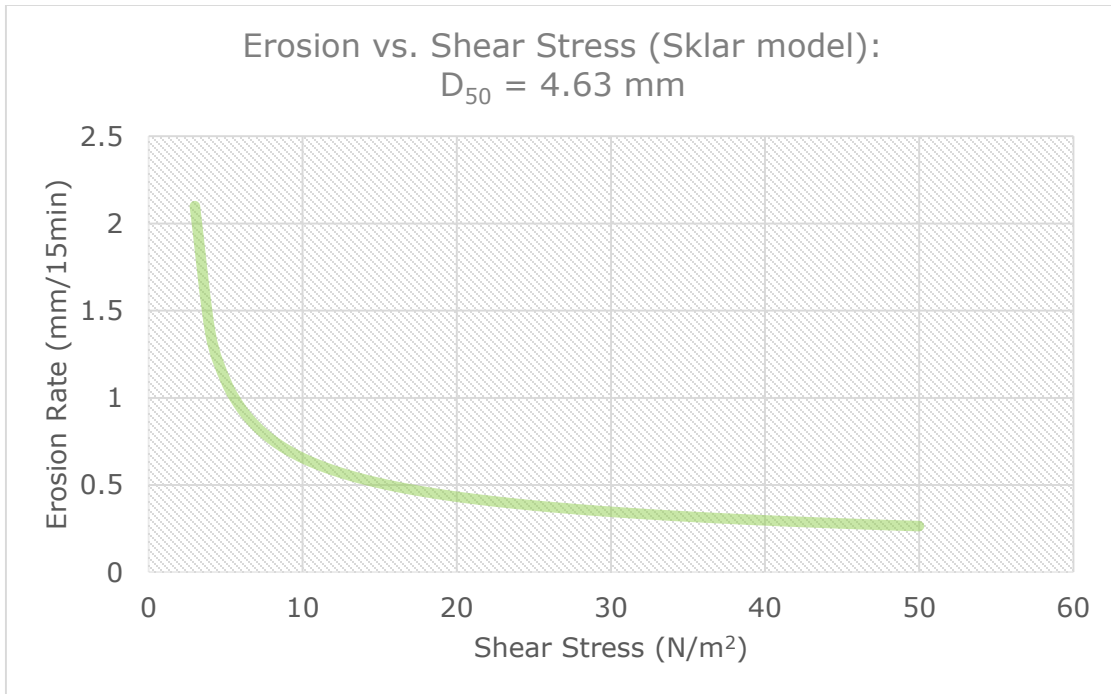
Figure 2: Erosion vs. shear stress according to the saltation-abrasion model of Sklar and Dietrich [2004], using sediment of D_{50} = 4.63 mm.
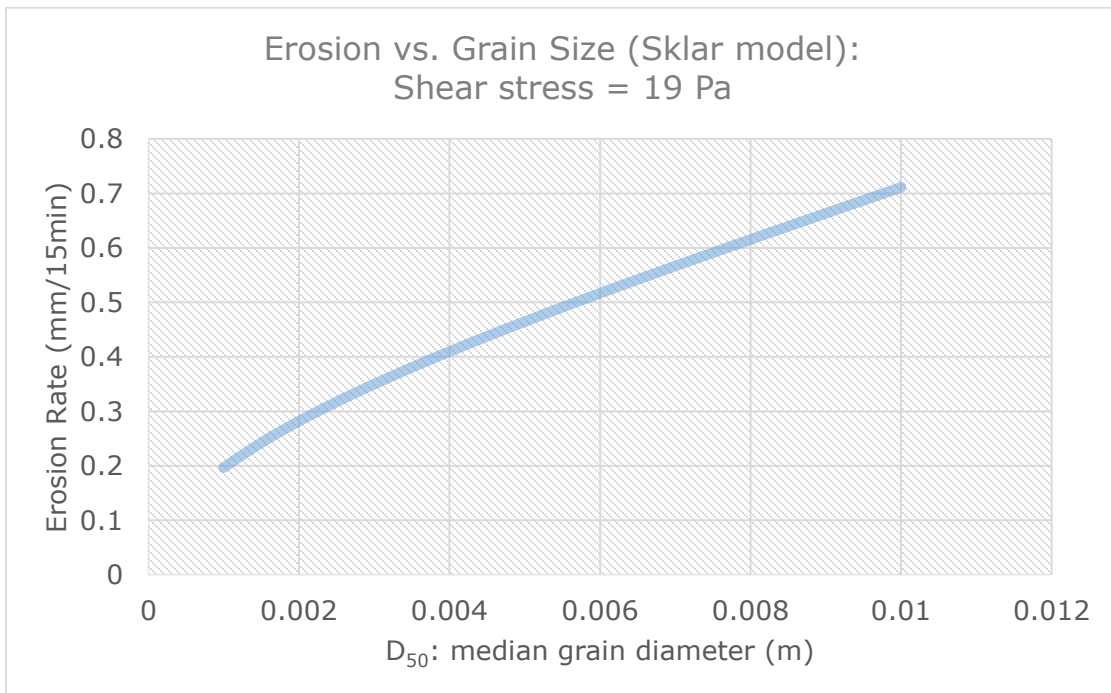
Figure 3: Erosion vs. median grain diameter (D_{50}) according to the saltation-abrasion model of Sklar and Dietrich [2004], using shear stress value constant at 19 N/m^2.

CHAPTER 3: METHODS

3.1: Lab Design

The experimental setup considers erosion of a weak concrete substrate by various sizes of sediment grains in transport. The experiment is designed so that a 3 meter long concrete insert is placed within an approximately 5 meter long, 0.45 meter wide recirculating flume [Fig. 2]. The removable inserts measuring 3 m long by 0.30 m width are placed within the flume, after being previously filled with concrete to a thickness of 0.15 m. In between the concrete insert and the upstream water source is another insert of length 1.5 m containing a smooth, plastic floor matching the 0.15 m height of the concrete, and this allows for a smooth transition between the upstream head box and the test area downstream. Additionally, this buffer zone allows for bedload particles (dropped from the above sediment hopper) to uniformly distribute before being transported along the erodible bed. Downstream of these, a locking frame is used to compress the concrete and transition inserts into place.
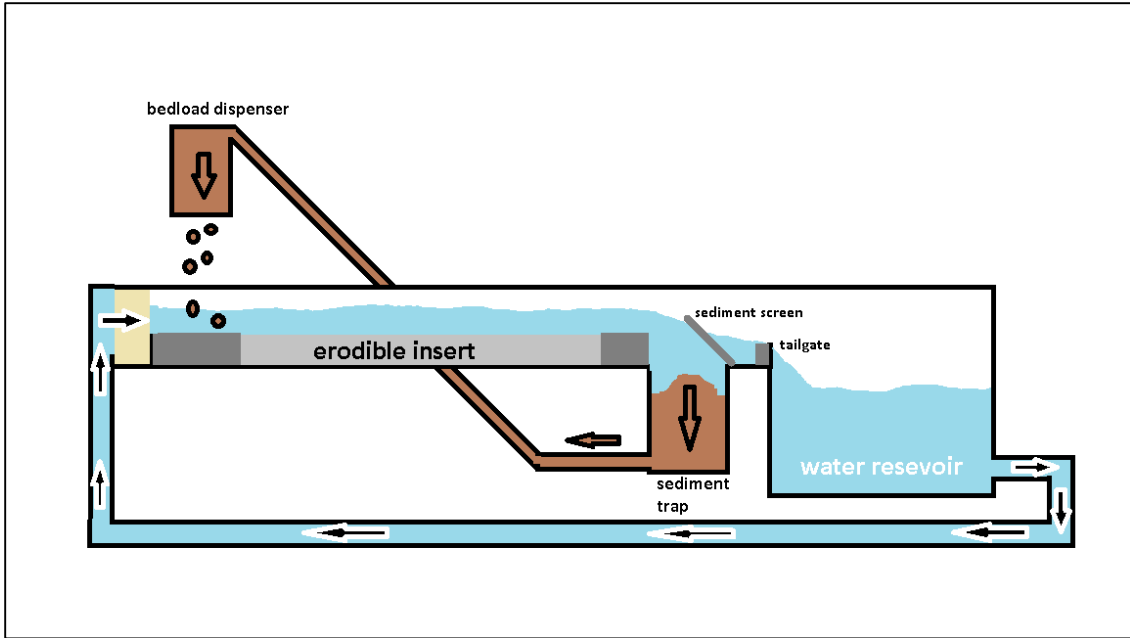
Figure 4: Simplified diagram of flume. Minus the bedload dispenser, all items listed here may be tilted between 0-10% slopes.

Figure 5: Upstream section of flume, including honeycomb flow gate (far background), followed by the transition insert, and nearest the concrete insert (semi-smooth roughness seen here). Above the flume at the most upstream section is the suspended sediment fan.

Further downstream of the inserts within the flume, a sediment trap is outfitted with various screens and meshes to catch transported particles and allow them to settle in a sediment trap that extends beneath the flume (Figure 4). Depending on the particles used, this tank can either recirculate the sediment simultaneously with the flow (1-inch diameter return line for sand) or after each experiment run (3-inch diameter return line for granules). Special precautions must be taken when recirculating either of the sediment types to prevent very difficult clogs and other mishaps, and the flume instruction manual must be read fully before any attempt at replication of these experiments.

Sand/suspended sediment is used in the 1-inch line while the larger bedload particles can only be moved through the 3-inch line. The sand is recirculated simultaneous with water flow throughout the duration of an experiment, and enters the flume through the fan-shaped outlet of the 1-inch return line. The motor speed to the 1-inch line and the shape of the fanned outlet are calibrated experimentally to ensure consistency in sediment flux and laterally-uniform sediment distribution, respectively. The larger particles (pea gravel) are returned to the sediment hopper that is fixed above the transition insert of the flume. The sediment flux here is calibrated to a number corresponding to the speed at which an internal auger spins and thus pushes out the gravel. Note that these calibrations are made for approximately 5 minutes after recirculating the sediment to the hopper, when water is barely dripping from the outlet, and additionally, note that gravel larger than 5.88 mm is not recommended in an identical setup as the hopper may not function reliably.

Bedload particles used in the experiment (D_{50} = 3.39 mm, 4.63 mm, 5.88 mm) are dropped into the flume from a hopper located upstream and above the erodible insert. This hopper is capable of dispensing sediment at a maximum rate of 225 grams per second. As the gravel falls, it is dispersed by a metal cone in order to spread the sediment load ~uniformly across the width of the flume. Near the end of the flume, before the reservoir basin, this bedload falls into a sediment trap. From the sediment trap here the gravels can be recirculated to the hopper using an electric motor and 3" PVC tubing independent of the water supply (Figure 4). The smaller sand particles that near suspension (using our flow conditions) are stored in this sediment trap between bedload runs. These sands (D_{50} = 0.56 mm) are recirculated to the upstream end of the flume via separate 1" PVC tubing, but use

13

the same pump as the larger 3" PVC tubing. A diverter valve directs which tubing is used.

At the very end of the flume is the reservoir water basin, this acts as a reservoir for water but also as a last precaution against loss of transported particles. A total of 5 aluminum mesh screens are installed in the flume, at an angle inclined upstream, directly above the sediment trap. This helps to slow down and create enough turbulence to force grains as small as $D_{50} = 0.56$ mm to drop, and prevent recirculation via the main water reservoir beyond. Periodically this basin will be drained and cleaned so that the settled fines (mostly from the eroded bed) can be removed.

Figure 6: Large basin/water reservoir at the downstream terminus of the flume. Here the basin was drained to allow cleaning of the relatively small amounts of sand and silt deposited after many erosion experiments.

The flume itself is designed so that water discharge (Q_w), slope (S), and sediment flux (Q_s) can all be controlled independently. Variable-speed electric motors propel water from the reservoir basin through PVC tubing to the upstream end, at maximum flow rates exceeding 75 L/s, and measured in-line with installed magnetic flow tubes. Similarly, a separate motor moves material from the sediment trap through either the 1-inch or 3-inch lines, depending on the current sediment being used. The basin, flume channel, motors, and all 3 recirculation tubes (small sediment, large sediment, and water) are mounted to the floor on a hinge; this allows a pair of screw-drives under the upstream section to tilt the flume for slope control between 0%-10%. A control panel near the observation platform displays the current slope value, pump motor speeds, and measured rates of discharge, as well as the interface to change these settings. The recirculating design is ideal, not only for independent control of key variables, but also for extended-duration experiments.

Figure 7: Screw drives that control bed slope of the entire flume (opposite end is hinged). In the background are future inserts containing concrete in the process of curing.

Figure 8: Flume control area. Reservoir basin is blue object on bottom-right, scanning laser is attached to cart sitting atop the rails halfway upstream flume, control panel is blue object just below the cart.

Figure 9: Sediment disperser placed below sediment hopper used to evenly distribute sediment grains along width of the flume insert.

The concrete used in the flume insert is formulated to be very weak, but to abrade by the same processes as real bedrock (i.e. brittle fracture under tension). Initially, the inserts were created up to 3 at a time in a large concrete mixer to help ensure similar properties between separate inserts, but it was later discovered that single batches following a strict protocol made for more consistent tensile strength and texture. Technically a mortar, this erodible material consists of sand with a D_{50} of 110 microns (Silcosil F110) and Portland cement type 3, following *Sklar and Dietrich* [2001] and *Johnson and Whipple,* [2010]. This artificial bedrock was made on-site in a mortar mixer large enough to theoretically fill 3 inserts with dimensions of 3 meters by 30 centimeters, to a depth of 15 centimeters in a single batch, in the expectation that one large batch would create a more consistent material than 3 separate mixes of the same recipe. With successive batches, however, the consistency of concrete poured from the top of the mixer compared to that at the bottom varied much more than the difference between single-insert batches created at separate times, so single batches were preferred.

Of the 10 inserts created, half consisted of a 15:1 sand-to-cement ratio (by weight), the others 25:1. Generally speaking, concrete becomes weaker as this ratio increases, or as the aggregate size decreases [Sklar and Dietrich, 2001]. During the mixing of each concrete batch, samples were collected in 2" x 4" cylinders (although only half filled half). The tensile strength was then measured at discrete time steps (between ~15 - 700 days) to create a curing curve. As an average among the many concrete batches, the tensile strength at the time of experimental runs of the stronger 15:1 mix was measured at approximately 0.14 MPa, and the weaker 25:1 mix at 0.05 MPa, most comparable to the weakest sandstones tested by Sklar and Dietrich (2001).

The curing of concrete is a slow chemical process, shown below, and consumes water, thus it is important to keep the insert (and samples) hydrated.

$$Ca_3SiO_5 + H_2O \rightarrow (CaO) \cdot (SiO_2) \cdot (H_2O)_{(gel)} + Ca(OH)_2 \qquad (\ 10 \ )$$
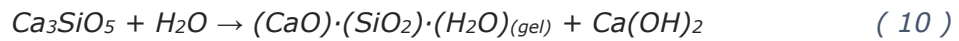
Note that this reaction remains unbalanced for clarity. Since water content at the time of mixing can also control the characteristics of the concrete, this factor was also controlled as much as possible (only enough water to keep the mixer moving). As the above reaction progresses, the concrete becomes stronger, but ~90% of the material's potential strength will be reached within the first four weeks. Most practical applications of concrete require testing of compressive strength, but as seen in Equation (3) bedrock abrasion scales with the tensile strength of the artificial bedrock. The samples were tested using the Brazilian test, where the cylindrical sample is given an axial load at a constant rate until the material reaches a deformational failure (Figure 6). The value of tensile strength at this point is calculated with the following:

$$\sigma_T = \ 0.636 \frac{P}{Dt} \qquad (\ 11 \ )$$

The above calculation can be used to estimate the tensile strength of each insert at the time of each erosion experiment. The average cylinder thickness (L) is approximately 2.2 +/- 0.18 inches, and the cylindrical casing for the samples has a manufactured diameter (D) of 2 inches. The applied load (P) is taken from testing the maximum load on the cylinder before structural failure of the sample.

3.2: Experiment Design

With the ability to control discharge, slope, and sediment flux independently, the flume is capable of creating scenarios not found in nature (e.g. low slope and water discharge with no alluvial cover, high slope and discharge but very low sediment flux). To make comparisons easier, a small set of each variable was chosen; slope conditions would be selected as either 2%, 5%, 7%, or 10%;

discharge as either 18 L/s, 35 L/s, or 55 L/s; and sediment flux either 50 g/s, 100 g/s, or 215 g/s, although 100 g/s was the norm for the vast majority of all experiments. When testing a given variable (typically slope or discharge), all other controls were held constant unless otherwise noted.

The experiment is designed so that each insert can be subjected to many different sets of flow conditions. Experimental runs are typically 15 or 30 minutes in duration. Runs identical in nature are repeated at the start and finish of each experimental series to test for reproducibility and to account for any differences associated with the evolving bed topography (see Johnson and Whipple, 2010 for a detailed discussion) since erosion rates may be affected by many subtle factors, including bed topography, curing time, and even the grain size of the preceding experiment. For this reason, the insert topography was manually smoothened between runs when grain size was changed, or to prevent the imminent incision of a deep channel. An effort was made to randomize pre-existing bed topography, experimental run order, and other potential factors in erosion rate to guard against the possibility that these changing conditions could complicate interpretation of the relationship between flow conditions and erosion rate. I also periodically ran repeats of experimental conditions already recorded, not only as a test of reproducibility, but also to ensure that much data was gathered for each state of bed roughness.

Flow discharges of 18, 35, and 55 L/s were considered. Depending on slope, these discharge values resulted in flow velocities exceeding 2.5 m/s. Additionally, flow conditions were carefully varied among the large range of possible values (Q_w = 18, 35, 55 L/s, S = 2%, 5%, 10%) to lessen the chance that an evolving bed topography would affect any relationships uncovered (i.e. simply increasing values of discharge and/or slope with each successive experiment).

Different methods of measuring bed shear stress were used and compared to most accurately reflect the near bed shear stress and flow velocity driving sediment transport and thus rock abrasion. Vectrino ADV point measurements were used to estimate Reynold's stress along the flume length and width, and also in the axis of deeply incised channels. Also using the ADV probe, velocity profiles are used to derive shear velocity (and therefore shear stress) from the Law of the Wall. Shear stresses were also calculated from measurements of flow depth and slope. This simple relationship of the depth-slope product (τ_b = pghS) requires an absence of acceleration within the flow, and I follow *Chatanantavet et al. (in preparation*) to account for the non-ideal conditions, where the depth-slope product is generally reduced as a function of changes in flow depth downstream if flow acceleration is observed. These results are then checked against the ADV point measurements to confirm accuracy.

An exposed bedrock stream is simulated with weak concrete, as similar artificial rock has been used with success in several experimental studies [Sklar and Dietrich, 2001; Chatanantavet, 2007; Johnson and Whipple, 2007; Finnegan et al., 2007; Johnson and Whipple, 2010]. The weak concrete was created in mixes of 15:1 and 25:1 of sand-to-cement ratios (by weight), as well as assorted samples between these ratios to create a trend. It is thought that abrasion rates scale inversely with the square of tensile strength [Sklar and Dietrich, 2001]. As our study considered erosion on materials of only two distinct strengths we cannot quantitatively test this prediction. However, the weakest of these mixes (25:1) was used to assist the study of erosion by suspended particles when it was shown that even extended durations of these erosion experiments showed little measurable erosion on the hardest concrete variety (15:1), roughly consistent with the order of magnitude difference in erodibility predicted given the factor of 3 difference in tensile strength.

This study examines the relationship between mean grain size and erosion rates on an exposed bedrock surface, but also takes into account key variables such as bed slope, water discharge, sediment flux, and bed roughness (morphology). For the range of flow conditions and grain sizes used, it was found that these particles are transported downstream primarily by saltation. With discrete controls over the many factors of erosion in the saltation-abrasion model, our experiments were specifically designed to test the predictions of *Sklar and Dietrich* [2004].

Quartz grains were used as abrasive particles in transport to erode the concrete substrate and varied an order of magnitude in median grain size diameter (D_{50}). These sizes included a sand (0.56 mm), and three gravels (3.39, 4.63, and 5.88 mm) [Figure 7]. The settling velocities of these grains were calculated as 15.7, 47.5, 56.4, and 68.0 cm/s, respectively [Dietrich 1983]. The grains are rounded-to-subrounded, and showed medium-to-high sphericity. Experiments were planned to explore the role of each variable (D_{50}, Q_w, Q_s, and S) against each type of bed roughness. Experiments nearing suspension of grains were typically dispersed between runs involving the gravels, as the former had a very weak capacity to sculpt the bed and influence larger scale roughness of the bed: where the larger grains can be seen to erode deep channels and undulating patterns, the sand primarily eroded smaller-scale facets on the floor and walls of those channels.

With few, noted exceptions, all erosion experiments were run for either 15 or 30 minute durations, and during this time, values of slope (S), water discharge (Q_w), sediment flux (Q_s), and mean grain size (D_{50}) were held constant. During each experimental run, the concrete insert experiences some erosional lowering, which is measured before the next erosion run. With separate control of S, Q_w, Q_s, and D_{50}, most sets of experiments were planned such that each key control was varied across the entire range of values possible in the flume, all while keeping the others

22

variables constant. Section 3.4 documents the list of flume settings for each erosion experiment.

3.3: Data Collection Methods

Erosion is measured by creating a high-resolution DEM of the concrete surface in the test section, using a high-speed computer-controlled axis system containing a triangulating laser displacement sensor (Keyence LK-G502). Bed topography is measured with this system before and after each period of erosion (typically time steps of 15 or 30 minutes). Erosion is reported as the average of vertical incision across the bed area (XYZ matrix subtraction of the DEM before/after experimental run), calculated from the laser data imported into Matlab.

The Keyence system was programmed to scan the bed surface at 2 mm spacing in the cross-stream direction (y) and 4 mm in the longitudinal direction (x). The residual amount of sediment and water left in the insert after an experiment was blown downstream with a high-powered hair dryer, this action was required to maintain uniform, dry and clear conditions to achieve accurate scan results. Mean erosional lowering in each experimental run was determined by differencing topographic scans taken before and after each run and taking the mean. To assess confidence bounds on our measurements of mean erosional lowering, in numerous instances we completed a repeat scan of the bed topography immediately before starting the subsequent run. These repeat scans were taken with the same conditions of ambient lighting and bed wetness as all post-experiment scans. Ideally such repeat scans would record zero elevation difference at all pixels. However, the telemetric laser has a measurement uncertainty of +/- 0.01 mm at the mean measurement distance in our setup. In addition, the artificial concrete bed has micro-roughness on the order of 10s of microns and even small positioning errors during the repeat scans could induce large local errors where bed topography is

steep. Distributed throughout the experimental runs reported here we conducted 16 repeat scans. Each repeat scan should find a 0.0 mm elevation difference. Actual values range from -0.044 mm to +0.035 mm, with a single outlier at -0.072 mm. The mean of all 16 repeat scans (including the single outlier) is -0.009 with a standard deviation of 0.028 (excluding the outlier the mean is -0.005 with a standard deviation of 0.023). We use the standard deviation about the mean of all 16 repeat scans to quantify the uncertainty on our measurements of mean erosional lowering and round up to two significant figures for a one-sigma uncertainty of 0.03 mm. This uncertainty is included as error bars in all figures.

Bed roughness conditions were initially only a qualitative, visual assessment. Smooth beds were determined when the concrete insert was flat and before any rills or early channel morphologies were observed. A very rough bed surface was documented when the insert had developed a deep incised channel, often with steep channel walls and a slight meandering path. Semi-smooth, semi-rough, and rough bed morphologies are labels as the bed surface evolves between those two extremes. Only during analysis of the importance of roughness to erosion rates were the experiments quantifiably measured; the roughness conditions were categorized by the average of standard deviation in elevation of the bed surface.

To preserve the bed for a larger number of experiments, when the bed surface reached a rough or very rough morphology it would be manually "shaved" down to at least a semi-smooth roughness. The reasoning here is that a high roughness would direct all erosion to a relatively narrow strip of the insert, and erosion experiments must cease when the concrete is eroded down the Plexiglas bottom, in any area that is scanned. The only other occasion that the insert would be manually altered is after repeated erosion runs using the smallest grain size (which hovers near the transition between saltating and suspended grain transport modes). After repeated runs, these

grains create sharp, brittle erosional facets that may artificially enhance the erosion rate in whatever later experiment causes them to break off. Similarly, suspended load erosion may exhume hardened cement nodules (these occurred only in some inserts and did not affect either measured tensile strength nor erosion rates in experiments with larger grains), which were therefore routinely filed down.

In an attempt to maintain consistent material properties, multiple earlier inserts were poured from a single batch in a large concrete mixer. Later, it was determined that smaller mixtures made for each insert were actually more consistent visually (some stratification within the mixer). This tensile strength was measured for each insert with data presented here, as the resistance to abrasion by saltating particles has been shown to scale with this property of bedrock [Sklar and Dietrich, 2001; Beyeler 2010]. The Brazil Test is an indirect measure of tensile strength [Fig. 10], performed by applying a steadily increasing force perpendicular to the circular cross-section of a cylindrical test specimen [Brown 1981]. The applied force at the moment of failure is recorded for calculation of tensile strength [Fig. 11]. Dozens of test samples were made for each insert, and testing occurred approximately 5 times for each between curing times of 30 to 500 days. No test samples were made for Insert 8 (of 10 inserts), so unfortunately no data from those experiments were used for analysis.

Figure 10: Equipment used for Brazil test method of measuring tensile strength of concrete test samples.
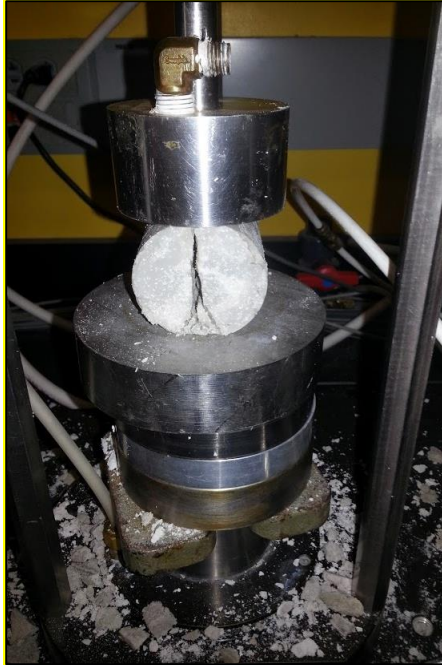
Figure 11: Brazil test of concrete sample at point of deformational failure

Flow conditions were documented from set values of discharge and slope, and most experiment runs also include a scan of the water surface for purposes of measuring flow depth. An ADV probe (acoustic Doppler velocimeter) is used in specific points along the concrete bed to support calculations of Rouse and Froude numbers relevant for understanding the transport processes of particles in the flow and for determining local bed shear stress.

Bed slope was determined from an integrated control on the flume control panel, but verified with a magnetic protractor attached the undercarriage. Flow velocity was measured using in-line magnetic flow tubes, as part of the flume itself, and flow velocities were verified with a Vectrino acoustic-doppler velocimeter (ADV) probe. The ADV probe was also essential in measuring shear stresses independent from the general depth-slope product method.

Reynold's stress at the bed surface was determined by the average of the instantaneous fluctuation products of the downstream and vertical flow vectors, as seen below in Equation 12:

$$\tau_{ij}' \equiv \rho \, \overline{u_i' u_j'} \qquad (12)$$

The ADV probe collects approximately 11,000 data points of flow velocity along the downstream, lateral, and vertical vectors within a 1-minute collection period at each depth. Another mode of extracting shear stress from the ADV data was to create a velocity profile of downstream velocity vs. the natural log of the measured height above the bed (the slope of which can be seen as $\frac{u^*}{k}$), and from here shear velocity can be reasonably determined (from an estimation of z_0) and converted into basal shear stress (Equations 13-17).

$$u = \frac{u^*}{k} * ln\left(\frac{z}{z_0}\right) \qquad (13)$$

$$u = \frac{u^*}{k} * ln(z) - \frac{u^*}{k} * ln(z_0) \qquad (14)$$

$$\frac{u}{ln(z)} = \frac{u^*}{k} - \frac{ln(z_0)}{ln(z)} \qquad (15)$$

$$u^* = k\frac{u}{ln(z)} - \frac{ln(z_0)}{ln(z)} \qquad (16)$$

$$u_* = \sqrt{\frac{\tau_b}{\rho}} \qquad (17)$$

Other methods of calculating shear stress at the bed included the depth-slope product (Equation 18) as well as a modified version used to correct for flow acceleration with a 1-D depth-average flow equation (Equation 19). Both variations relied on depth values measured from water surface scans, and the modified version further calculated mean velocity values from those depths along the length of the flume.

$$\tau_b = \rho g h S \tag{18}$$

$$\tau_b = \rho g h S - \rho g h \frac{\partial H}{\partial x} - \rho u h \frac{\partial U}{\partial x} \tag{19}$$

A "honeycomb" at the upstream end and a flow control tailgate at the downstream end were designed and used in the flume as methods to decrease flow acceleration and macro turbulence. Between the honeycomb and the most upstream end of the concrete insert, a non-erodible insert matching the concrete in width and height is used as a transition zone to allow flow conditions to stabilize. Periodically a Vectrino ADV was used to spot-check vertical flow velocity profiles at typical, as well as unique, features on the bed. These measurements were used to determine shear velocity, u*. In addition, Reynolds stress near the bed could be determined for an independent measure of bed shear stress. Note that it would not be possible to measure near-bed flow velocities using the Vectrino during an erosion run, so all data from the instrument is collected without any sediment flux.

For data collection of conditions during experiments, custom equipment was created to hold the various measurement tools used in or near the flume. This includes a harness for the Vectrino acoustic Doppler velocimeter (ADV); a miniaturized bedload sampler in the style of the Haley-Smith sampler (1/2 inch square opening), used for measuring concentration profiles of transported sand particles (D_{50} = 0.56 mm); and a simple metal cone used to disperse gravels falling into the flume from a sediment hopper.

Figure 12: Vectrino probe in place above the bed surface. Distance to the bed is manually measured from the concrete surface to the central head of the probe. Holding the Vectrino is a precise screw-drive mount, and that is attached to the scanning laser cart.

Figure 13: Vectrino probe and pre-determined points of interest to measure flow data. In this case, the flow was to be measured and compared across the width of the flume.

Sediment flux rates (Q_s) were measured by collecting in a bucket grains released from the sediment hopper. Multiple samples were collected, varying duration as well as speed control on the sediment hopper. Each test bucket was allowed to dry completely in the sun before the mass measured on a scale tared for each identical bucket. The plots of sediment mass divided by duration of collection period (sediment flux) with sediment feeder number (indicating speed of screw drive) were used to find the setting required for each of the pre-determined modes of Q_s = 50, 100, and 215 grams per second for each bedload grain used (D_{50} = 3.39, 4.63, and 5.88 mm). For most consistent results, each sample collection from the sediment hopper was timed a few minutes after running the 3-inch sediment return

line, just long enough for water escaping from the sediment hopper to slow to a drip. The smallest grain size (D_{50} = 0.56 mm) was recirculated in a separate 1-inch sediment return line that did not feed into the sediment hopper, and instead directly into the most upstream section of the flume, so for this case the calibration of sediment flux used the variable frequency of the motor powering the sediment return lines (in hertz). Otherwise, these samples were similarly collected in buckets, dried, and put on a scale.

Median grain diameter (D_{50}) was measured for each grain size using a set of standard stacking sieves. The grains were poured from their bags (sieve labels from bag: 1/4" x 1/8", 3/8" x 3/16", 3/16" x #10, and #30) into a bucket and scooped out for each use of the sieve (to filter out erroneous small fragments of grains non-representative of the sediment label).

CHAPTER 4: RESULTS

4.1: Concrete Tensile Strength and Other Material Properties

Tensile strength of the stronger concrete insert averaged 0.14 MPa during the time of experiment (between 100 and 500 days curing), and 0.05 MPa for the weaker concrete. These values can be plotted against the amount erosion vs. tensile strength in *Sklar* [2001], and plot within the regression curve nearest the closest equivalent of their weakest sandstone. For example, one can expect a median erosion rate somewhere near 0.002 meter per hour on the strong concrete (and twice that on the weak), and multiplied by the 2000 meter x 0.3 meter test section, as well as an estimate for the concrete density, yields an erosion rate around 1000 grams per hour.

It should be noted that the tensile strength for Insert 4 was slightly higher than the results for Insert 1-3 and Insert 5, but the reason is unknown. The weaker concrete (25:1 sand: cement ratio) was created as a response to negligible erosion on the stronger concrete (15:1) during the sand (D_{50} = 0.56 mm) experiments, in which the flow conditions on this smallest grain size hover near the transition from saltation to suspension (suspended particles impact the streambed far less by definition). Although tensile strength was extensively measured for all concrete batches (except Insert 8, so it was excluded from analysis), the parameters of Young's modulus of elasticity (Y) and the dimensionless abrasion constant k_v from Equation 5 were not tested independently in this study.
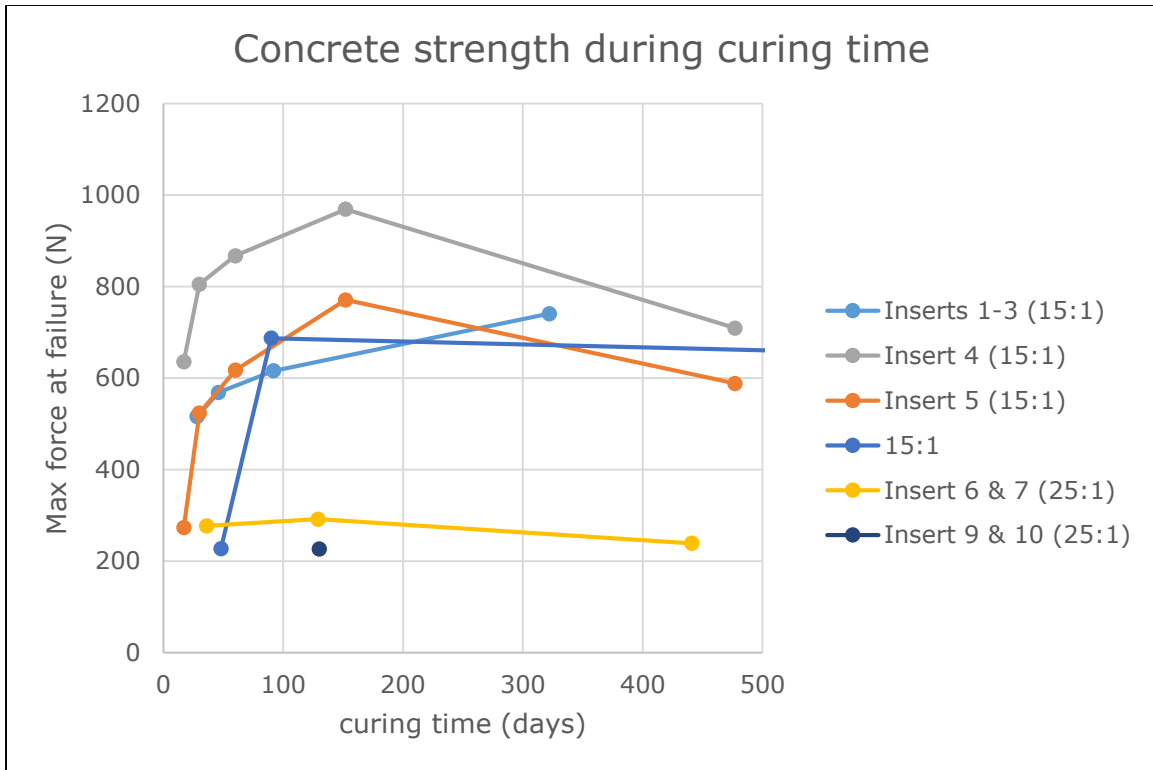
Figure 14: curing curves of concrete mixtures of varying sand: cement ratios

4.2: Erosion vs. Sediment Flux (Qs) and Bed Exposure

Before results of E vs. Q_s are shown, it's important to understand why their relationship is so vital to the paper. If it can be established that no alluvial cover effects persist on the bed ($F_e = 1$), then a potentially complicated factor in the saltation-abrasion model can be ignored. With the dependence on Fe eliminated, erosion rates can be predicted relative to "excess" shear stress $\left(\frac{\tau^*}{\tau_c^*} - 1\right)$ and D_{50}. More specifically, the saltation-abrasion model of *Sklar and Dietrich* [2004] predicts that (all else held equal) increases in shear stress will lower erosion rates (as τ^* is raised to a negative power) and increases in D_{50} will increase raise erosion rates (as $\frac{1}{\tau_c^*}$ is raised to a negative power), as seen here again in Equation 9 (where $F_e = 1$).

$$E = K\, q_s \left(\frac{\tau^*}{\tau_c^*} - 1\right)^{-0.5} \qquad (\,9\,)$$

34

In order to understand how this is possible, we look at a previous study from *Chatanantavet [2010]* that examined the relationship between F_e and the supply to capacity ratio $(\frac{q_s}{q_t})$ of a flume system (Fig. 15).
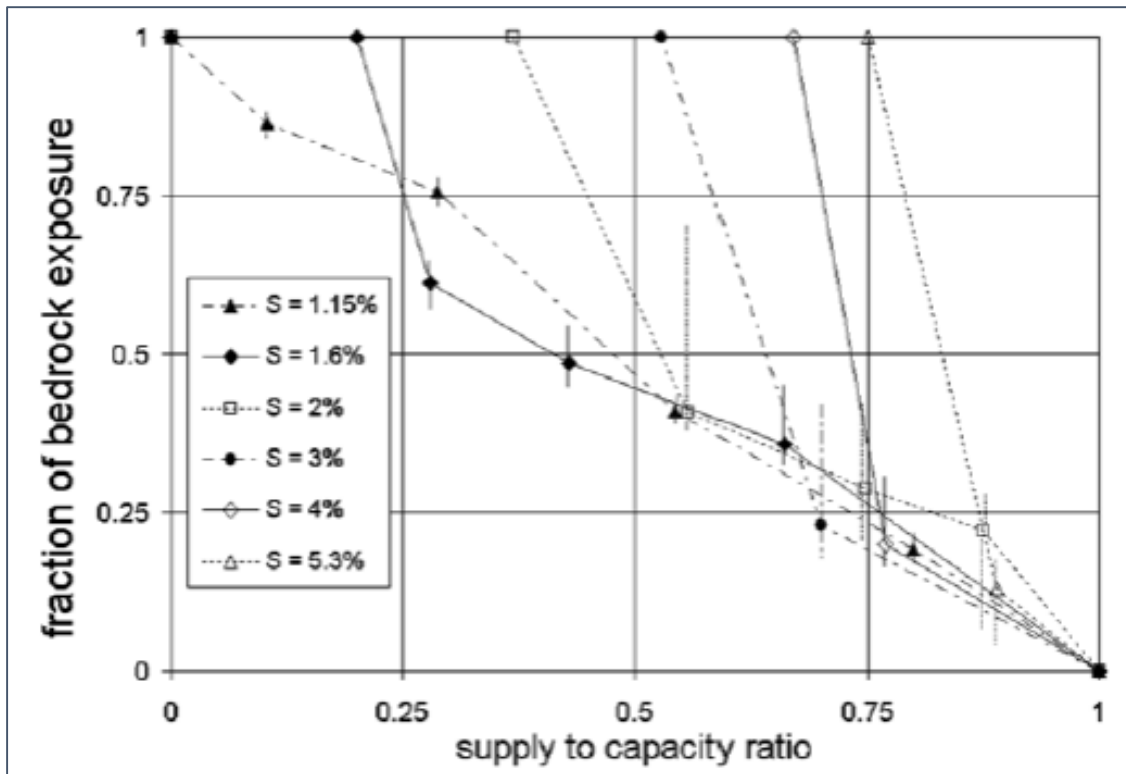
Figure 15: F_e vs. q_s/q_t, showing that for certain conditions, the supply to capacity to ratio can increase while the bedrock remains completely exposed. Reproduced from Chatanantavet [2010].

We call attention to the top edge of x-axis in Figure 15. Along this line there are several data series for which the bed remains clear of sediment (F_e = 1) over a significant range of the supply to capacity ratio (up to 0.75 for the steepest slope). Eventually a critical value of this ratio is reached where alluviation suddenly occurs; once this threshold is crossed, F_e varies as predicted by *Sklar and Dietrich* [2004] - see Equation 9. This indicates that in bedrock channels, F_e does not gradually decrease as $\frac{q_s}{q_t}$ grows, but rather that there is a threshold value to initiate alluviation that depends on flow conditions and likely the roughness of the bed surface.

Fortunately enough, our erodible concrete inserts are very smooth (relative to natural settings), and so finding flow configurations where $F_e = 1$ is not problematic.

Figure 16 plots erosion rates vs. sediment flux (Q_s) for a wide range of flow stages, but focuses on the lower slopes and discharges where alluviation may have been more likely. Alluviation was very rarely observed after an erosion experiment, but the relationship between erosion rate and sediment flux can help identify the threshold for alluviation and effective bed cover in terms of experimental flow conditions.
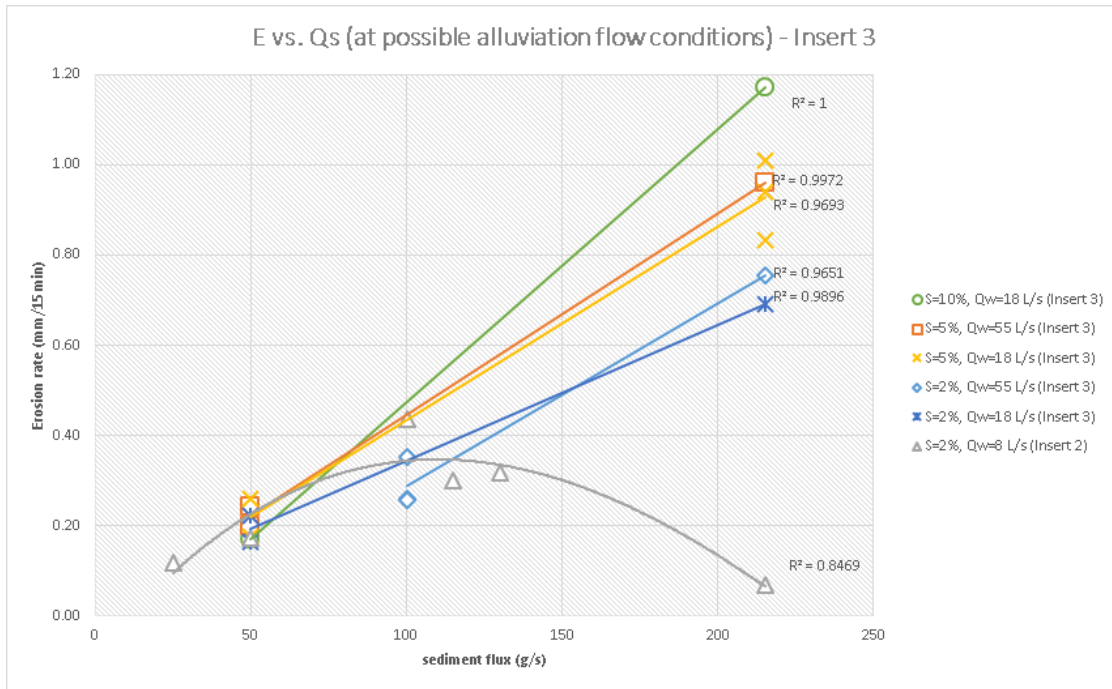
Figure 16: Erosion vs. sediment flux at flow conditions where alluviation may occur. A linear trend with q_s is indicative that the bed is free from persistent alluvial cover.

As seen above, with the exception of a data series where S = 2% and Q_w = 8 L/s, each of the flow configurations displays a strongly linear relationship of erosion rate vs. Q_s. By ignoring the experiments that fail this test, we can safely assume that $F_e \sim$ 1 for all qualified flow conditions (since Eq. 9 shows that $E \sim q_s*F_e$). This allows us to isolate the dependence of erosion rate on flow shear stress.

To ensure this relationship holds true for the other bedload grains used, Figure 17 includes all grain sizes and concrete types at a single flow condition, and still shows a strong linear trend of erosion versus sediment flux. This relationship was observed for all flow conditions where sediment flux was varied, but not enough data was created to include all grain sizes for all flow conditions in such a plot. Again, a condition of all experimental runs in this study was to disallow any conditions that appeared to create standing deposits of sediment. Any sediment flux greater than the capacity of a flow condition to transport those materials creates cover, which increasingly protects the bed from further impacts [Sklar and Dietrich, 2004] [Chatanantavet and Parker 2008; Johnson 2014]. With this accounted for, erosion rates must increase proportional to this increasing sediment flux.
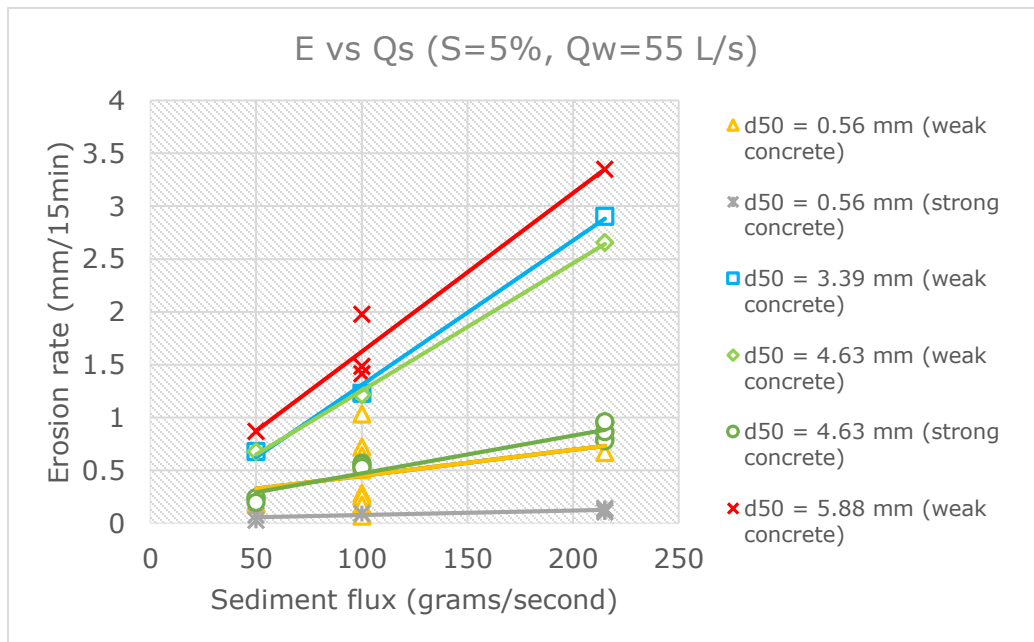
Figure 17: Erosion vs. sediment flux at flow conditions of S=5% and discharge = 55 L/s. Plot shows all grain sizes used as erosion tool across both sets of concrete strengths.

4.3: Erosion vs. Discharge (Q_w) and Bed Slope (S)

Note that for all following results, conditions of Q_s = 100 g/s and D_{50} = 4.63 mm are implied, unless otherwise noted. These conditions are the vast majority of all experiments conducted within the flume. All other factors held equal, erosion rates are invariant with discharge (Fig. 18). Figure 18 is a small series of experiments, but this trend is representative of the whole and replicates earlier results (Johnson and Whipple, 2010), so additional figures are included (all data is provided in tables). To illustrate this point further, a map of measured erosion rates is presented below for a set of experiments at slope = 7%, a subset of data seen in Figure 18 (Fig. 19-21). Note that these figures are not ordered chronologically (even though all three experiments are back-to-back), and instead in an order of increasing discharge. These figures show how erosion looks similar in both intensity and location as Qw is greatly varied.
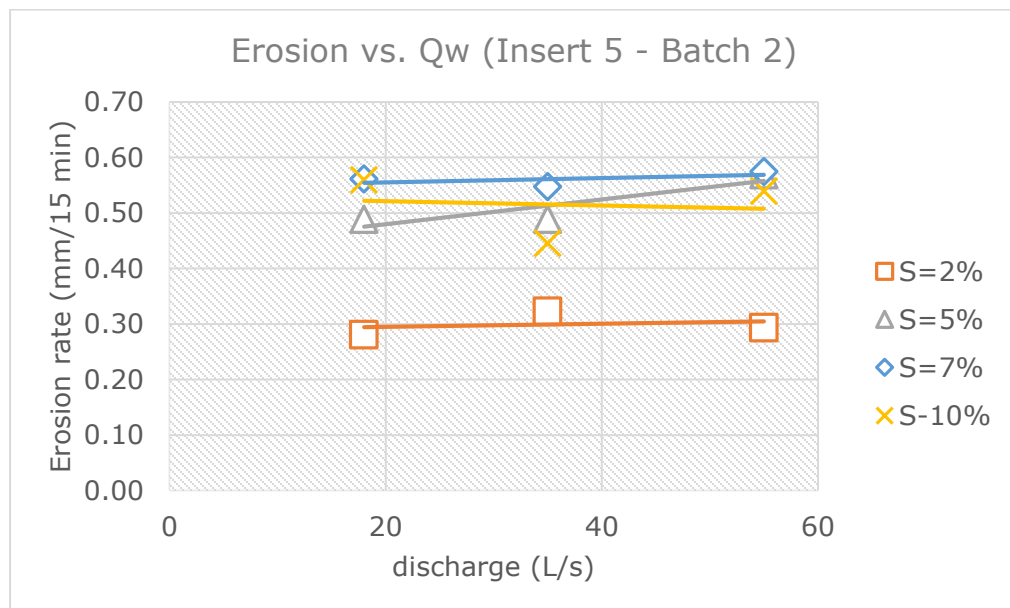
Figure 18: Erosion vs. discharge, showing no trend as discharge increases. Each data series is a different slope.
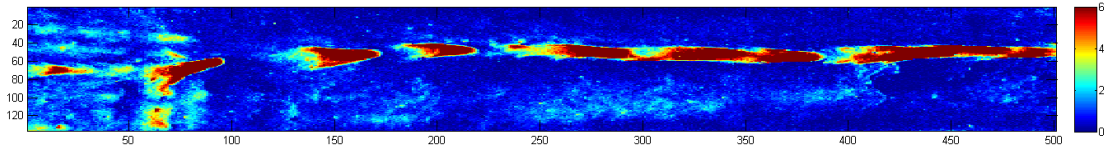
Figure 19: Erosion map of Insert 5, Batch 2, Run 3: S = 7%, Qw = 18 L/s. E = 0.56 mm / 15 min. Color indicates of the amount of erosion (mm).
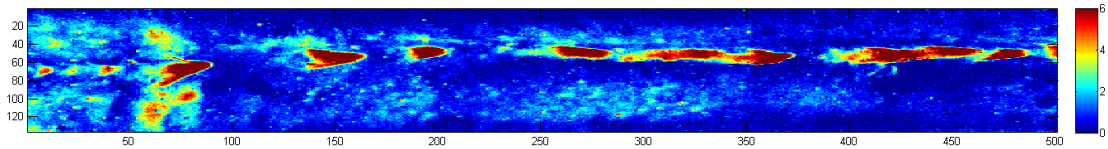
Figure 20: Erosion map of Insert 5, Batch 2, Run 2: S = 7%, Qw = 35 L/s. E = 0.55 mm / 15 min. Color indicates of the amount of erosion (mm).
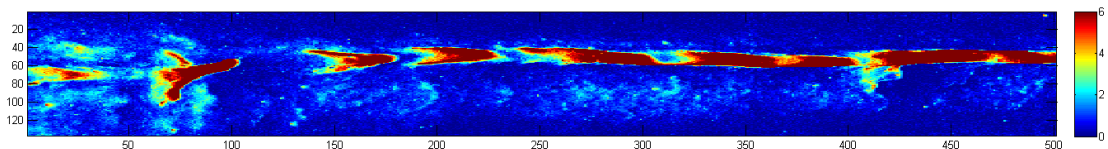
Figure 21: Erosion map of Insert 5, Batch 2, Run 4: S = 7%, Qw = 55 L/s. E = 0.57 mm / 15 min. Color indicates of the amount of erosion (mm).

Unlike discharge, the other independent control of flow stage in the flume, erosion rates reliably increase with increasing bed slope, all else held equal. Figure 22 uses data points from the same set of experiments for the above plots of erosion vs. discharge, but note that each experiment run was not immediately sequential. Again, this is a small set of data, but the trend is representative for all other experiments with varying bed slope. Note that the data points at S=10% were at the end of a large set of experiments, and could be lower due to changes in bed roughness (a topic addressed later in the paper).
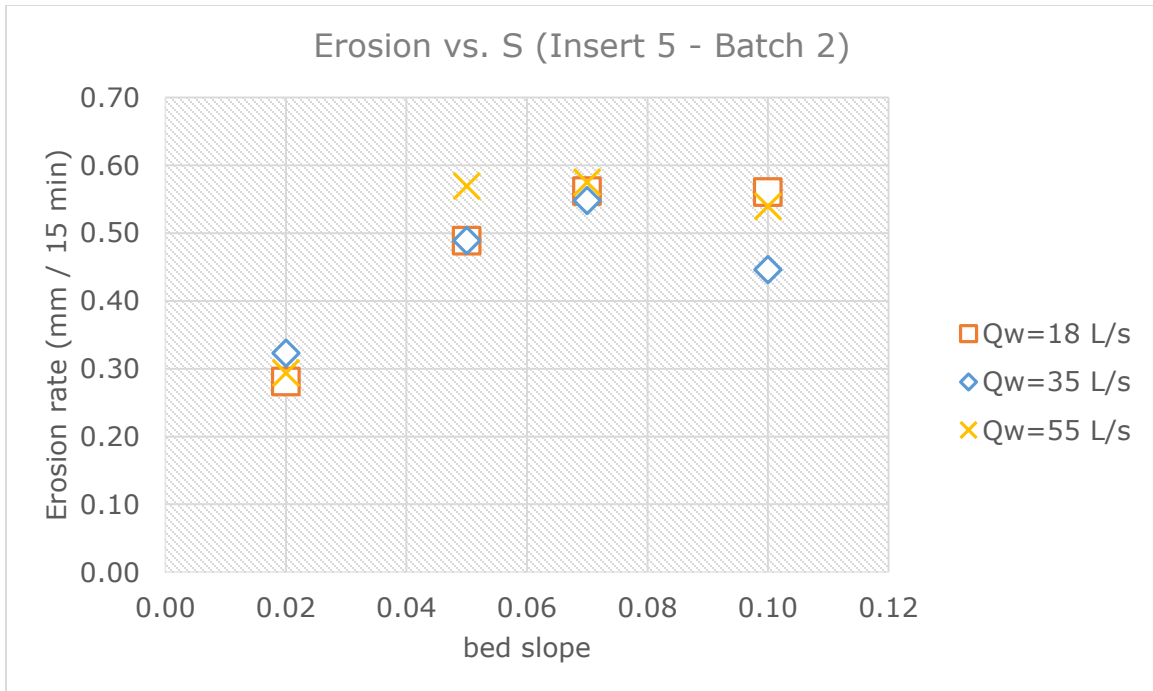
Figure 22: Erosion vs. bed slope, indicating a slight positive trend. Each data series is a different discharge.

Additionally, maps of erosion rate in experiments with varying slope indicate not only an increase in the magnitude of erosion with slope, but also that erosion occurs in an increasingly large area of the erodible insert [Fig. 23-26]. It should be noted that while Figure 23 shows signs of an alluviated bed (erosion halo surrounding an uneroded channel axis), these flow conditions far exceed the minimum shear stress that indicates a lack of persistent alluvial cover, per Chapter 4.2, and is absent at higher slope (Fig. 24-26). Also the erosion rate on the 2% slope was identical for Qw ranging from 18-55 L/s; there is no indication of a change in bed conditions over this range of discharge and the 55 L/s experiments are unequivocally free of any bed-cover influence. Also noteworthy is the relatively low erosion rate at S = 10%; this was the last experiment within a series of 12 experiments, and such, bed roughness was high, and so should further examined further after Chapter 4.6 to follow.
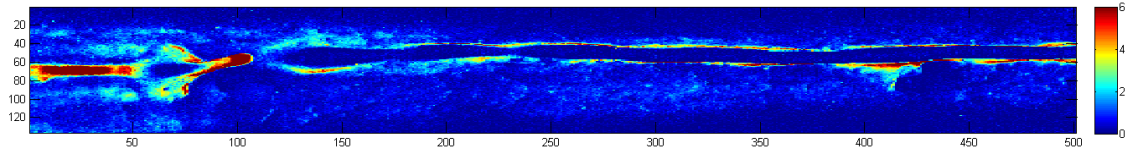
Figure 23: Erosion map of Insert 5, Batch 2, Run 5: S = 2%, Qw = 35 L/s. E = 0.32 mm / 15 min. Color indicates of the amount of erosion (mm).
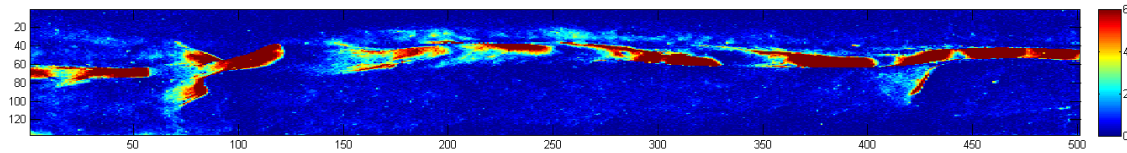
Figure 24: Erosion map of Insert 5, Batch 2, Run 10: S = 5%, Qw = 35 L/s. E = 0.49 mm / 15 min. Color indicates of the amount of erosion (mm).
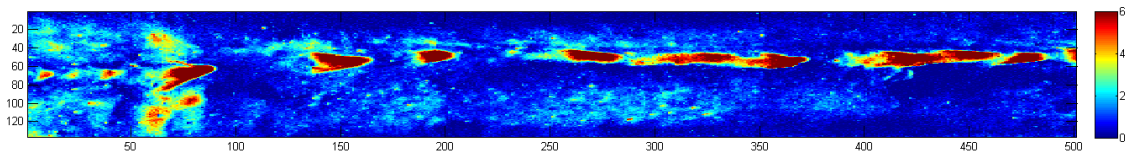
Figure 25: Erosion map of Insert 5, Batch 2, Run 2: S = 7%, Qw = 35 L/s. E = 0.55 mm / 15 min. Color indicates of the amount of erosion (mm).
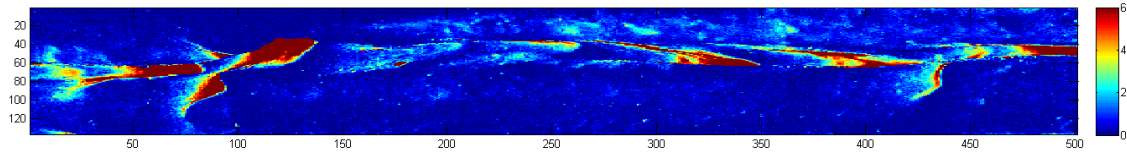
Figure 26: Erosion map of Insert 5, Batch 2, Run 13: S = 10%, Qw = 35 L/s. E = 0.45 mm / 15 min. Color indicates of the amount of erosion (mm).

To understand the phenomenon above more clearly, velocity profiles of the listed flow conditions warranted analysis. A quantification of how fast these bedload particles are impacting the concrete bedrock is the most basic way to understand the power of abrasion across all flow conditions, and the Vectrino ADV probe allows measurement of flow velocities accurate from 5 mm above the bed surface.
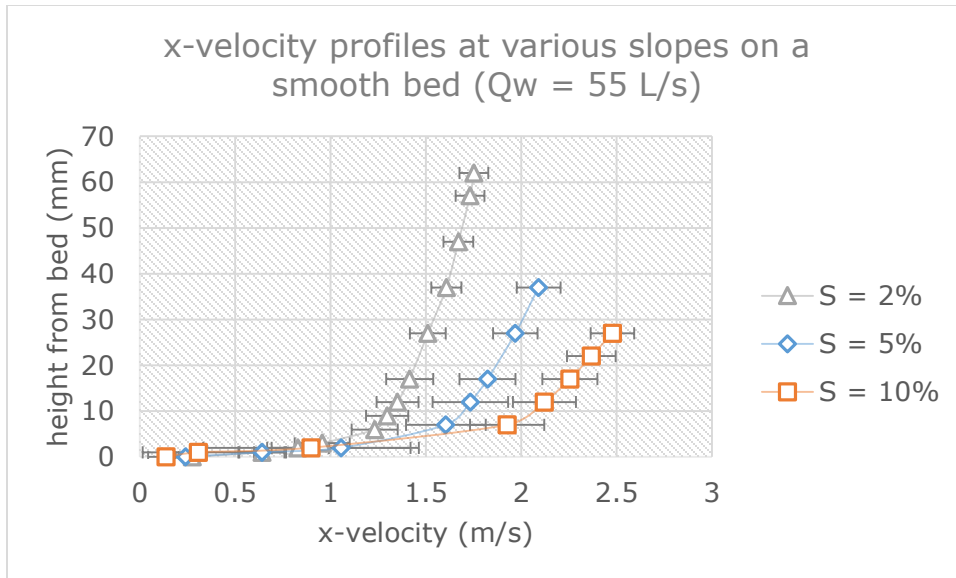
Figure 27: Profiles measuring the x-component of velocity centered within a flume. Data series show profiles of a specific point at different bed slopes. Note drastic change in velocities with respect to slope.
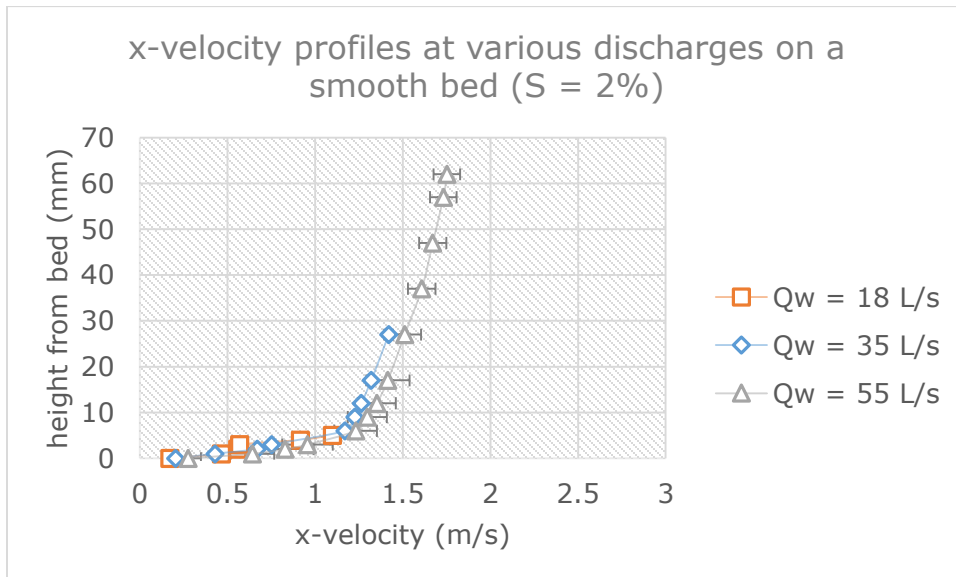
Figure 28: Profiles measuring the x-component of velocity centered within a flume. Data series show profiles of a specific point at different flow discharges. Note relative invariance of flow velocity with flow discharge compared to a changing slope.

Figure 27 shows different velocity profiles at Q_w = 55 L/s, and where each data series represents flow over a different bed slope. On the other hand, Figure 28 shows different velocity profiles at a bed slope = 2%, and each data series represents a different discharge, Q_w. It is immediately obvious that with variations is

42

discharge, flow velocity is really not affected much, and the only real difference appears to be an increase in water depth (the Vectrino probe causes too much turbulence near the water surface to retrieve accurate data in the upper part of the water column). When slope is varied, there is an immediate shift in the near-bed flow velocities as well as the overall velocity profile curvature. By itself, these figures can intuitively describe why erosion rates varied so greatly with respect to slope, yet appeared to be invariant with changes in discharge. To best quantify how erosion scales with changing flow conditions, however, we need to get values of shear stress with which to compare the observed dependence of erosion rate on shear stress to the predictions of the saltation model of *Sklar and Dietrich* [2004]

4.4: Flow Acceleration and Bed Shear Stress

Initial results of erosion versus our independent controls on flow conditions agree with previous, separate studies in that erosion rates are insensitive to discharge (Johnson and Whipple, 2010), but strongly sensitive to changes in slope (Johnson and Whipple, 2007; Chatanantavet, 2007). Since the saltation-abrasion model [Sklar and Dietrich, 2004] predicts that any increase in shear stress will result in decreased erosion rates, either shear stress is not increasing as a function of discharge and slope (as expected for a steady and uniform flow), or basal shear stress is not a sufficient indicator of erosive potential.

Flow acceleration is a potential problem that the flume was designed specifically to prevent, but there is evidence it may still be present (Fig. 29-30). As stated earlier, an accelerating flow creates conditions of reduced bed shear stress. We show below that in our experiments shear stresses were reduced by nearly a factor of two relative to expectations for steady, uniform flow.

Flow acceleration is a possible flaw in the "normal" estimation of shear stress using the depth-slope product, where basal shear stress in a steady, uniform flow is

determined by fluid density (ρ), gravitational acceleration (*g*), water depth (h), and bed slope (S), seen in Equation 18: $\tau_b = \rho g h S$. So from here it must first be confirmed that the flow does not change with respect to time nor position, otherwise this equation cannot be used.

Figure 29 illustrates the water surface profile relative to the bed for all flow conditions used. The left column compares variations in the water surface as discharge changes, each plot holding slope constant. The right column compares variations in the water surface as slope changes, and each plot holding a discharge constant. The bed surface was also scanned (note that it is not perfectly planar). It appears that the flow is least uniform as flow stages of greatest depth, but it should also be obvious that the flow thins and thus accelerates downstream under all flow conditions. For more clarification, the actual flow depths are plotted together in Figure 30. Interestingly enough, however, Figure 31 plots three different velocity profiles at different points along the length of the flume, and lacked any great indication of flow acceleration downstream.
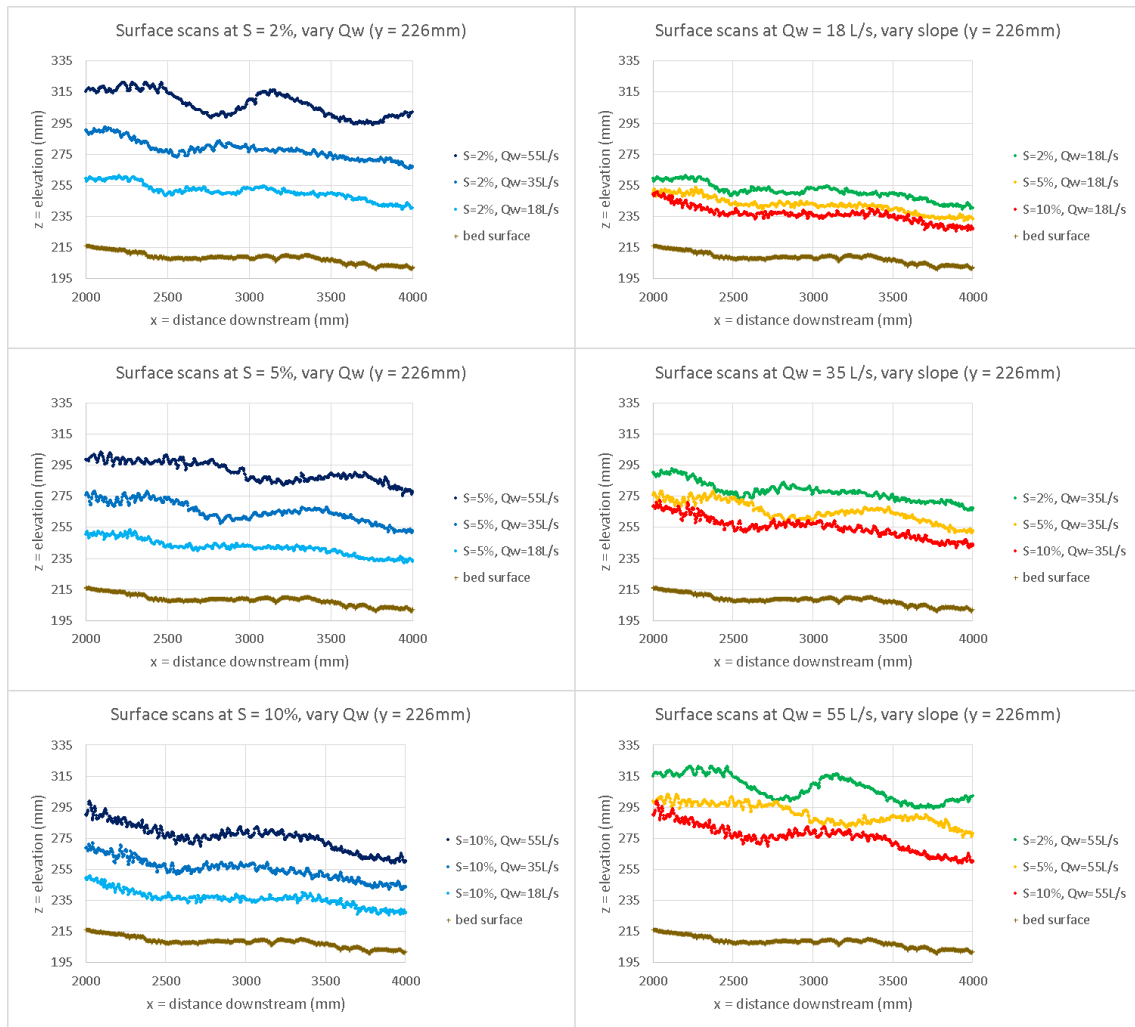
Figure 29: water surfaces relative to the bed. Left column compares the water surface at various Q_w as S is held constant. The right column compares the water surface as S is varied and Qw is held constant.
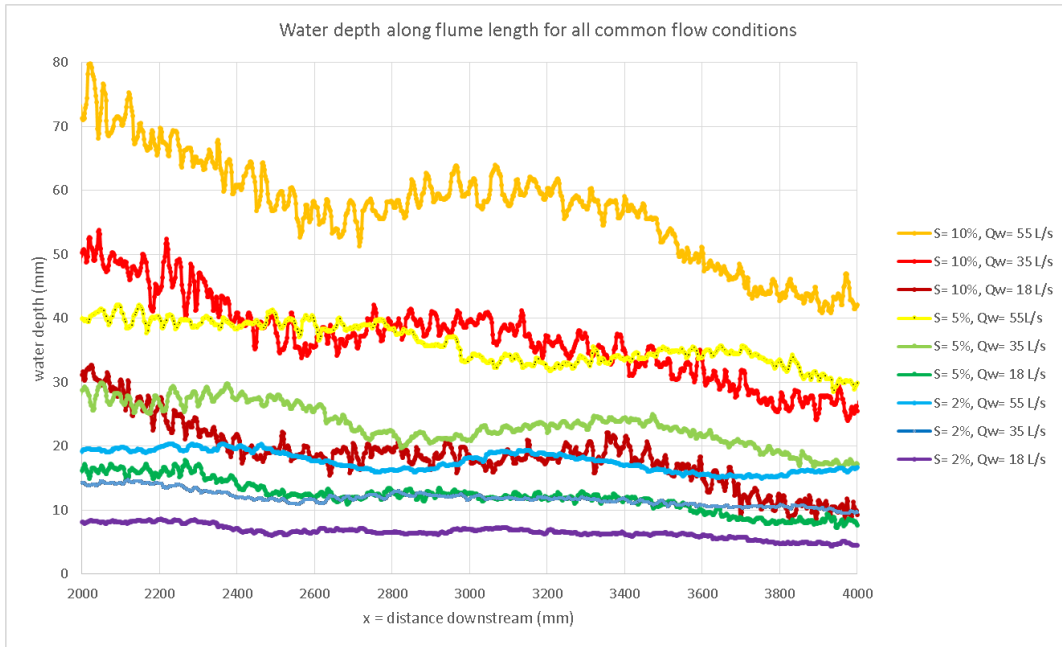
Figure 30: water depths on a smooth bed for all major flow conditions used for erosion experiments.
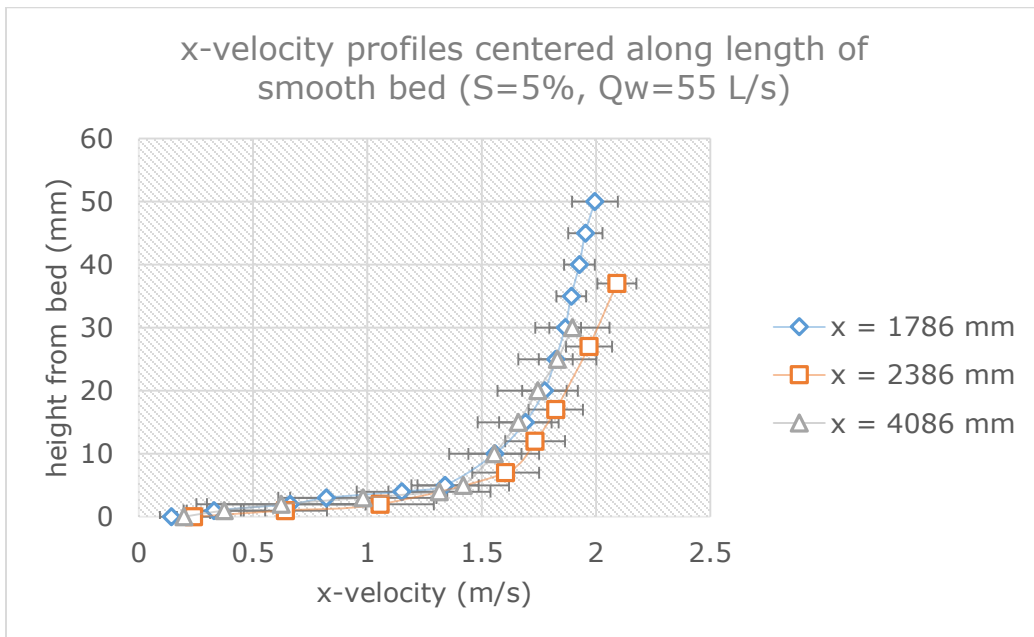
Figure 31: Profiles measuring the x-component of velocity. Data series show profiles along different distances along the downstream length of the flume. Note no significant difference along flume length.

Since flow acceleration must be accounted for in determining bed shear stress, multiple independent methods were used to find a best estimate of shear stress on the bed surface. The first method is a simple correction to the depth-slope product to account for flow acceleration using the backwater equation. The second method calculated basal shear stress by plotting values of Reynold's stress determined from ADV measurements of velocity fluctuations (Equation 9: $\tau_{ij}' \equiv \rho \overline{u_i' u_j'}$) against the height from the bed each sample was taken, then simply fitting a linear regression to the curve at points above 5 mm height (minimum measuring distance for Vectrino ADV probe) to find a projected shear stress at the bed (Figure 32). The third method derived a value for τ_b using the law of the wall (Equations 13-17) from measured vertical velocity profiles using the Vectrino ADV (Figure 33).
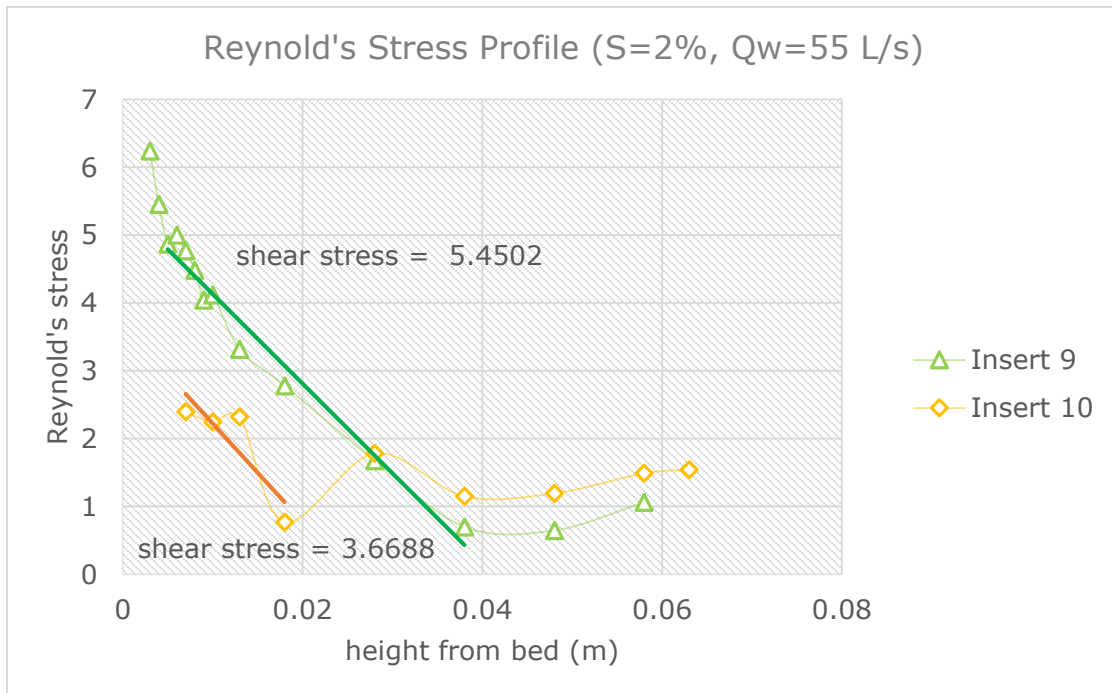
Figure 32: Reynold's stress profiles calculated from ADV data for an example flow condition (S=2%, Qw=55 L/s) on two different inserts of similar roughness. A linear regression is fitted to the near-bed data to estimate the shear stress on the bed surface. Shear stress is calculated from fluctuations in flow velocity as shown here:
$$\tau_b = \tau_{ij}' \equiv \rho \overline{u_i' u_j'}$$
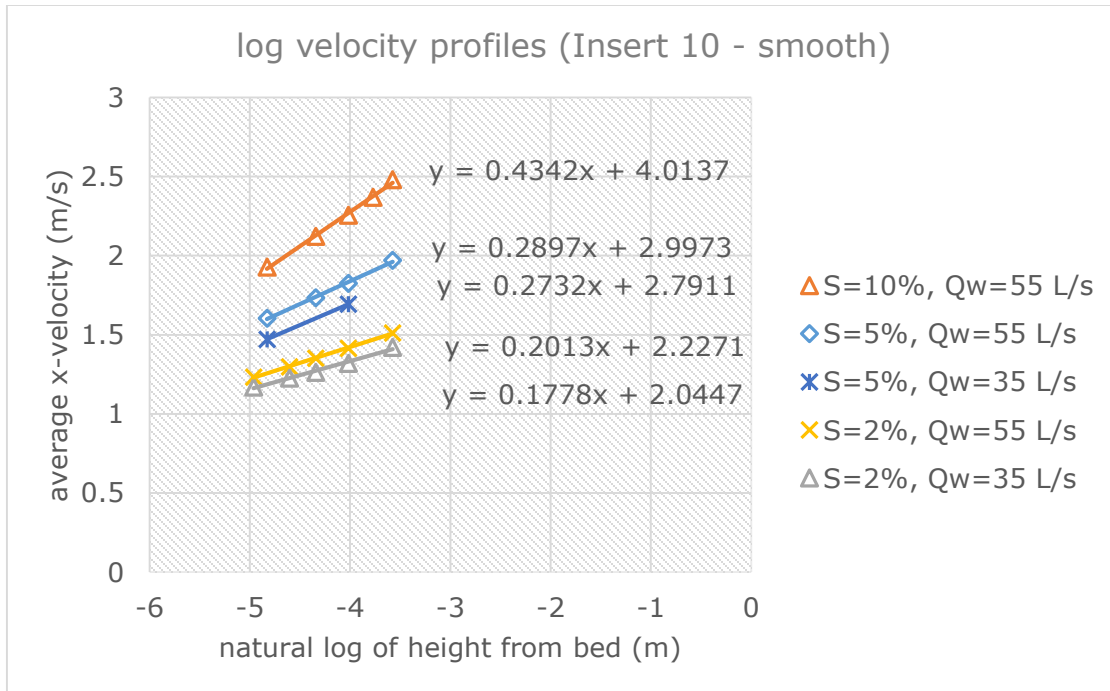
Figure 33: Shear stress calculated from logarithmic curvature of velocity profiles, data from ADV probe. The slope that describes each linear regression ($\frac{u}{ln(z)}$) can be integrated into the Law of the Wall to find shear velocity (u^*), and thus shear stress (τ_b).

Using these methods, plots of shear stress vs. Q_w (Fig. 34-36), and shear stress vs. S (Fig. 37-39) were created that include every major flow condition used in erosion experiments. These data points came from flows on a smooth, uneroded bed and may not be equivalent for every flow condition, but clearly show that the acceleration-corrected depth-slope product (Equation 19) is a decently accurate representation of what shear stress should be for any similar flow conditions (collection of ADV data is very time-consuming and is not available for every experiment).
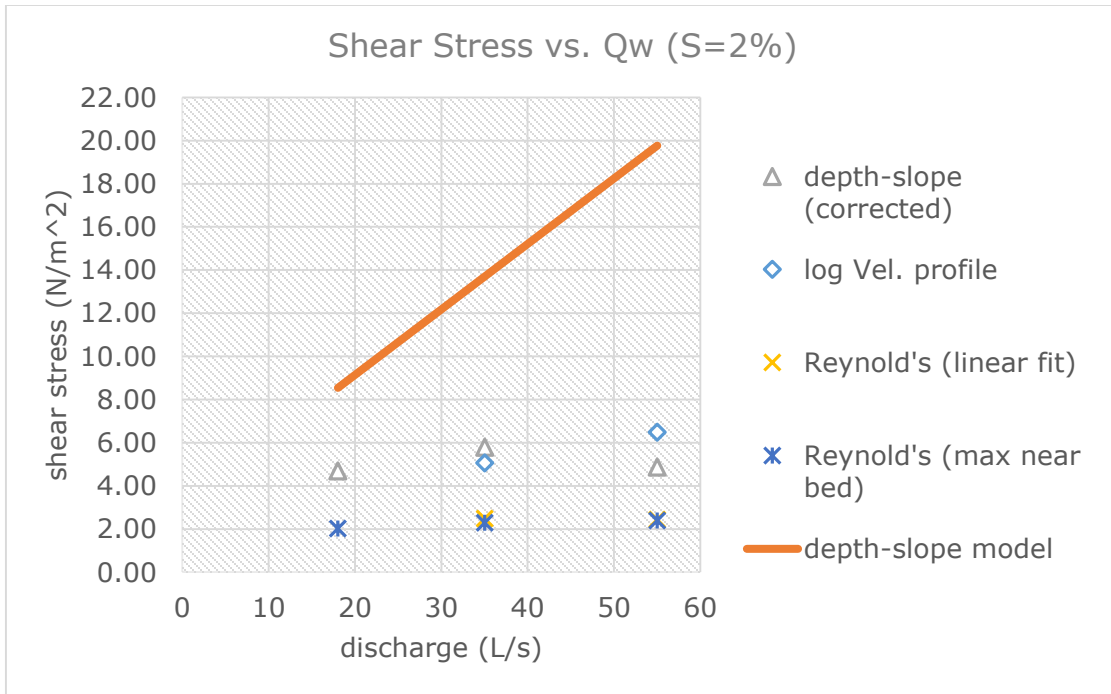
Figure 34: Shear stress vs. discharge as slope is held constant at 2%.
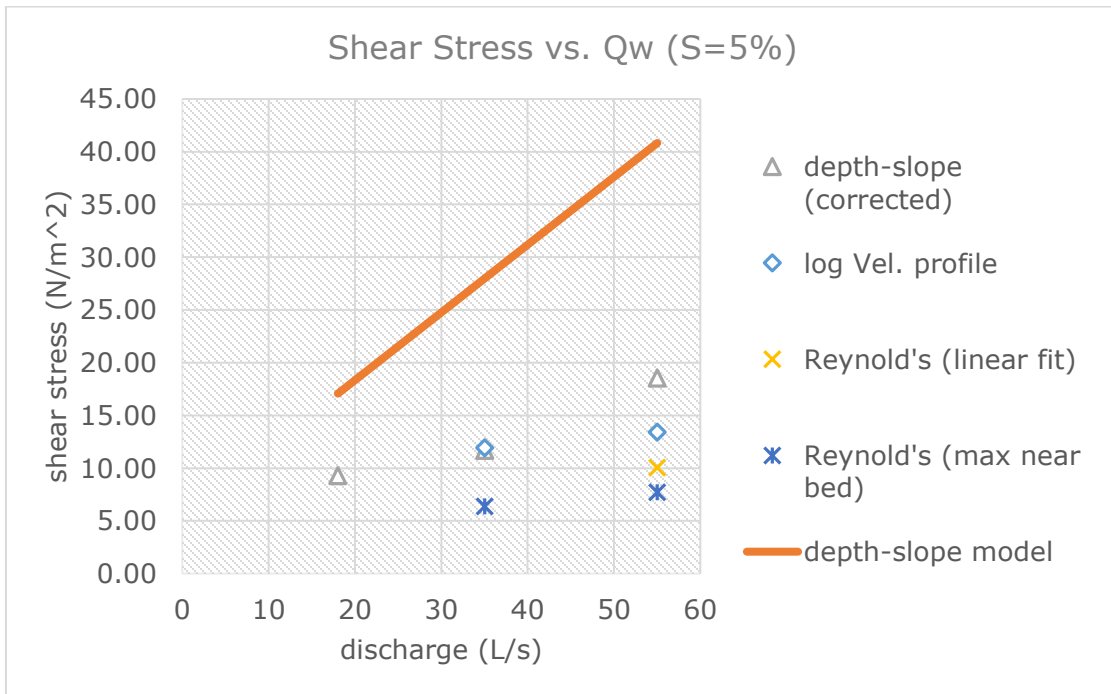
Figure 35: Shear stress vs. discharge as slope is held constant at 5%.
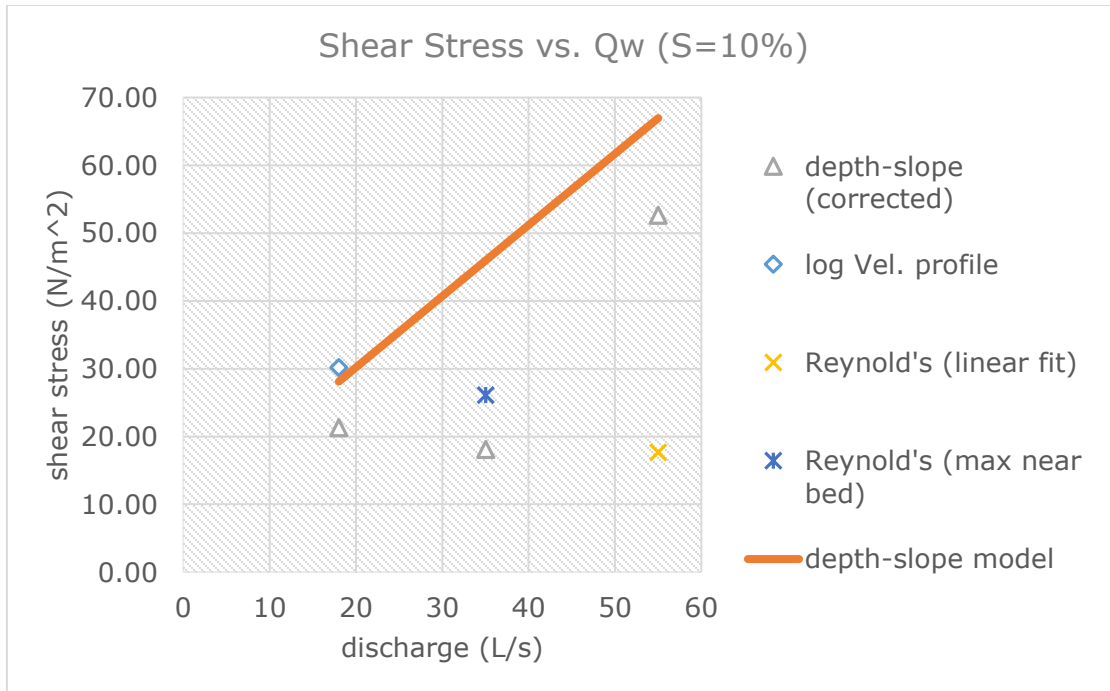
Figure 36: Shear stress vs. discharge as slope is held constant at 10%.

We can see that the depth-slope product greatly overestimates shear stress on this accelerating flow, and that shear stress does not appear to be affected by changes in Q_w. If shear stress is a meaningful metric for erosion, these flat lined trends explain the invariance of erosion to changes in discharge shown in previous plots.
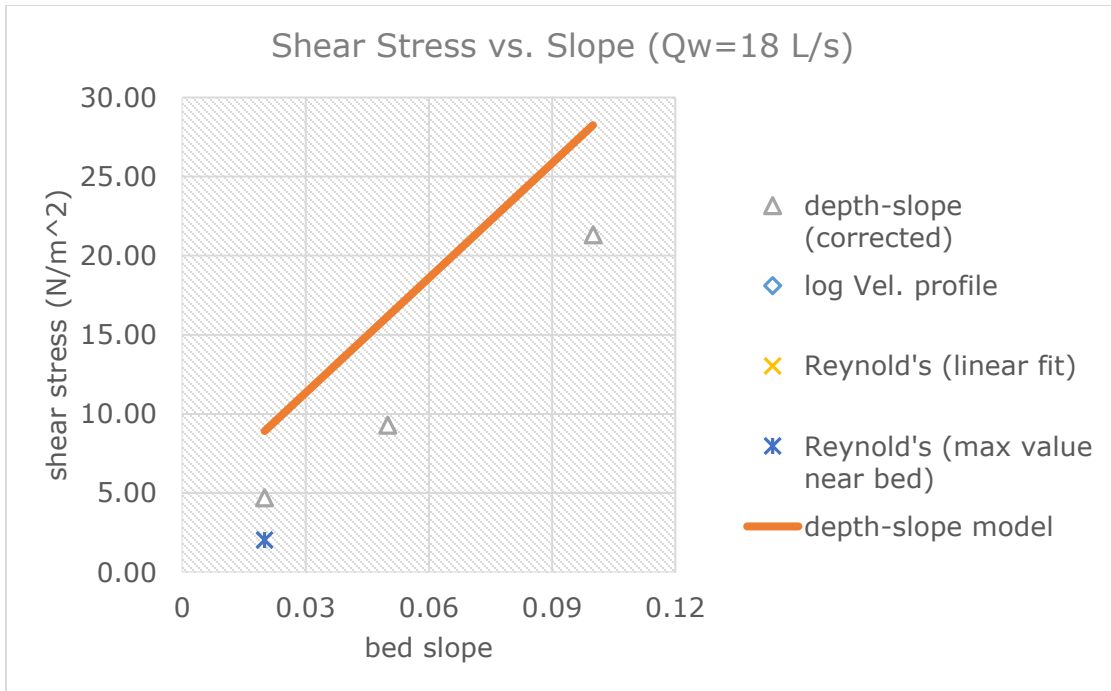
Figure 37: Shear stress vs. slope as discharge is held constant at 18 L/s.
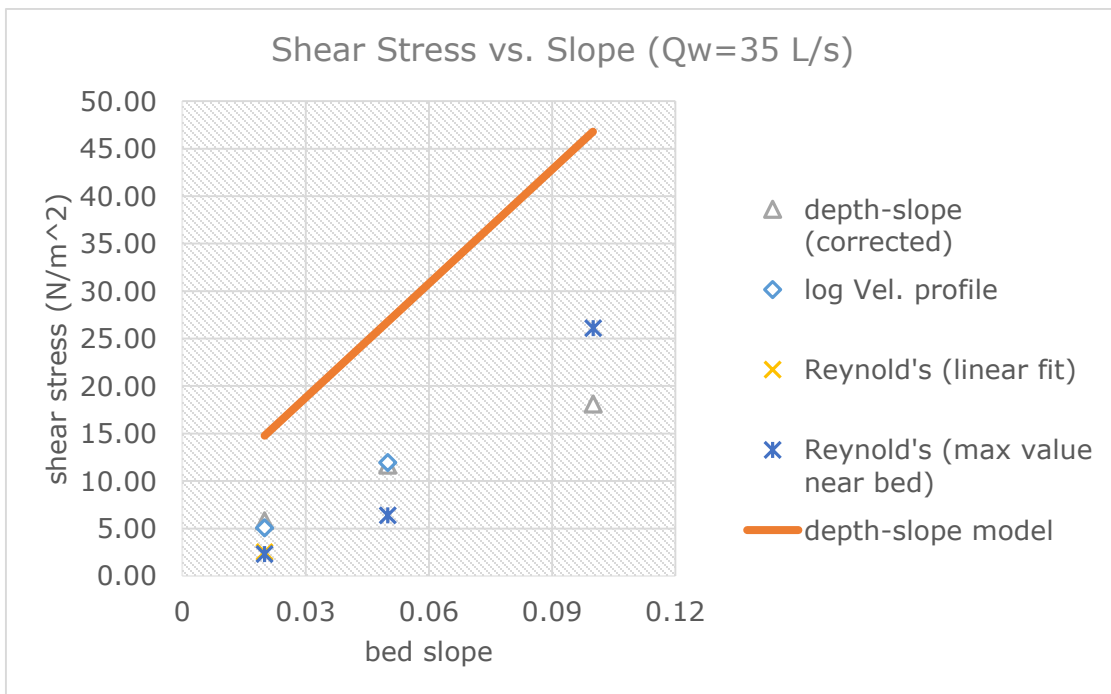
Figure 38: Shear stress vs. slope as discharge is held constant at 35 L/s.
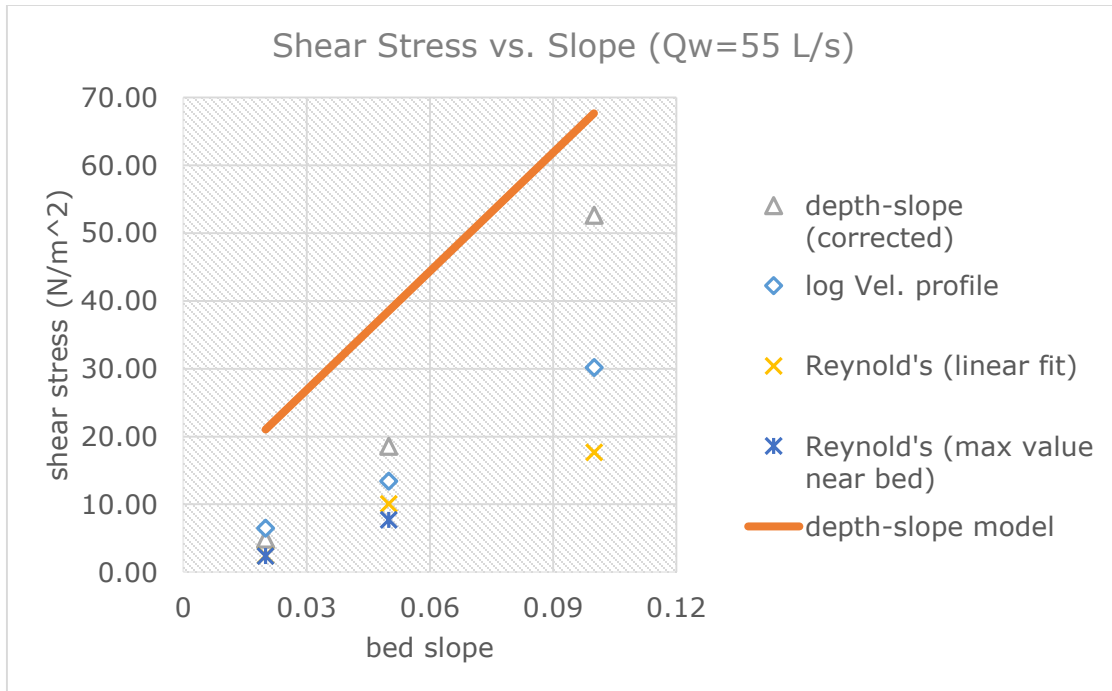
Figure 39: Shear stress vs. slope as discharge is held constant at 55 L/s.

Again contrasting the plots regarding discharge, shear stress is seen in Figures 37-39 to increase with slope. It's also interesting to note that this positive trend is strongest at lower discharges, but the reason for this is unknown. This relationship suggests a possible explanation to the earlier finding that erosion appear to vary with bed slope but not with flow discharge, ostensibly two ways to manipulate flow shear stress in this sort of experiment.

To conclude, my data shows that for these conditions, shear stress is unaffected by changes in discharge (Q_w), and increases monotonically with slope (S). It should be no surprise, if shear stress is a meaningful indicator of erosion, that the plots of E vs. Q_w and τ_b vs. Q_w should mirror each other, as should E vs. S to τ_b vs. S. Figures 40-41 below illustrate how discharge and bed slope affect shear stress, here as an average of multiple independent measurements. The 9 data points are a combination of 3 discharge and 3 slope control configurations, and together form the vast majority of all flow conditions used for erosion experiments in the flume. For

this reason, unless otherwise noted, these values of shear stress are used for all

other experimental runs of matching slope and discharge.
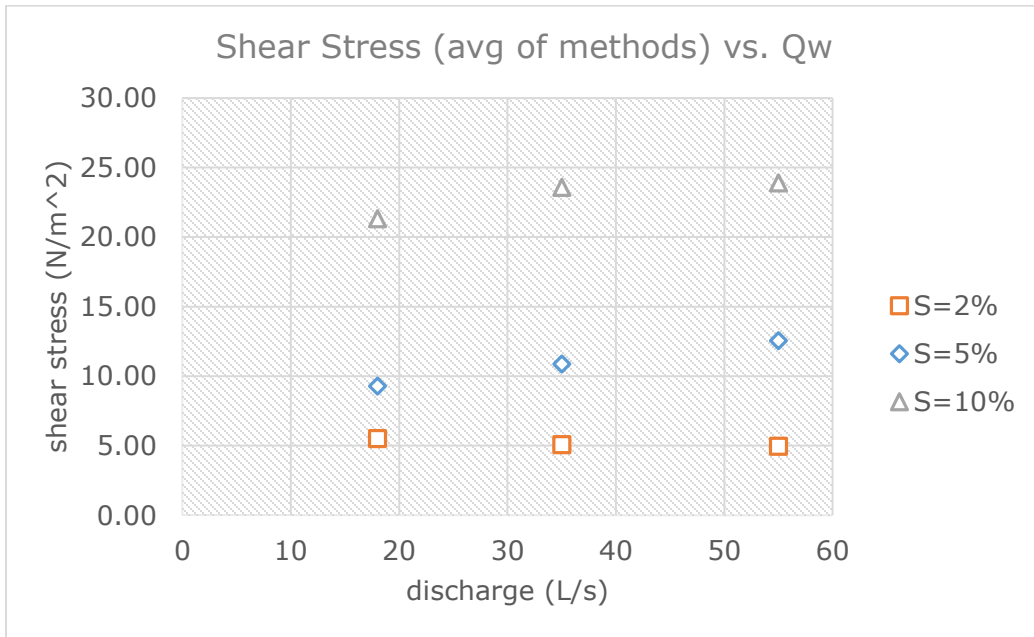
Figure 40: Shear stress vs. discharge, at varying slopes. Each value of shear stress is the average of multiple independent measurements.
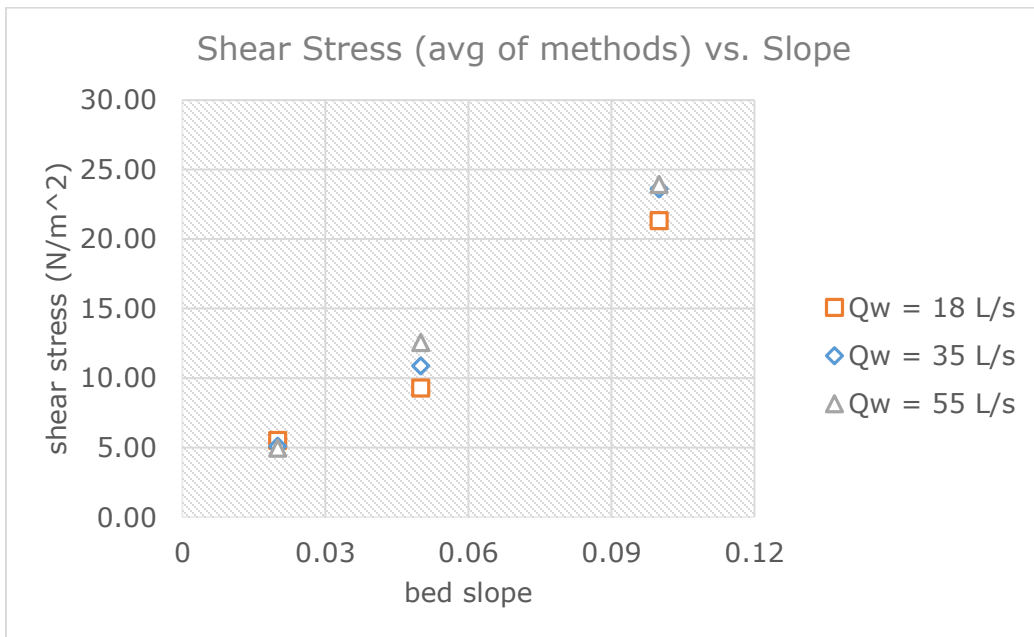
Figure 41: Shear stress vs. slope, at varying discharges. Each value of shear stress is the average of multiple independent measurements.

4.5: Erosion vs. Shear Stress (τ_b) under Ideal Conditions

In comparing erosion rates vs. shear stress, the work of *Johnson and Whipple* [2010] showed an invariant relationship, although their experiments could only vary discharge on a bed of fixed slope (6.5%) and had no way to test for potential flow acceleration nor directly measure and confirm an increase in shear stress at higher flow discharges.. This experiment shows this same conclusion [Figure 18] and in fact strengthens the argument, since the observation of invariance of erosion rate over a wide range of water discharge appears to be true across a range of bed slopes (2° – 10°). Interestingly, however, a consistent increase in erosion rates with increasing bed slope was found in our experiments.

Now that we have a reliable method of measuring shear stress we can finally see how erosion rate varies with shear stress for both changing water discharge and bed slope. The saltation-abrasion model of *Sklar and Dietrich* [2004] is specifically for a smooth, planar bed, so first the relationship between erosion and shear will be evaluated on only idealized smooth to semi-smooth bed roughness (each classification in Chapter 4.6).
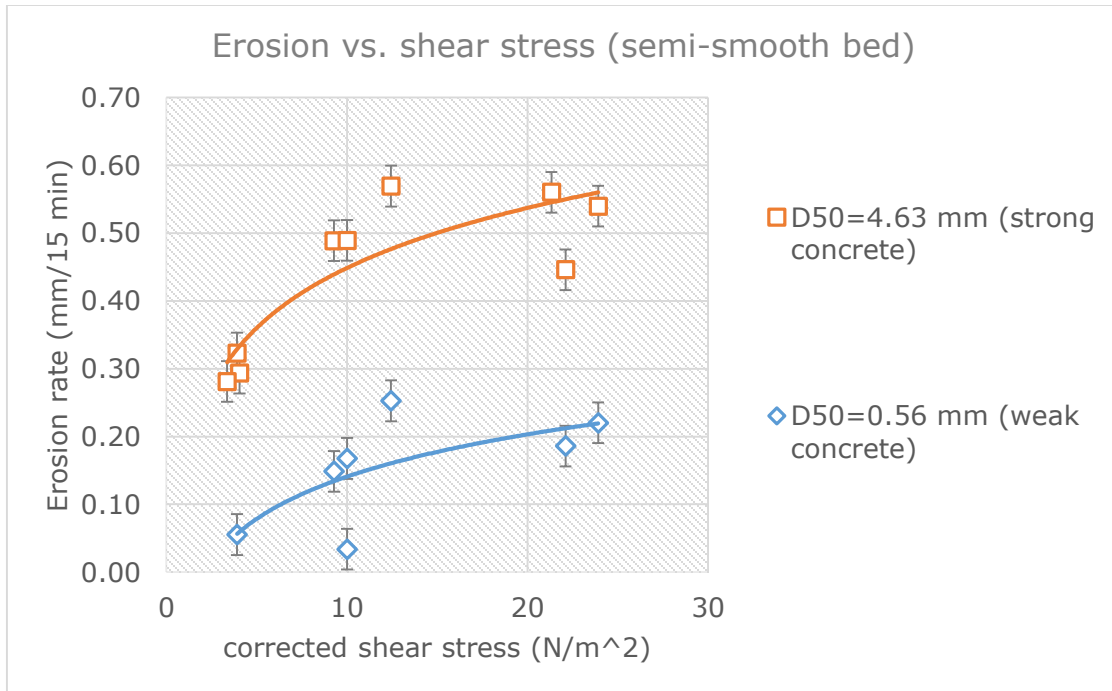
Figure 42: Erosion vs. shear stress on a semi-smooth bed. Insert 5 is of the stronger, 15:1 sand: cement ratio concrete (σ_T = 0.14 MPa), while Insert 10 is the much weaker 25:1 (σ_T = 0.05 MPa).

Figure 42 consists of the subset of experiments where a full range of shear stresses were obtained in consecutive experiments before a central channel (and therefore enhanced bed roughness) developed. As seen above, both data series represent a very clear increase in erosion rate with increasing shear stress. The rate of increase of erosion rate with shear stress is the same in both cases despite nearly a magnitude of difference in median grain size (D_{50}). To include the majority of experiment data that did not occur on a nearly smooth bed, the evolving morphology and roughness of the bed surface needs to be included, and ideally quantified.

4.6: Erosion vs. Bed Roughness and Other Considerations

Although the erodible concrete insert initially begins as roughly planar surface, it quickly begins form rills, grooves, and eventually deeply incised channels that will affect near bed shear stress in ways we can not directly measure and may complicate relationships predicted by the saltation-abrasion model of *Sklar and*

Dietrich [2004] theorized for a smooth bed (e.g., Johnson and Whipple, 2010). The insert walls containing the concrete are a hard, smooth Plexiglas, but still create enough drag to direct momentum towards the center of the flume which likely initiates the rapid channelization. Documentation of bed roughness was largely qualitative at the time of each experiment, and only in later analysis quantified with using the standard deviation of bed elevation in the test section. Images of the range of roughness are included below as Figures 43-46.

Figure 43: Smooth bed

Figure 44: Semi-smooth bed

Figure 45: Semi-rough/rough bed

Figure 46: Very rough bed

The largest contributor to increasing roughness is the formation of a typically single, large channel. Once a channel was created, a positive feedback was observed in that bed load particles were more likely to be transported along this low in the topography, thus concentrating erosion in the axis of developing grooves. When this central channel becomes too deep or with overhanging banks (prevents accurate erosion scanning), the insert may be drastically altered by hand to create a semi-smooth surface again. This is done my manually carving the outer banks down to be level with the inner channel [Figure 47]. Other roughness features include sharp erosional features from experiments nearing suspended transport [Figure 48] and hardened cement nodules that are sometimes present in some inserts but does not appear to affect tensile strength. When these features start to stick out, or look brittle, they are shaved down by hand and a new "zero" scan is made of the bed surface. Later concrete inserts were periodically smoothed by hand to delay the inevitable development of deep grooves so that a greater assortment of flow

conditions could be used more often at low roughness. As an additional benefit, this proved to prolong the useful lifespan on the inserts, since further scanning is halted when erosion reaches the underlying Plexiglas container.

The scale of roughness elements seems to correlate with the size of sediment. The gravels used in the flume created smooth edges, deep channels, and a general undulating pattern of erosion intensity (a hop length correlation). On the other hand, the smallest sediment size (D_{50} = 0.56 mm) was found to form sharp, delicate grooves and a tendency to undercut existing features, somewhat limiting our ability to measure erosion.

Figure 47: High roughness bed form half-way through manual carving away of outer channel banks.

Figure 48: Sharp erosional facets created from repeated erosion experiments using smallest sediment (D_{50} = 0.56 mm), which hovers near the transition between suspended and saltation transport modes.

Roughness was quantified as the standard deviation of elevation, because although simple, this simple metric of roughness is effective. Figures 51 and 52 show a strong negative correlation between erosion rate and roughness, but interestingly, Figure 50 appears to lack any sort of trend (perhaps due to the unique transport mode near the threshold of suspension for this grain of D_{50} = 0.56 mm).
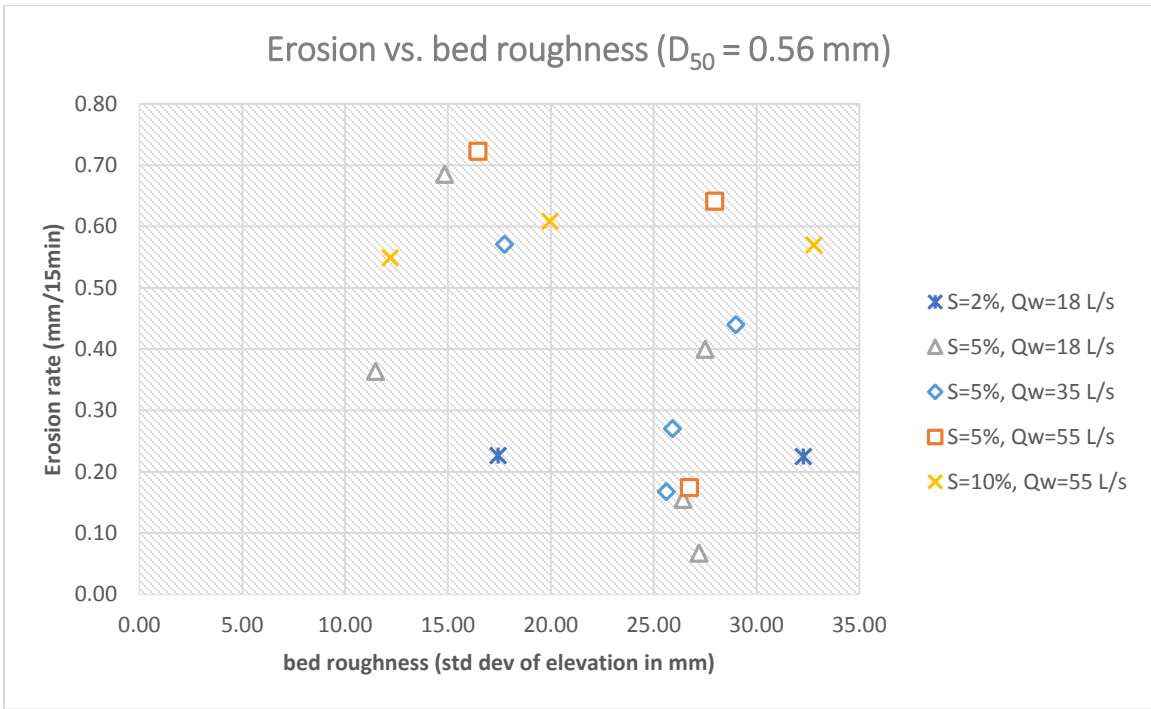
Figure 49: Erosion vs. bed roughness for the smallest sediment grain (D$_{50}$ = 0.56 mm). Unlike the plots for the larger grains, these sands show no obvious correlation to increasing bed roughness.
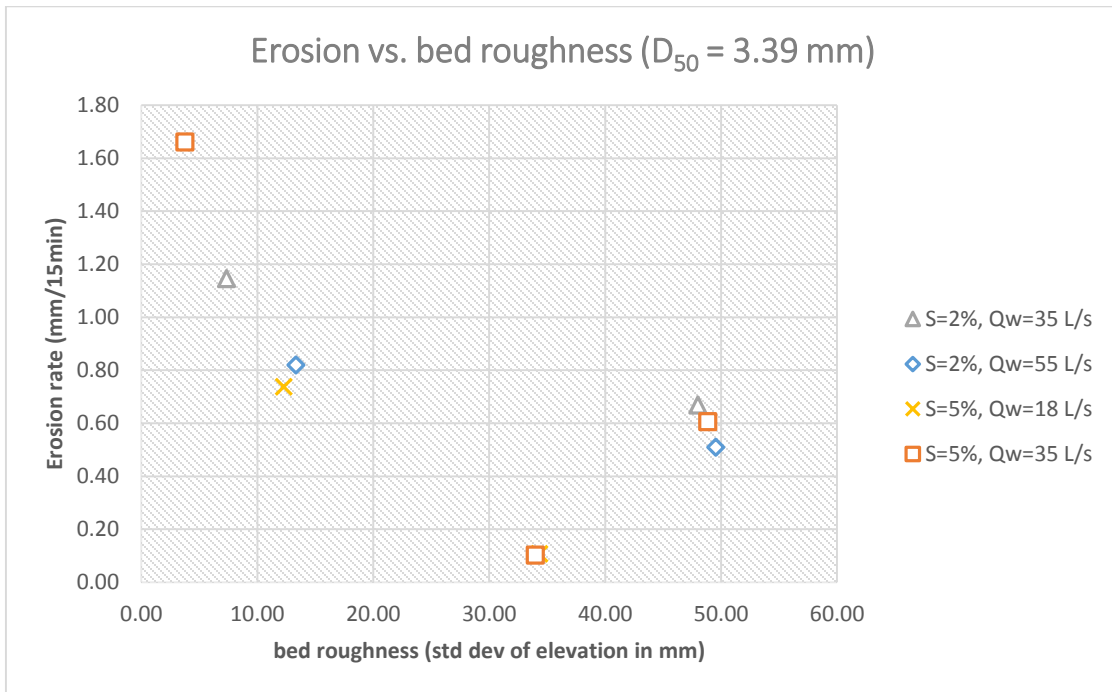
Figure 50: Erosion vs. bed roughness of smallest gravel (D$_{50}$ = 3.39 mm), showing a strongly negative relationship.
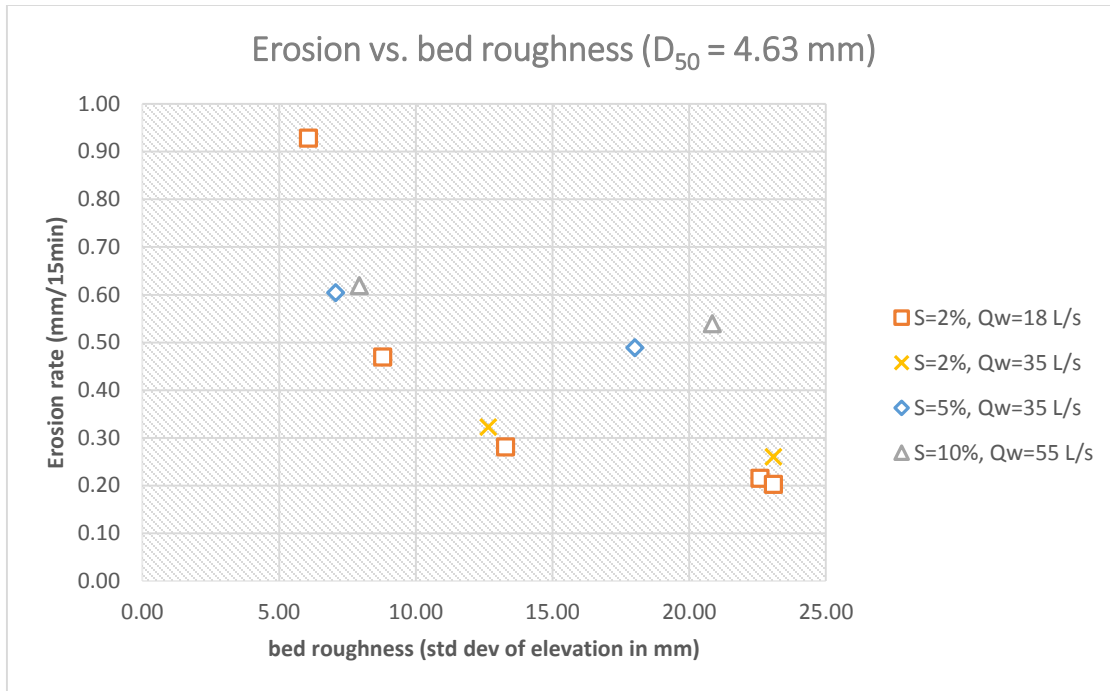
Figure 51: Erosion vs. bed roughness of the medium gravel (D_{50} = 4.63 mm), showing a strongly negative relationship.

Erosion rates were found to generally decrease with increasing roughness, which contradicts *Johnson and Whipple, 2010*, where it was hypothesized a larger component of velocity normal to a bed during saltation trajectory would be more likely to occur on a bed with high roughness. In the case of this flume, it may be possible that the deep, narrow channels simply slowed the saltating grains, but not enough to initiate alluviation.
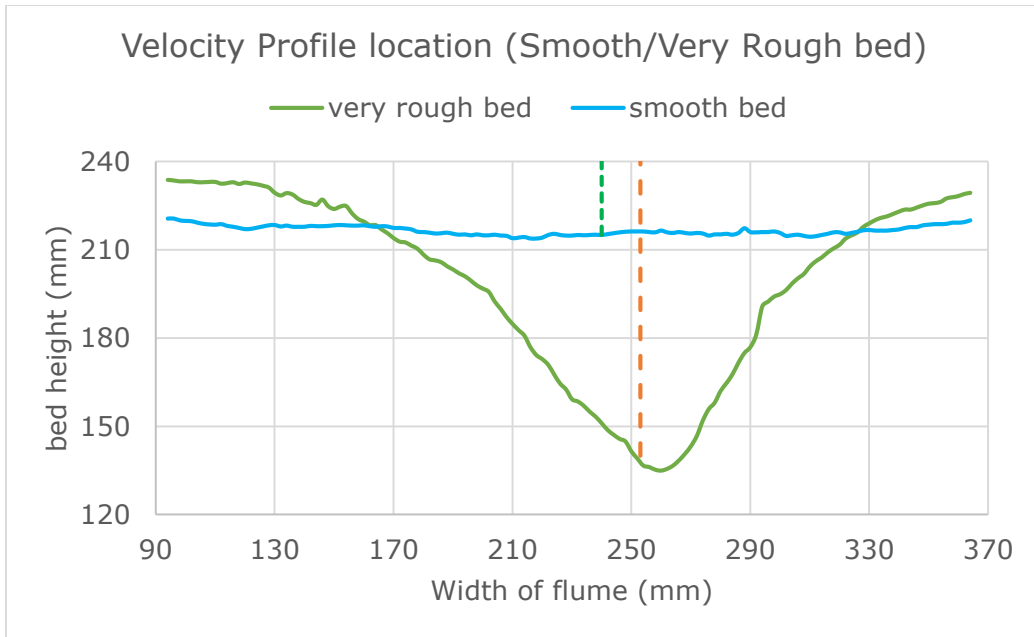
Figure 52: Cross-section of flume insert at smooth and rough bed conditions. Dotted line shows locations of ADV probe used to measure shear stress.
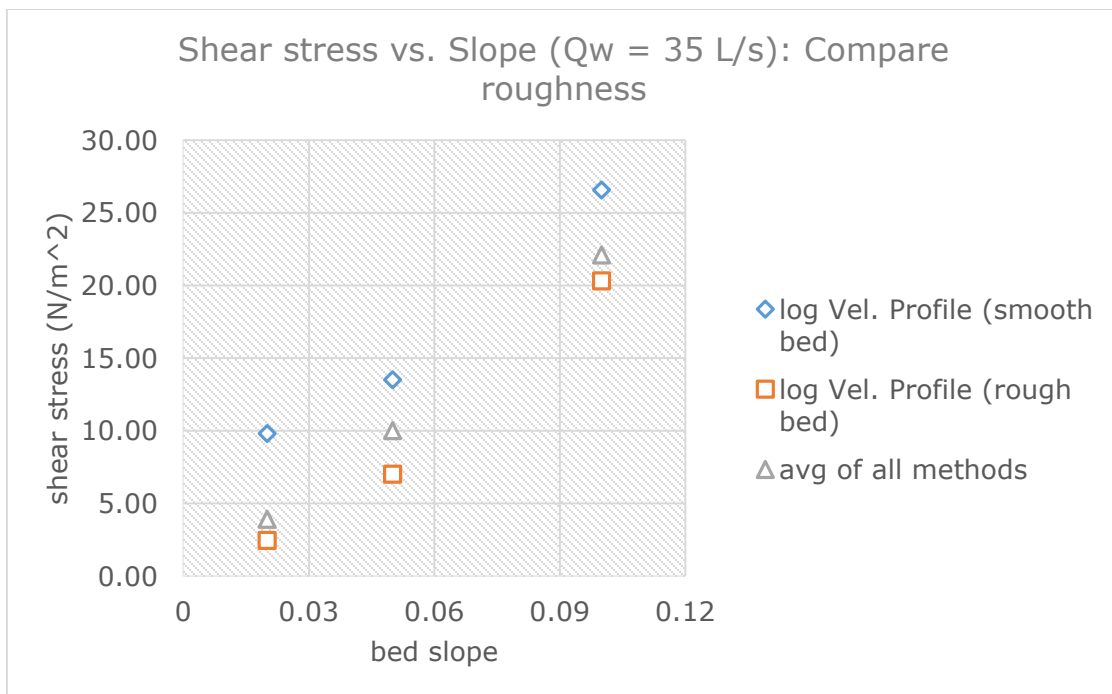
Figure 53: Shear stress vs. slope at Qw=35 L/s. The shear stresses measured from a rough bed were noticeably lower than from a smooth bed, but the relationship to slope is similar.

4.7: Erosion vs. shear stress considering all conditions

With an accurate measure of shear stress for all flow conditions, and recognition that bed roughness strongly influences erosion rates, we can look at all other erosion experiments where any flow conditions are varied, and at least categorize our data by different roughness values. Figures 54-58 showcase erosion vs. shear stress for each grain size used in all experiments, and each data set if separated by relative roughness. Without these distinctions, much of the data would look orderless, but now most data sets show a monotonic increase in erosion rate with increasing shear stress similar to the relationships seen in Figure 42 as long as bed roughness is similar.
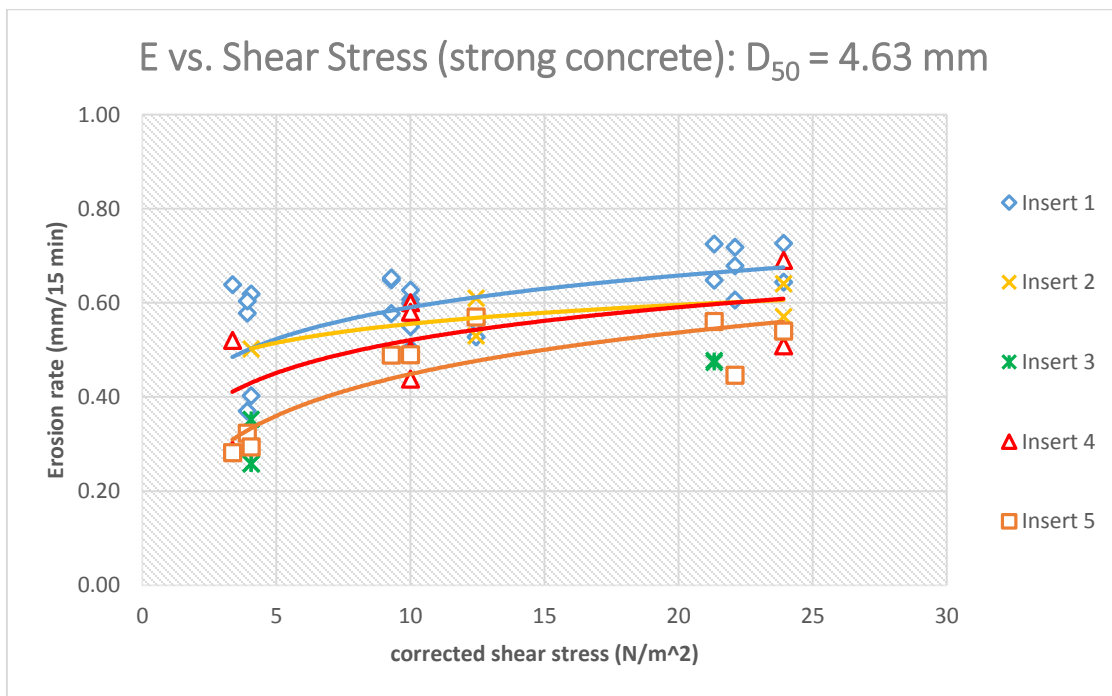
Figure 54: Erosion vs. corrected shear stress, across a variety of concrete inserts and changing roughness.

Here we can see a clear relationship in erosion vs. shear stress, even while largely ignoring differences in roughness (each set of data may contain a range of roughness). While there is insufficient data to compare the same relationship with other grain sizes on the strong concrete inserts, later experiments were specifically

designed to use a weaker concrete to find results (i.e. erosion experiments using D_{50} = 0.56 mm were indistinguishable from zero-erosion runs for experiments of even 30+ minutes in duration).
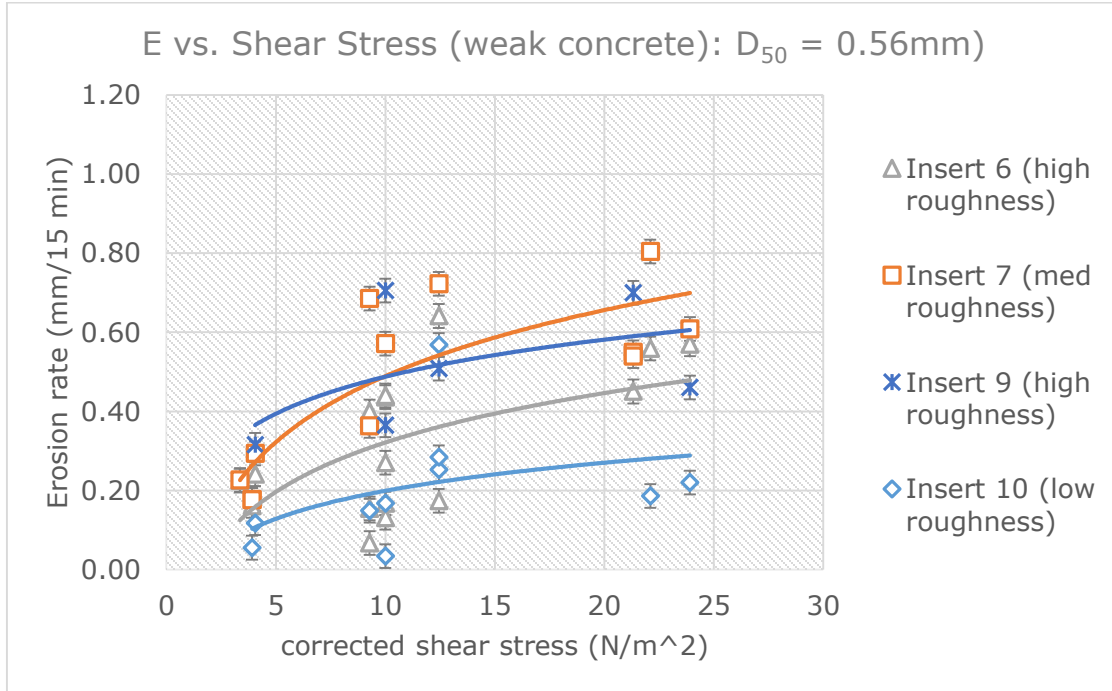
Figure 55: Erosion vs. shear stress on weak concrete for D_{50} = 0.56 mm. Data sets are separated by roughness.
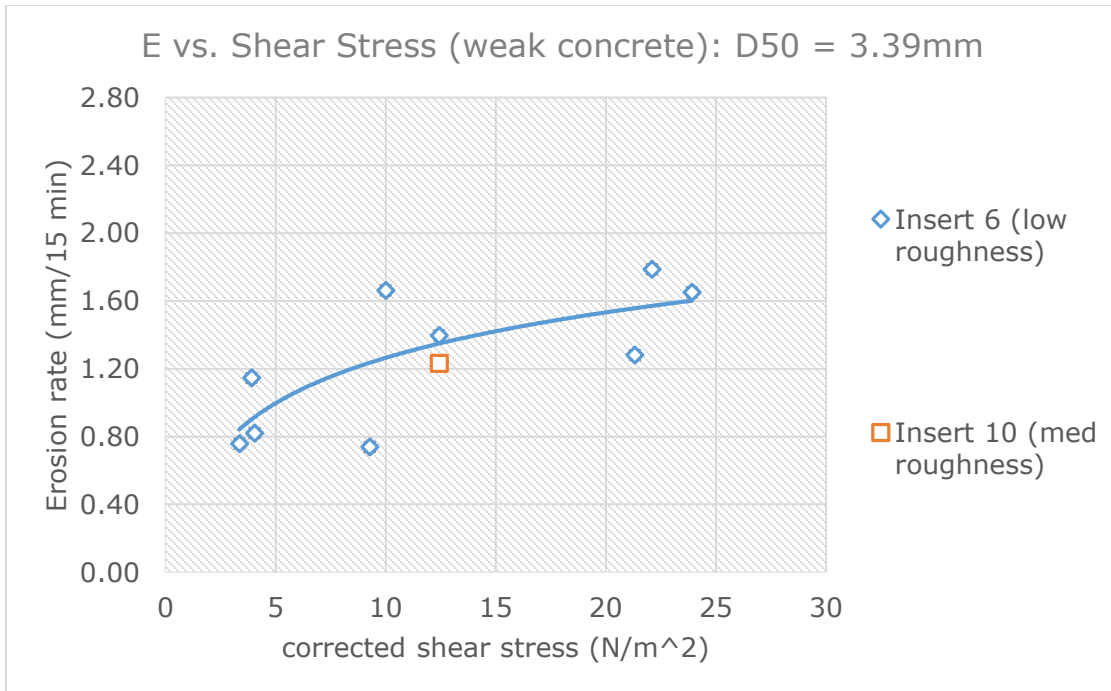
Figure 56: Erosion vs. shear stress on weak concrete for D_{50} = 3.39 mm. Data sets are separated by roughness.
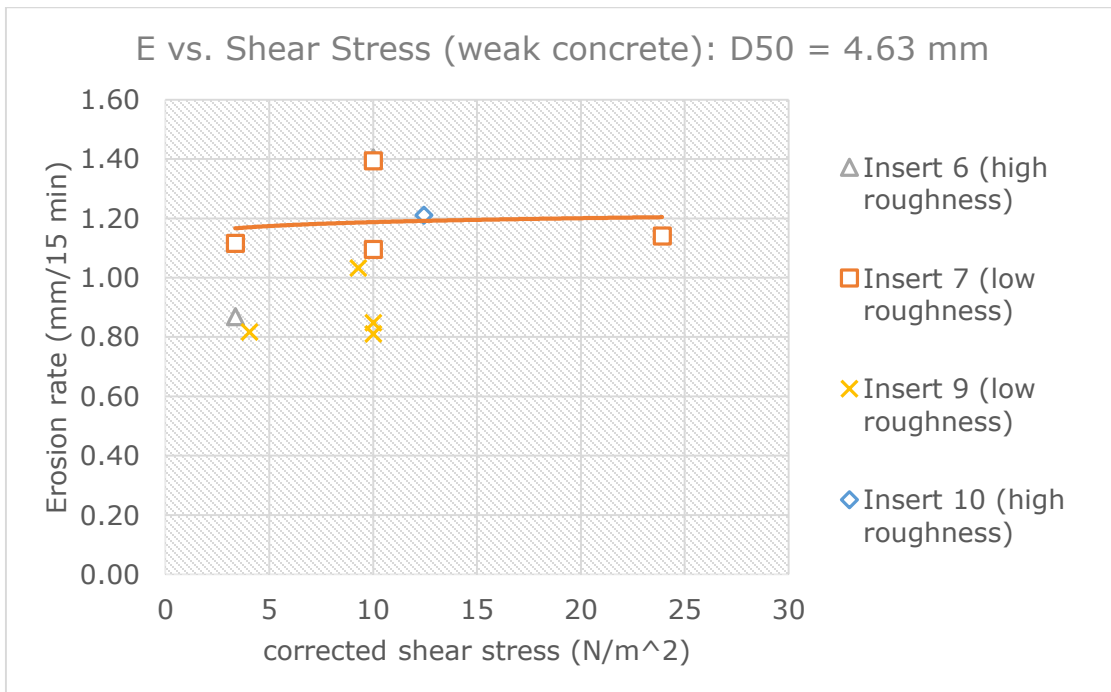
Figure 57: Erosion vs. shear stress on weak concrete for D50 = 4.63 mm. Data sets are separated by roughness.
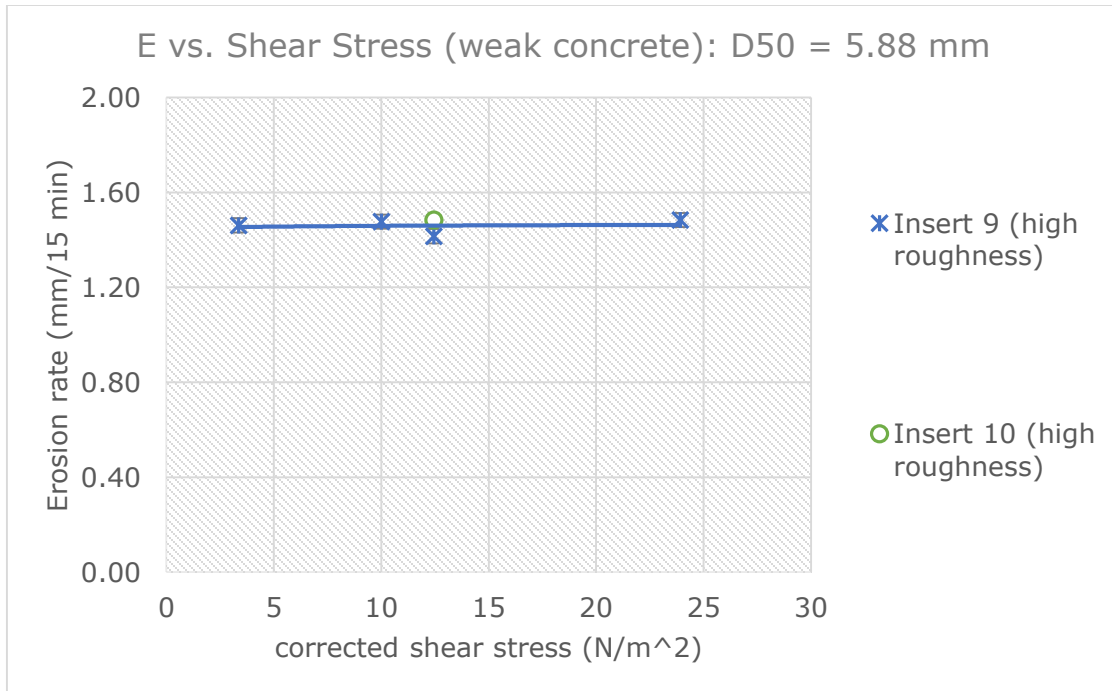
Figure 58: Erosion vs. shear stress on weak concrete for D50 = 5.88 mm. Data was not available for varying stages of roughness.

The sand abrasion experiments were given special attention, as they hover near the transition zone between suspended and saltating transport processes. These experiments were surprisingly consistent with experiments with coarser sediment, since there was an expectation that erosion rates would decrease rapidly as particles go into suspension [Sklar and Dietrich, 2004; Lamb et al., 2008?]. In Figure 59, however, we see that flow conditions previously calculated to create some degree of suspension were narrowly out of range (after accounting for flow acceleration).The erosion rates are greatly reduced in magnitude compared to the bedload runs, but that was expected according to *Sklar and Dietrich [2004]; Lamb et al [2008] and Scheingross et al [2014]* and may reflect the decrease in mass and kinetic energy flux more than any potential change in mode of transport*.*

67
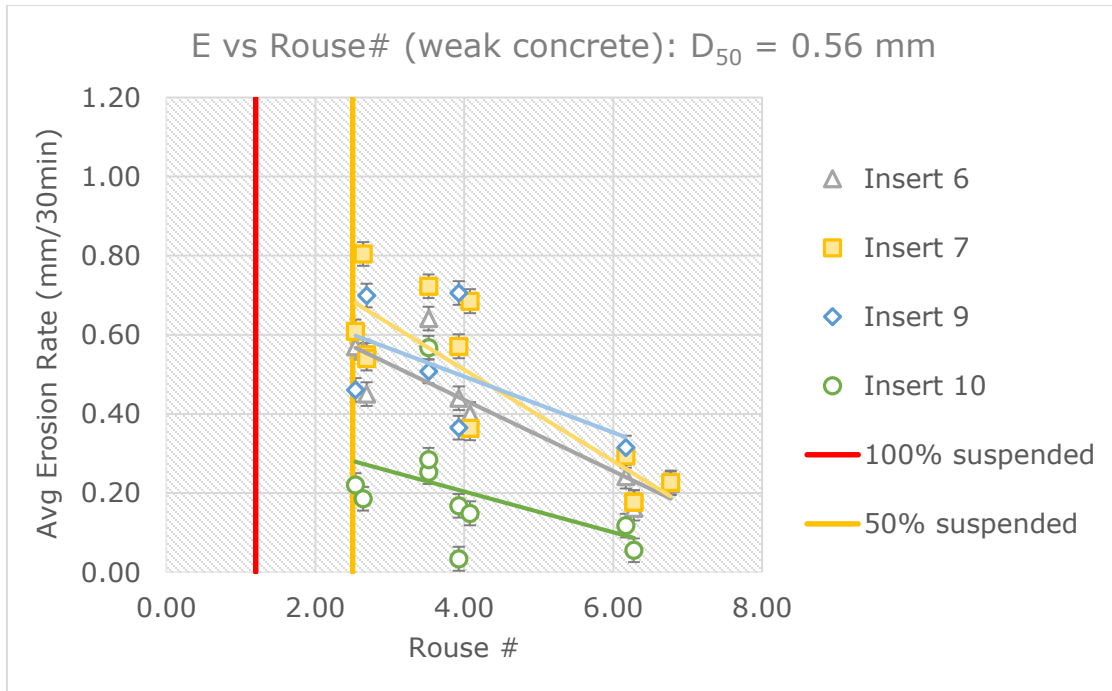
Figure 59: Erosion vs. Rouse number shows the strongest trend when considering the smallest grain size (D_{50} = 0.56 mm). Bedload transport is defined at P > 2.5, and below that varying degrees is suspended transport.

Most importantly, we want to compare our results of erosion vs. shear stress with the saltation-abrasion model (Sklar and Dietrich, 2004; Lamb et al. 2008) as it represents the state of the art for process-based models of river incision by abrasion. Assuming no bed cover, and no onset of suspension this model can be simplified to:

$$E = K \, q_s \left(\frac{\tau^*}{\tau_c^*} - 1 \right)^{-0.5} \tag{9}$$

This predicts that erosion rate will decrease with shear stress in excess of that required to initiate grain transport (the decline with shear stress is predicted to further increase with the onset of suspension). We can compare this equation to our data, knowing that it's not so important that the data matches perfectly, more that the trend and trajectory of the data matches similarly (as the constant "K" could have an increasingly complex calculation to match perfectly with our conditions, as so many factors are bundled therein).
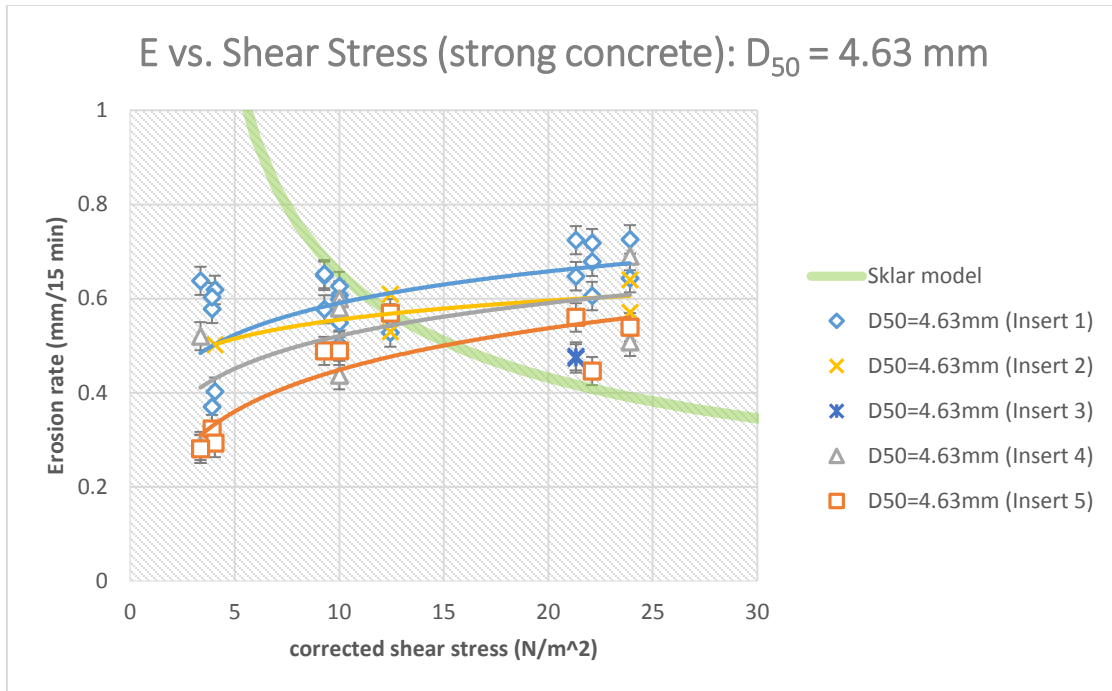
Figure 60: Erosion vs. shear stress on strong concrete, compared to saltation-abrasion model. Each data series represents erosion experiments across a range of roughness for each concrete insert.

Even across a wide range of individual inserts and roughness values, none of our data matches the prediction by the Sklar model [Figure 60]. While the saltation-abrasion model of *Sklar and Dietrich* [2004] predicts a power-law decay of erosion rate as shear stress increases, experimental data shows a non-linear but positive trend. To further push the issue, Figures 60-63 include all other grain sizes on the weaker concrete bed and are also compared to the saltation-abrasion model of *Sklar and Dietrich* [2004], and we find the same general result.
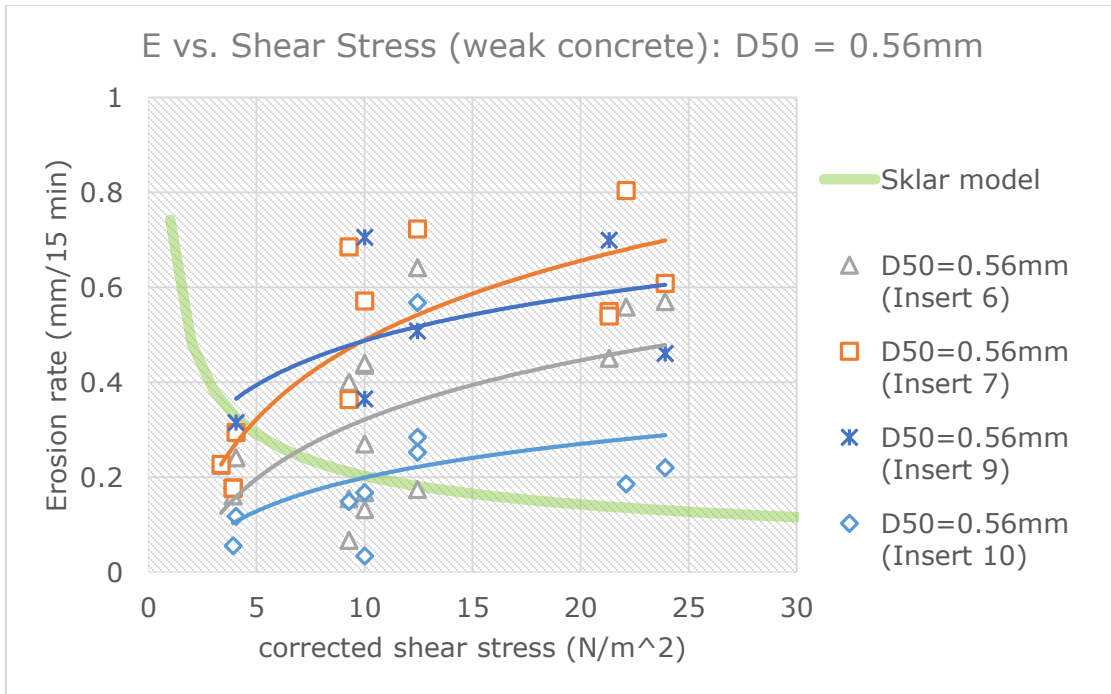
Figure 61: Erosion vs. shear stress on weak concrete, compared to the saltation-abrasion model of Sklar and Dietrich [2004] for D_{50} = 0.56 mm.
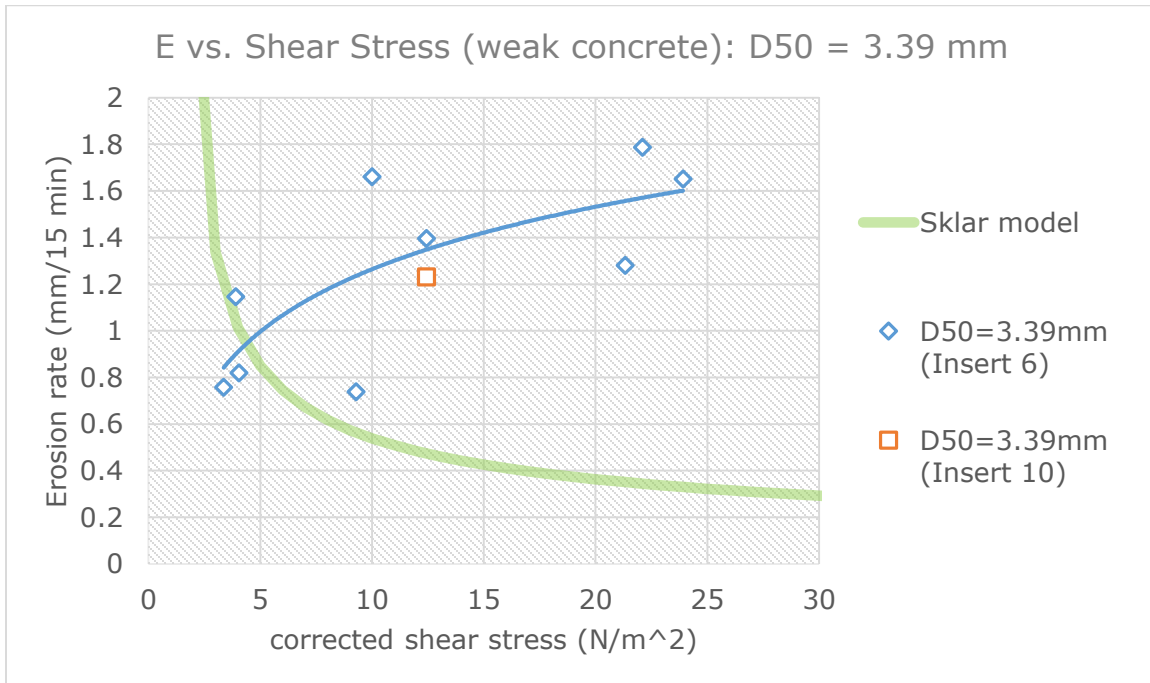
Figure 62: Erosion vs. shear stress on weak concrete, compared to the saltation-abrasion model of Sklar and Dietrich [2004] for D_{50} = 3.39 mm.
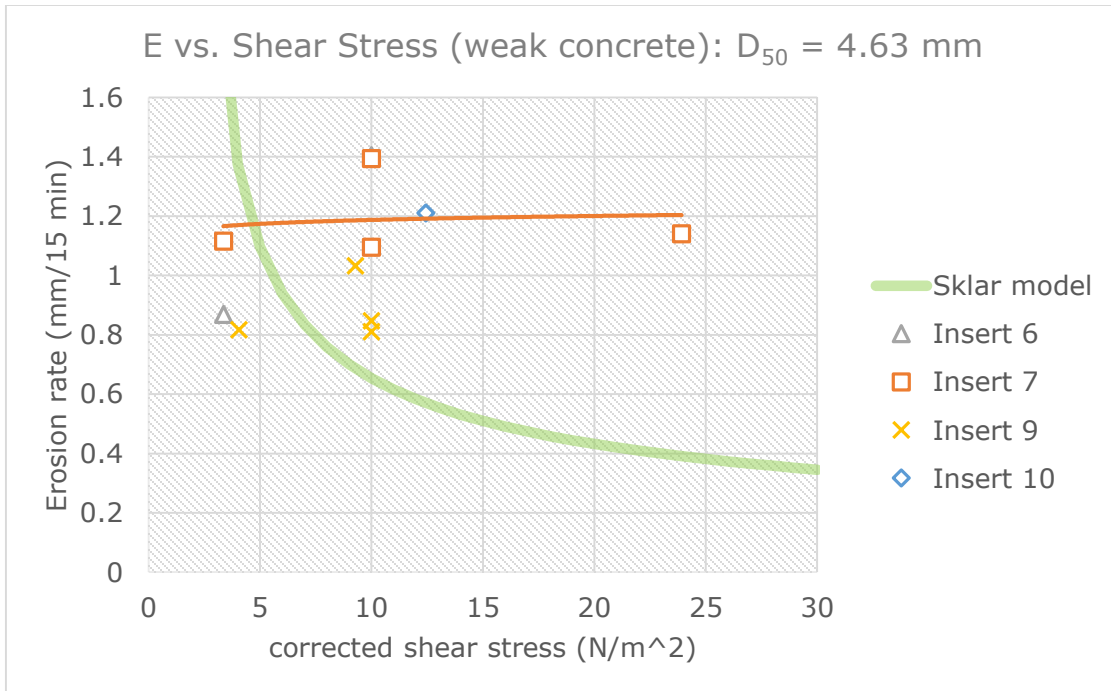
Figure 63: Erosion vs. shear stress on weak concrete, compared to the saltation-abrasion model of Sklar and Dietrich [2004] for D50 = 4.63 mm.
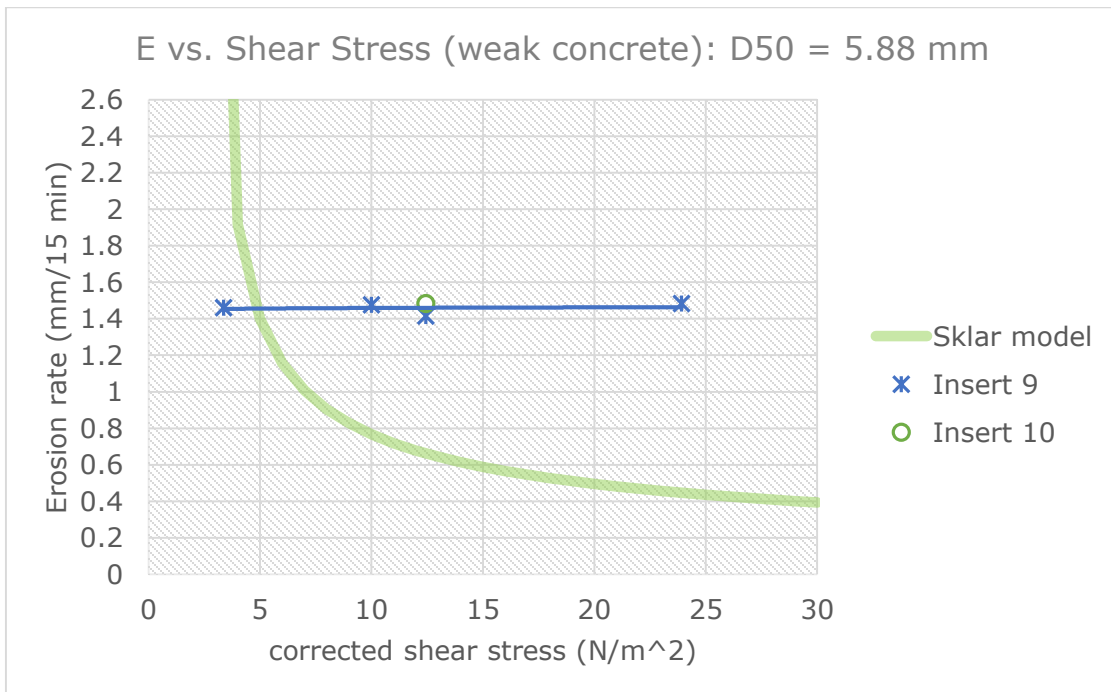
Figure 64: Erosion vs. shear stress on weak concrete, compared to the saltation-abrasion model of Sklar and Dietrich [2004] for D50 = 5.88 mm.

4.8: Erosion vs. Mean Grain Diameter (D_{50})

Grain sizes in these experiments order over a degree in magnitude, technically, but 3 of the 4 were relatively close in size. Figure 64 shows the distribution of particle sizes and a note of the D_{50} of each.
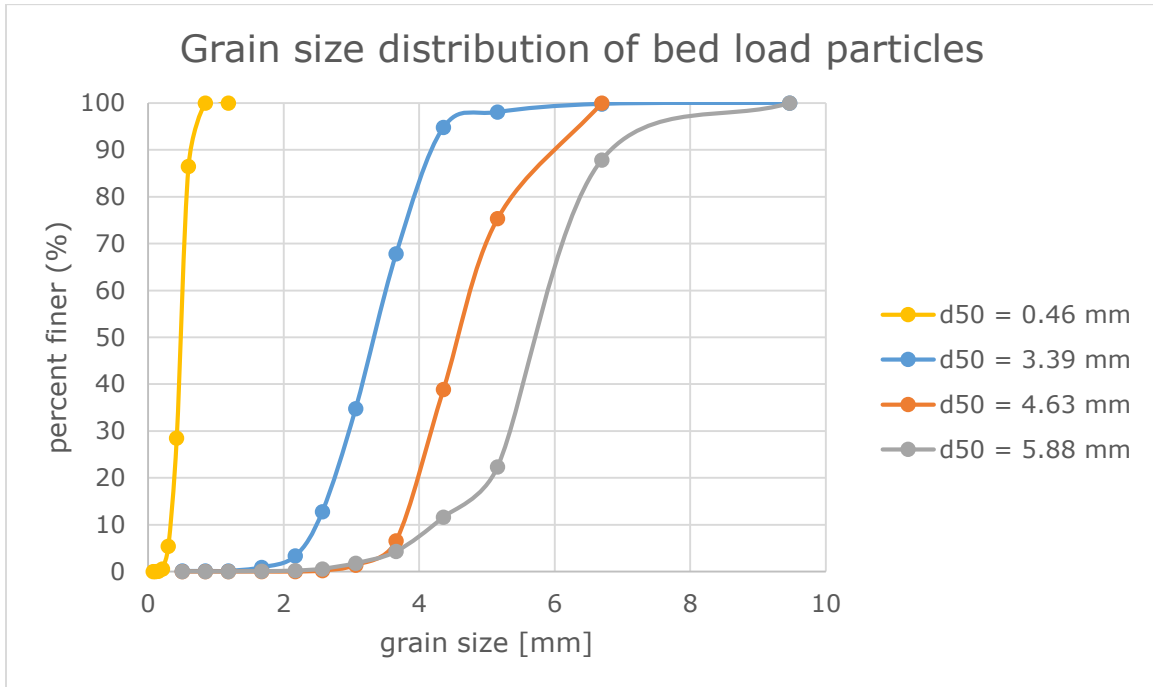
Figure 65: Sieve analysis of grains used for bedload abrasion. Median grain size can be inspected visually by drawing a line from the y-axis at 50 (% finer) to where it intersects the curve of any of the different grain size species

Besides the decrease in erosion rates with the square root of excess shear stress, the other concept implicitly derived from the simplified saltation-abrasion model of *Sklar and Dietrich* [2004] is that erosion should positively scale with increasing median grain diameter of the saltating bed load (D_{50}), seen here as in increase in τ_c^* to a – ½ power.

$$E = K\, q_s \left(\frac{\tau^*}{\tau_c^*} - 1\right)^{-0.5} \qquad\qquad (9)$$

Below this, plots of erosion vs. grain size are plotted with data series varying bed slope (Fig. 66-68). Since we've established Q_w has not increased shear stress as expected, there is no value to a bunch of graphs with points plotted on top of each

other, so those figures were excluded
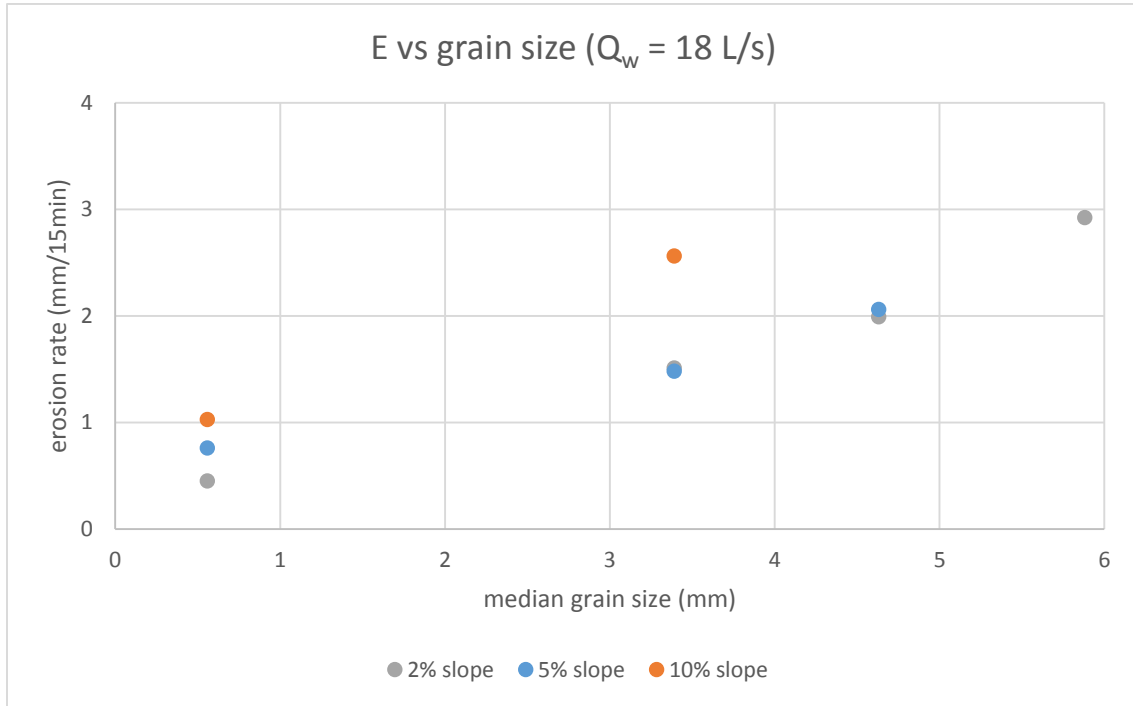
Figure 66: Erosion vs. grain size at Q_w = 18 L/s. Each data series represents a different bed slope.
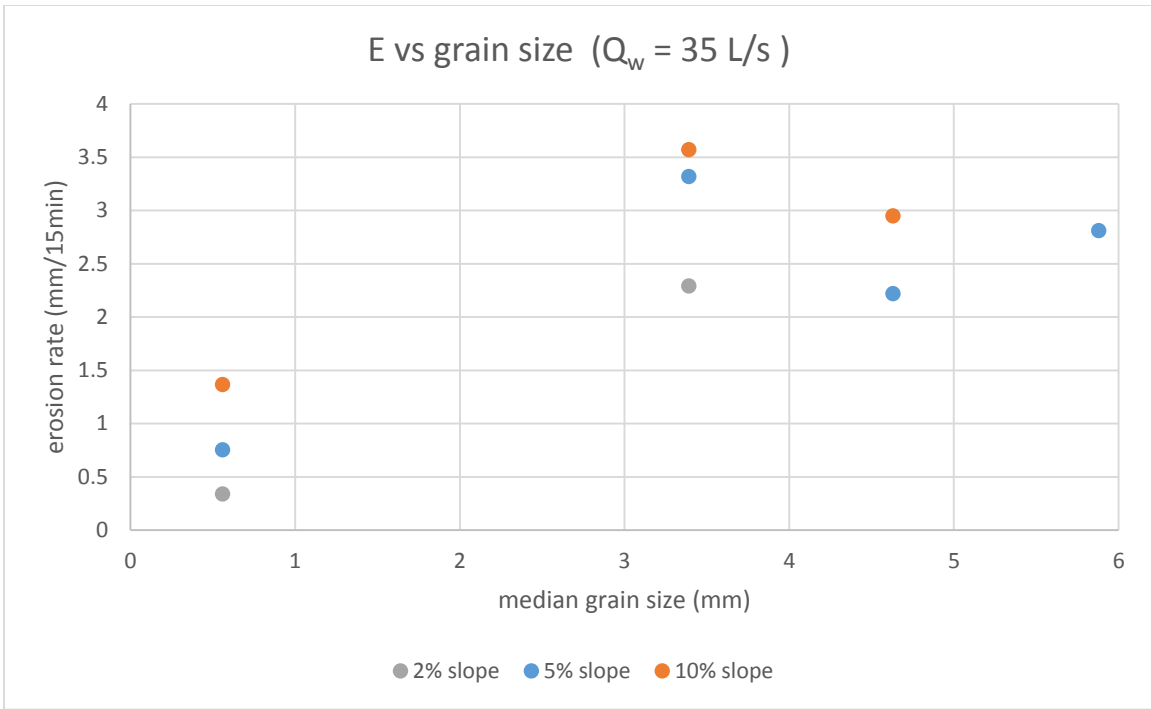
Figure 67: Erosion vs. grain size at Qw = 35 L/s. Each data series represents a different bed slope.
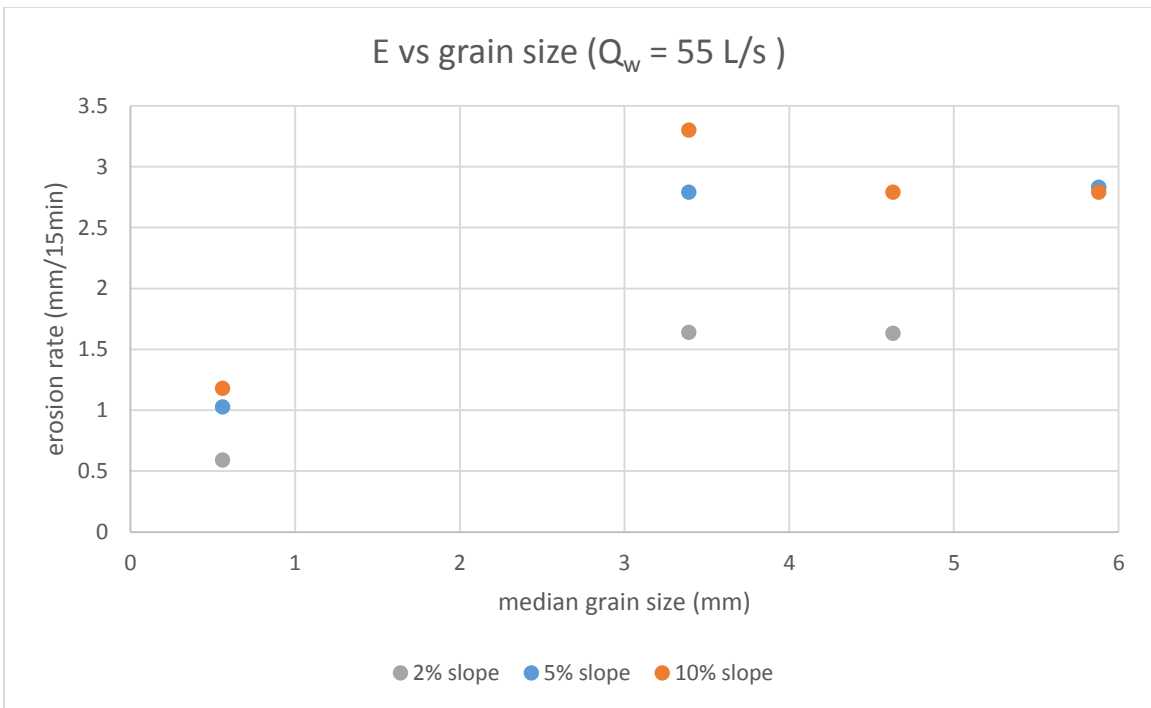
Figure 68: Erosion vs. grain size at Qw = 55 L/s. Each data series represents a different bed slope.

The figures above illustrate the relationship between erosion rates and grain size across different values of bed slope. Each plot is separated by different values of flow discharge, but all use a sediment flux equal to 100 grams per second ($Q_s = 100$ g/s). Comparing erosion rates within each grain size class, a persistent trend of increased erosion with bed slope is observed (i.e. bed slopes of 10% consistently yield erosion numbers greater than those at 5%, and those should be greater than 2%). It could also be argued that we can see either a slight positive trend of erosion vs. grain size, or an invariant trend among the 3 largest grains and an outlier at the smallest. It appears that the relationship of E vs. D_{50} is most positive at lower flow stages, though the reason is unknown.

Note that the sand ($D_{50} = 0.56$ mm) generates much lower rates than the larger gravels, and that the largest gravel ($D_{50} = 5.88$ mm) generates the highest erosion rates. The relationship between those 2 data series in that range of grain sizes is not well-understood. The medium gravel ($D_{50} = 4.63$ mm) persistently created lesser erosion rates than the smallest gravel ($D_{50} = 3.39$ mm). This pattern is also observed in plots of erosion vs. grain size in other flow conditions (variations in water discharge and slope), but the trend appears to weaken as flow velocity increases [Figures 66-68].

But more importantly, Figure 69 compares erosion rate vs. D_{50} of our results with the the saltation-abrasion model of *Sklar and Dietrich* [2004]. The data series are color-coded to the different values of sediment flux (Q_s) for experiment/model comparison. Flow stage of each of these data points is S = 5%, $Q_w = 55$ L/s.

75
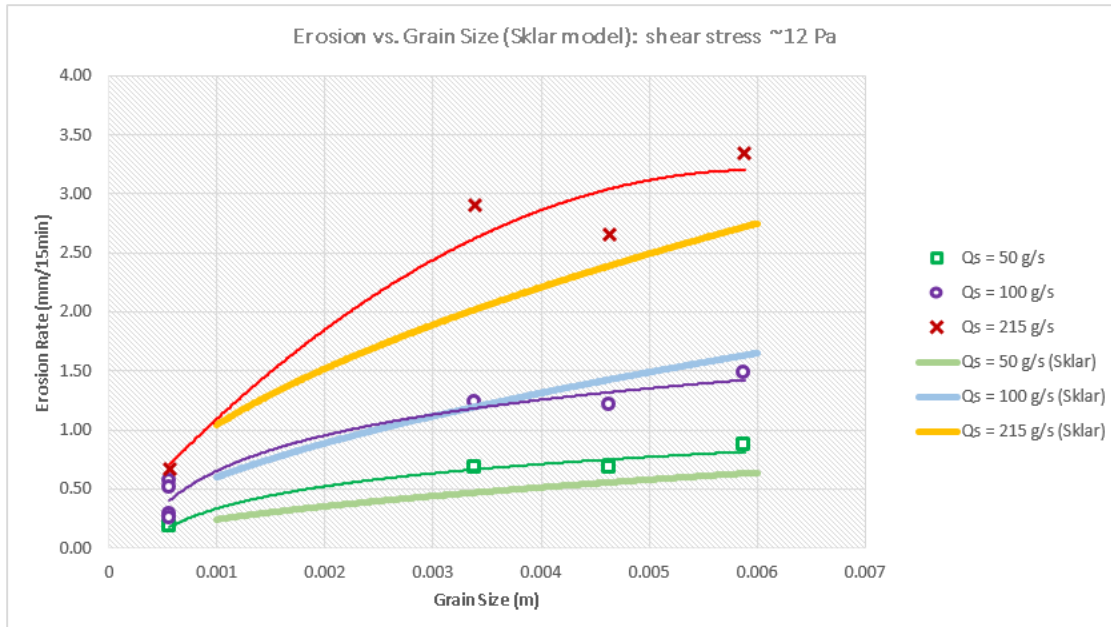
Figure 69: Erosion vs. median grain diameter on weak concrete, compared to the saltation-abrasion model of Sklar and Dietrich *[2004] for* $\tau \sim 12\ Pa.$

With some manual tweaking of the coefficients to the saltation-abrasion model of

Sklar and Dietrich [2004], these results mesh fairly well with the theoretical model

(for purposes of confirming that the relationships between the experiment and the

model are consistent). All points plotted here were configured to a slope = 5% and

Q_w = 55 L/s. Barring any extreme roughness conditions, this gives a shear stress

value of 12.44 N/m^2 (or Pa) with which to use for the saltation-abrasion model of

Sklar and Dietrich [2004].

CHAPTER 5: DISCUSSION

From the results, we can garner that a flow acceleration problem explains why erosion scales positively with slope and not at all with discharge; rates of erosion varies consistently with shear stress, and flow acceleration neutralizes the boost to shear stress expected when increasing discharge.

Additionally, the flume is ideal for experiments where we want to keep $F_e \sim 1$, such as isolating how erosion varies with independent control over variables like τ, D_{50}, and bed roughness. We're able to keep $F_e \sim 1$ over a large range of conditions because τ_c^* is very much smaller on a smooth concrete surface than in natural systems [Chatanantavet 2010]. In our comparison with the saltation-abrasion model of *Sklar and Dietrich* [2004], we find that erosion does increase with D_{50} [Figure 71], but we also find that erosion increases almost linearly with τ, rather than decreasing to the ½ power as predicted [Figure 70]. The cause of this is not yet discovered, but perhaps erosion rates are more sensitive to factors that allow a greater component of horizontal velocity to impact the bed instead of calculations of fluid shear stress as suggested by Johnson and Whipple (2010). In fact, *Chatanantavet and Parker [2006]* were able to increase erosion rates by increasing slope and decreasing discharge (holding τ constant), so flipped around, one should be able to find decreasing erosion rates by increasing discharge and decreasing slope.
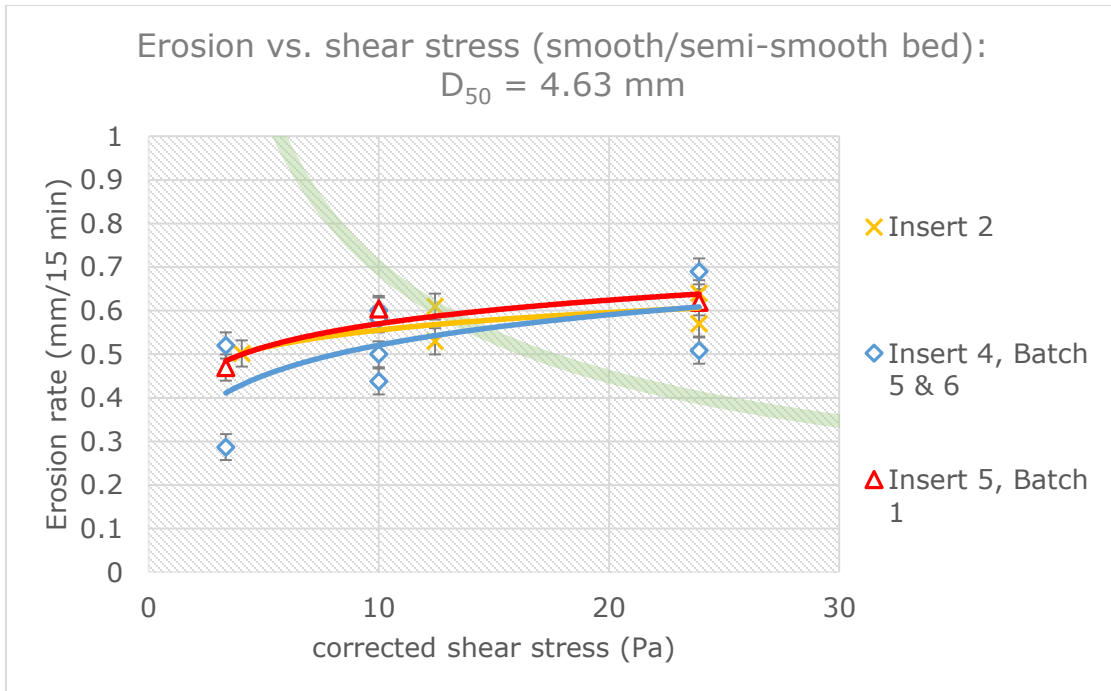
Figure 70: Erosion vs. shear stress on strong concrete with smooth to semi-smooth bed roughness, as compared to the saltation-abrasion model for D₅₀ = 4.63 mm.
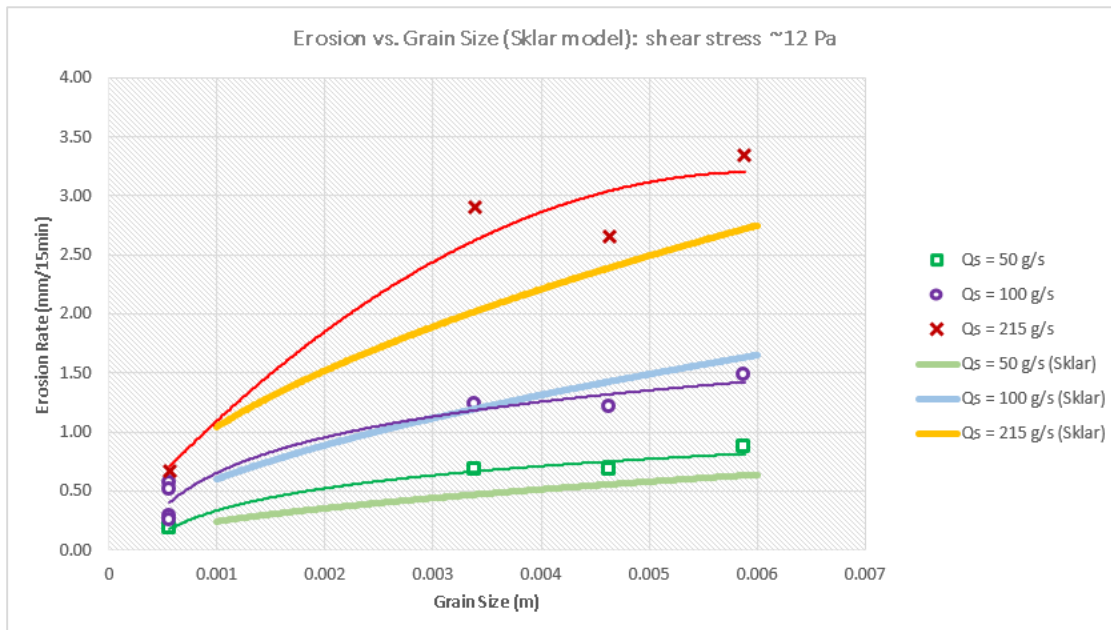
Figure 71: Erosion vs. median grain diameter on weak concrete, compared to the saltation-abrasion model of Sklar and Dietrich *[2004] for* $\tau \sim 12$ *Pa.*

Bed roughness was also found to play an important role controlling that

factors that cause erosion, and in the case of these experiments, greatly decreased

78

erosion rates as it increased (except of experiments of D_{50} = 0.56 mm, where an opposite or invariant trend was often found). Since most of our measures of shear stress were generalized to represent the entire length of the flume, it's possible that lower erosion rates could be a result near-bed shear stress diminishing within the deep, narrow channels found at high roughness, which is of course expected. The unreliable relationship between erosion and bed roughness of the smallest sediment (D_{50} = 0.56 mm) could furthermore be complicated by near-suspended transport of these grains (very high saltation hop length and height) within an incised channel, creating erosion above the bed surface too high for saltation trajectories of the larger grains.

In addition, long duration experiments (30+ minutes) consistently returned values of erosion less (per unit time) than shorter duration experiments, and so there is likely diminishing returns for any sets of experiments where flow conditions are not varied greatly. It is theorized that a bed topography out of equilibrium with flow conditions (i.e. experiment of one extreme of our range of shear stresses followed by another at the opposite extreme) will generally increase erosion rates, as saltation trajectories should have drastically different wavelengths.

The data shows that bedload size is not a very strong control of erosion of bedrock channels between grains of similar size, but there is very positive relationship of E vs. D_{50} between our smallest sand and the larger gravels as a whole. There is also a slightly positive correlation between erosion and grain size at lower flow conditions, but as water speed increases this relationship is diminished. This problem has the opposite result from the possibility that there was some sort of cover effect; if a positive trend between E vs. D_{50} was shown to exist at low flow conditions, increasing flow intensity would only ensure that the largest particles (and hardest to move) are in constant transport along the flume.

If the data for the medium grain size (D_{50} = 4.63 mm) was omitted, the trend between erosion rates and grain size would be much more obvious and more linear. The reason for the dip in erosion rates at this grain size is not well known (or the reason D_{50} = 3.39 had such high values of erosion), and may require further investigation. Every effort was made to run each grain size at similar run conditions and bed topographies to reduce any chance of a false correlation.

CHAPTER 6: CONCLUSION

The flume experiment attempts to recreate a very ideal set of conditions that are not often found in nature. The stream bed is fully exposed; no sediment cover is ever at rest on the surface. The experiments also took into consideration many factors that may have affected erosion rates. Given that flow conditions that created alluvial cover were disallowed, Equation 8 shows that erosion rate was primarily a competition between the vertical component of velocity as a particle impacts the bed (ω_i) versus the saltation length of those same particles (L_b), as the other components of that theory were held constant (or measured between inserts and deemed negligible). This intensity vs. frequency relationship was found to be either favorable to increased erosion rates (when bed slopes were increased) or unchanged (when flow rates were increased) – erosion rate scaled positively with shear stress. Given knowledge of saltation trajectory from *Chatanantavet et al* [2012], it was theorized that increases in bed slope allowed a given transported particle a greater component of velocity normal to the bed, increasing the amount of force per impact, yet our results showed a negative correlation between erosion rates and roughness; something that should've also had that effect.

Conditions were chosen so that the bedload particles would be transported downstream by saltation, in some cases near the transition to suspension, and that the abrasion of these bouncing particles erodes the concrete insert (proxy for a bedrock channel). For the grain size $D_{50} = 0.56$ mm, nearly half of all flow conditions showed Rouse numbers indicating 50% suspension ($2.5 < R < 1.2$), which is thought to be a far less efficient process of abrasion [Sklar, Lamb, Dietrich; 2008], but this was later amended with corrections in shear stress to show there was no degree of suspension at all. Other erosional processes include plucking and cavitation, but our

experiments were designed such that flow and substrate conditions were not conducive to the onset of these processes.

Further testing is required to better understand the role of erosion by suspended sediment. Small amounts of data here shows that abrasion by suspended sediment can be non-negligible, and given its relative abundance in modern rivers, this process may be vital to a better understanding of erosion in bedrock channels.

One attempt of this study was to investigate the effect of suspended load erosion on an exposed bed, but only after extensive experimentation was it realized that most flow conditions used did not fully suspend the sand we had selected. This data was then used to help strengthen the understanding of erosion by particles near the boundary between bed load transport processes and suspension. Had we realized this earlier, we could have increased flow discharge or decreased the particle size intended for suspension, or both. If this was the case, however, I believe we would have extreme difficulty in both the capture of the suspended sediment (without impeding flow) and the prevention of the sediment in traveling to the main water supply, causing an underestimation of real sediment flux in this recirculating system. Both of these were difficult problems that eventually found satisfactory solutions in our not-so-suspended sediment experiments. If changes to the flume in the future could be made to fix this, I suggest that much more success could be achieved if the sediment trap area between the erosive insert and the water supply basin was made dramatically larger (specifically wider). This would theoretically allow the flow to slow down drastically and drop these particles from suspension.

Experimental runs were conducted using only one grain size at a time, and within each there is a small tolerance from the median. In nature, however, there may be a much wider distribution of sizes of sands and gravels (the grain size range this study encompasses) intermingled within the flow. Future work should consider

the role of mixed grain sizes in erosion by abrasion. Another limitation of this study was the occasional heterogeneity of the concrete, apparent only after the concrete was prepared for use (at least 30 days of curing from the time of mixing). These appeared to be cement nodules, possibly resulting from the cement compound not being adequately ground prior to being mixed with the sand. Proper procedure is to break apart the cement clumps by hands when mixing with water, and then adding that slurry to the mixer. The sand is then slowly added, along with a minimum amount of water, while the mixer turns. The cement nodules seem to have little effect on the tensile strength of the concrete, but they do appear to create an increasingly rough topography during suspended-load runs (Figure 72).

Figure 72: Cement nodules within the concrete. Concrete mixes of the same sand: cement ratio showed no significant change in tensile strength with or without these features.

REFERENCES

Aydin, A., & Basu, A. (2005). The use of Brazilian Test as a Quantitative Measure of Rock Weathering. *Rock Mechanics and Rock Engineering*, 39(1), 77-85. doi:10.1007/s00603-005-0069-0

Beer, A. R., & Turowski, J. M. (2015). "Bedload transport controls bedrock erosion under sediment-starved conditions." *Earth Surface Dynamics*, 3(3), 291-309. doi:10.5194/esurf-3-291-2015

Carter, C. L., & Anderson, R. S. (2006). "Fluvial erosion of physically modeled abrasion-dominated slot canyons." *Geomorphology*, 81(1-2), 89-113. doi:10.1016/j.geomorph.2006.04.006

Chatanantavet, Phairot, and Gary Parker (2008). "Experimental Study of Bedrock Channel Alluviation under Varied Sediment Supply and Hydraulic Conditions." *Water Resources Research*, 44 (12). doi:10.1029/2007wr006581

Chatanantavet, Phairot, Kelin X. Whipple, Mark A. Adams, and Michael P. Lamb (2013). "Experimental Study on Coarse Grain Saltation Dynamics in Bedrock Channels." *Journal of Geophysical Research*: Earth Surface 118.2, 1161-176. doi:10.1002/jgrf.20053

Finnegan, Noah J., Leonard S. Sklar, and Theodore K. Fuller (2007). "Interplay of Sediment Supply, River Incision, and Channel Morphology Revealed by the Transient Evolution of an Experimental Bedrock Channel." *Journal of Geophysical Research*, 112 (F3). doi:10.1029/2006jf000569

Johnson, Joel P., and Kelin X. Whipple (2007). "Feedbacks between Erosion and Sediment Transport in Experimental Bedrock Channels." *Earth Surface Processes and Landforms* 32 (7), 1048-062. doi:10.1002/esp.1471

Johnson, Joel P. L., and Kelin X. Whipple (2010). "Evaluating the Controls of Shear Stress, Sediment Supply, Alluvial Cover, and Channel Morphology on Experimental Bedrock Incision Rate." *Journal of Geophysical Research*, 115 (F2). doi:10.1029/2009jf001335

Lamb, Michael P., William E. Dietrich, and Leonard S. Sklar (2008). "A Model for Fluvial Bedrock Incision by Impacting Suspended and Bed Load Sediment." *Journal of Geophysical Research*, 113 (F3). doi:10.1029/2007jf000915

Lamb, M. P., Finnegan, N. J., Scheingross, J. S., & Sklar, L. S. (2015). "New insights into the mechanics of fluvial bedrock erosion through flume experiments and theory". *Geomorphology*, 244, 33-55. doi:10.1016/j.geomorph.2015.03.003

Li, K., Pan, T., Liao, J., & Ku, C. (2014). "Accumulative damage and dissipated energy during saltation abrasion of soft rock – a micromechanics perspective." *Proceedings of the 7th International Conference on Scour and Erosion, Perth, Australia, 2-4 December 2014 Scour and Erosion*, 427-432. doi:10.1201/b17703-53

Scheingross, J. S., Brun, F., Lo, D. Y., Omerdin, K., & Lamb, M. P. (2014). "Experimental evidence for fluvial bedrock incision by suspended and bedload sediment." *Geology*, 42(6), 523-526. doi:10.1130/g35432.1

Sklar, L., & Dietrich, W. E. (1998). "River longitudinal profiles and bedrock incision models: Stream power and the influence of sediment supply." *Rivers over Rock: Fluvial Processes in Bedrock Channels Geophysical Monograph Series*, 237-260. doi:10.1029/gm107p0237

Sklar, L. S., & Dietrich, W. E. (2001). "Sediment and rock strength controls on river incision into bedrock." *Geology*, 29(12), 1087. doi:10.1130/0091-7613(2001)0292.0.co;2

Sklar, Leonard S. (2004). "A Mechanistic Model for River Incision into Bedrock by Saltating Bed Load." *Water Resources Research*, 40.6. doi:10.1016/j.geomorph.2005.08.019

Sklar, L. S., & Dietrich, W. E. (2006). "The role of sediment in controlling steady-state bedrock channel slope: Implications of the saltation–abrasion incision model." *Geomorphology*, 82(1-2), 58-83. doi:10.1016/j.geomorph.2005.08.019

Slingerland, Rudy, and Norman D. Smith (1998). "Necessary Conditions for a Meandering-river Avulsion." *Geology* 26.5, 435. doi:10.1130/0091-7613(1998)0262.3.co;2

Turowski, J. M., Lague, D., & Hovius, N. (2007). "Cover effect in bedrock abrasion: A new derivation and its implications for the modeling of bedrock channel morphology." *Journal of Geophysical Research*, 112(F4). doi:10.1029/2006jf000697

Turowski, J. M., Wyss, C. R., & Beer, A. R. (2015). "Grain size effects on energy delivery to the streambed and links to bedrock erosion". *Geophysical Research Letters*, 42(6), 1775-1780. doi:10.1002/2015gl063159

Ulusay, R. and J. A. Hudson. "Rock characterisation, testing and monitoring. ISRM suggested methods." (1981). *International Journal of Rock Mechanics and Mining Sciences & Geomechanics Abstracts*, 18(6). doi:10.1016/0148-9062(81)90524-6

Whipple, K. X. (2009). "The influence of climate on the tectonic evolution of mountain belts." *Nature Geoscience*, 2(10), 730-730. doi:10.1038/ngeo638

Wohl, E. (2013). Fluvial Geomorphology. In J. F. Shroder (Ed.), *Treatise on Geomorphology* (Vol. 9). Oxford: Academic. doi:10.1016/c2009-1-28399-7

APPENDIX A

MISCELLANEOUS DATA
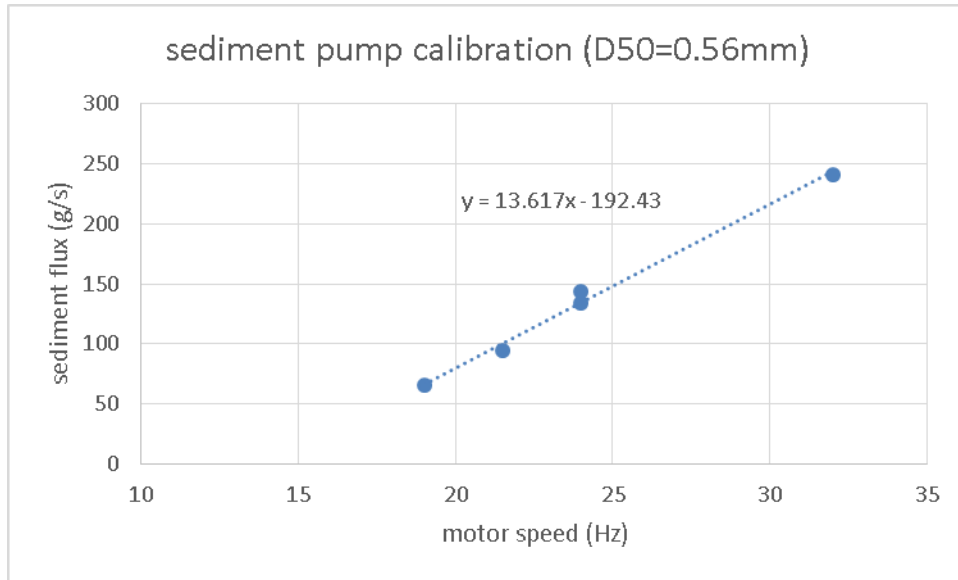
Figure 73: Flux rate for grain unit D_{50} = 0.56 mm is controlled by an electric motor. Sediment flux was calibrated for each grain size.
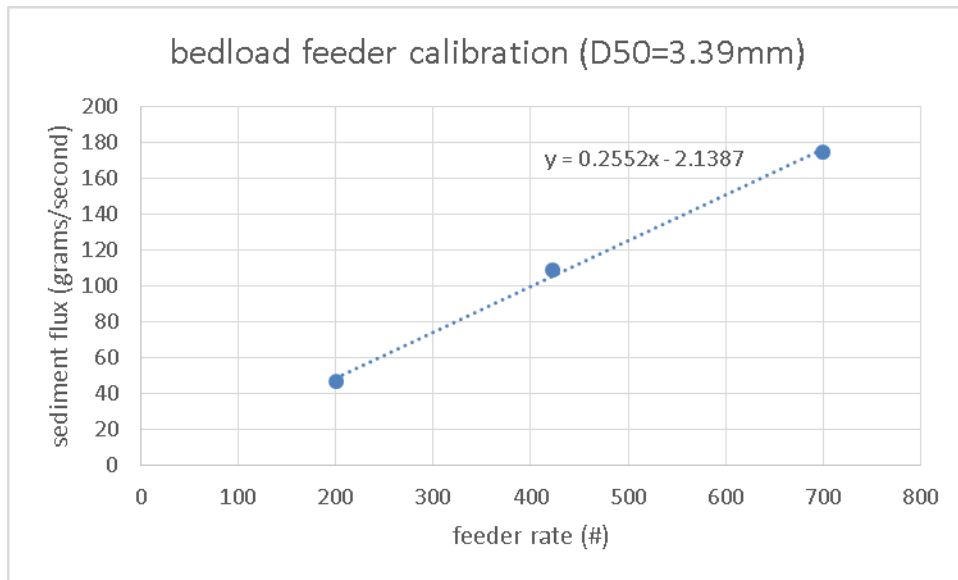
Figure 74: Sediment feeder was calibrated for each grain size. Feeder rate is shown to consistently produce predictable sediment fluxes. Flux rates for grain units D_{50} = 3.39, 4.63, and 5.88 mm are controlled by a sediment feeder controlled independently of flow conditions.
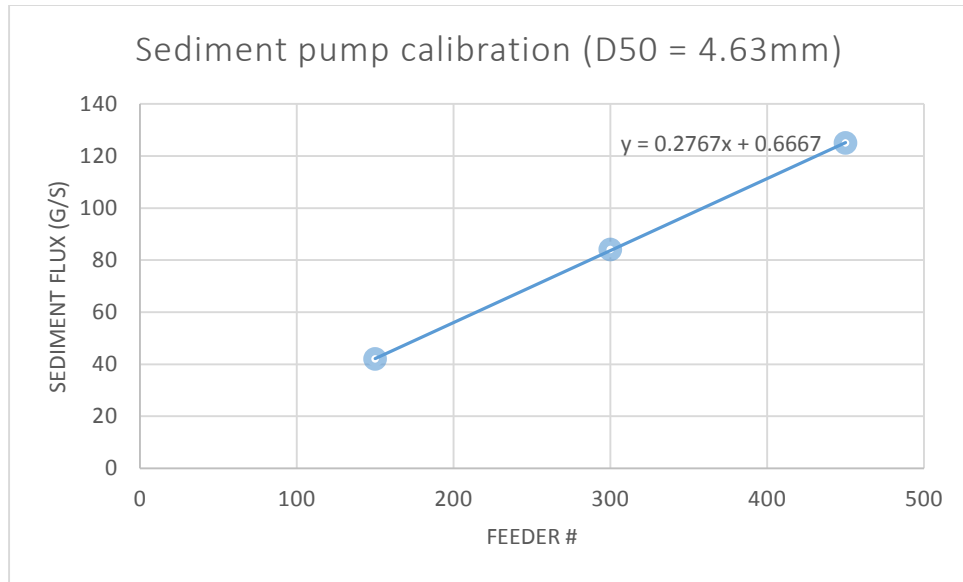
Figure 75: Sediment feeder was calibrated for each grain size. Feeder rate is shown to consistently produce predictable sediment fluxes. Flux rates for grain units D_{50} = 3.39, 4.63, and 5.88 mm are controlled by a sediment feeder controlled independently of flow conditions.
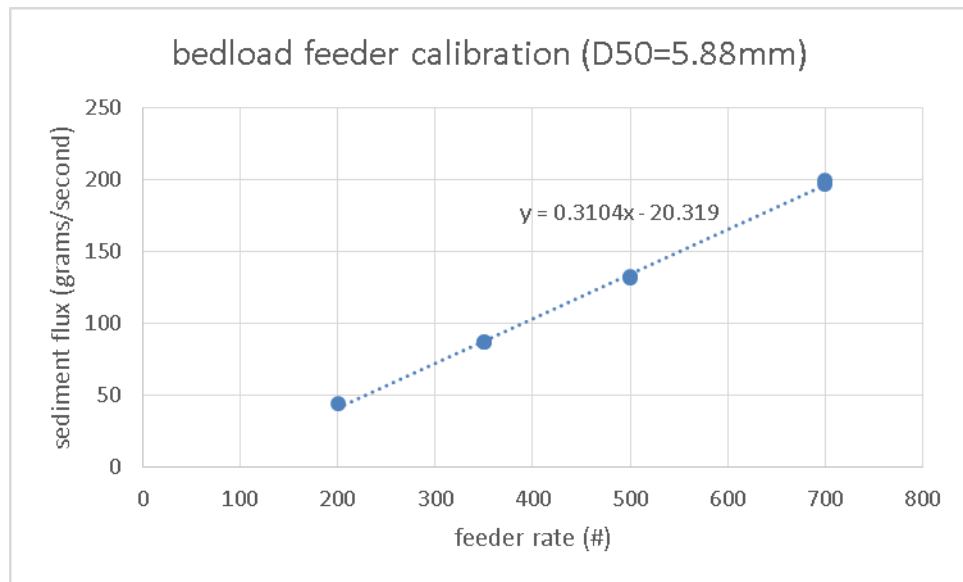
Figure 76: Sediment feeder was calibrated for each grain size. Feeder rate is shown to consistently produce predictable sediment fluxes. Flux rates for grain units D_{50} = 3.39, 4.63, and 5.88 mm are controlled by a sediment feeder controlled independently of flow conditions.

88
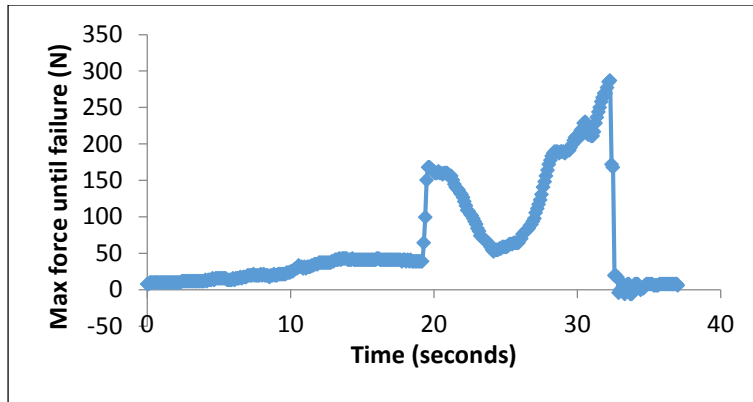
Figure 77: Sample tensile strength test of concrete used as bedrock proxy
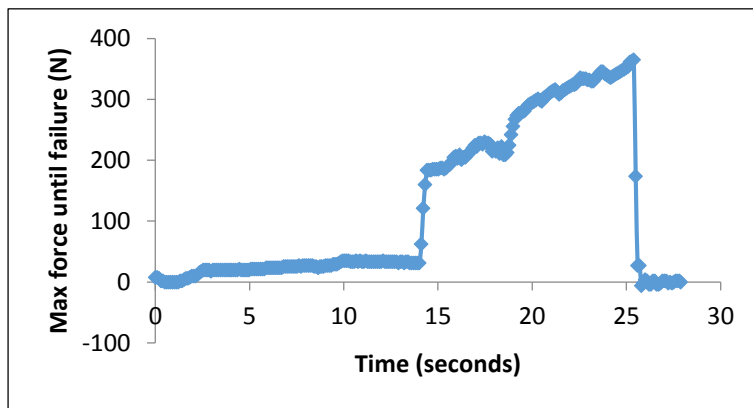
Figure 78: Sample tensile strength test of concrete used as bedrock proxy
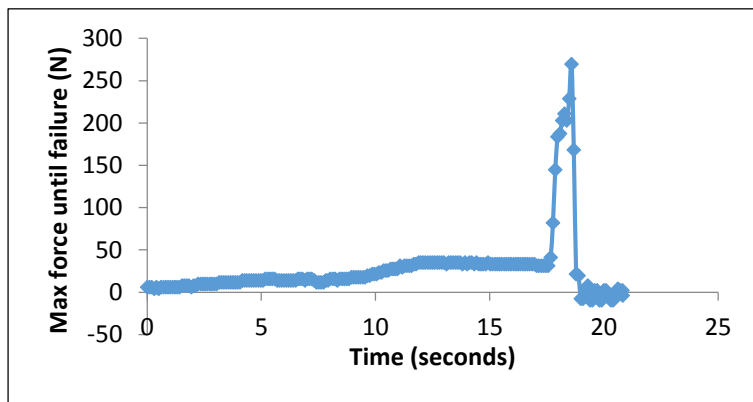
Figure 79: Sample tensile strength test of concrete used as bedrock proxy

89

APPENDIX B

OUTLINE OF EROSION EXPERIMENTS

Figure 80: Outline of Flume Experiments

Insert	Batch	Run	Run time (min)	S	Qw (L/s)	Qs (g/s)	D50 (mm)	Tb (N/m^2)	Roughness (mm)	E (mm/15 min)
1		2	15	0.05	35	100	4.63	10	5.16	0.61
1		3	15	0.05	8	100	4.63	#N/A	5.19	0.60
1		4	15	0.05	18	100	4.63	9.28	5.19	0.65
1		5	15	0.05	55	100	4.63	12.44	5.23	0.53
1		6	15	0.05	35	100	4.63	10	5.31	0.55
1		7	15	0.1	35	100	4.63	22.1	5.39	0.61
1		8	15	0.1	8	100	4.63	#N/A	5.59	0.70
1		9	15	0.02	35	100	4.63	3.91	5.97	0.58
1		10	15	0.02	8	100	4.63	#N/A	6.04	0.47
1		11	15	0.02	18	100	4.63	3.36	6.57	0.64

1		12	15	0.02	55	100	4.63	4.05	7.14	0.62
1		13	15	0.02	35	100	4.63	3.91	7.80	0.60
1		14	15	0.1	18	100	4.63	21.32	8.27	0.72
1		15	15	0.1	55	100	4.63	23.91	8.78	0.73
1		16	15	0.1	35	100	4.63	22.1	9.43	0.72
1		17	15	0.05	35	100	4.63	10	10.19	0.50
1		18	15	0.05	8	215	4.63	#N/A	10.79	0.94
1		19	15	0.05	8	25	4.63	#N/A	11.01	0.15
1		20	15	0.05	8	150	4.63	#N/A	11.83	0.81
1		21	15	0.05	8	50	4.63	#N/A	12.34	0.37
1		22	15	0.05	8	100	4.63	#N/A	13.12	0.62
1		23	15	0.05	8	215	4.63	#N/A	13.56	0.90
1		24	15	0.05	35	215	4.63	#N/A	14.66	1.16

1		25	15	0.05	35	25	4.63	#N/A	14.93	0.18
1		26	15	0.05	35	150	4.63	#N/A	16.07	0.92
1		27	15	0.05	35	50	4.63	#N/A	16.58	0.36
1		28	15	0.05	35	100	4.63	10	17.42	0.63
1		29	15	0.05	35	215	4.63	#N/A	18.51	1.05
1		30	15	0.05	18	100	4.63	9.28	19.35	0.65
1		31	15	0.05	55	100	4.63	12.44	20.12	0.56
1		32	15	0.05	8	100	4.63	#N/A	20.70	0.56
1		33	15	0.05	35	100	4.63	10	21.40	0.60
1		34	15	0.05	18	100	4.63	9.28	22.09	0.58
1		35	15	0.02	35	100	4.63	3.91	22.36	0.37
1		36	15	0.02	8	100	4.63	#N/A	22.42	0.23
1		37	15	0.02	18	100	4.63	3.36	22.67	0.28

1		38	15	0.02	55	100	4.63	4.05	22.99	0.40
1		39	15	0.1	8	100	4.63	#N/A	23.88	0.73
1		40	15	0.1	35	100	4.63	22.1	24.63	0.68
1		41	15	0.1	18	100	4.63	21.32	25.36	0.65
1		42	15	0.1	55	100	4.63	23.91	25.93	0.64
1	-	43	15	0.05	18	100	0.56	9.28	26.31	0.00
1	-	44	15	0.05	8	100	0.56	#N/A	26.30	0.09
1	-	45	15	0.05	13	100	0.56	#N/A	26.32	-0.01
1	-	46	15	0.05	18	50	0.56	#N/A	26.33	0.01
1	-	47	15	0.05	8	50	0.56	#N/A	26.32	-0.01
1	-	48	15	0.05	13	50	0.56	#N/A	26.33	-0.12
1	-	49	15	0.05	18	215	0.56	#N/A	26.31	0.01
1	-	50	15	0.05	8	215	0.56	#N/A	26.32	-0.05

1	-	51	15	0.05	13	215	0.56	#N/A	26.32	0.04
1	-	52	15	0.02	18	50	0.56	#N/A	26.32	-0.07
1	-	53	15	0.02	8	50	0.56	#N/A	26.32	0.01
1	-	54	15	0.02	13	50	0.56	#N/A	26.32	-0.05
1	-	55	15	0.02	18	215	0.56	#N/A	26.32	0.05
1	-	56	150	0.02	8	215	0.56	#N/A	26.34	0.00
1	-	57	480	0.02	13	215	0.56	#N/A	26.38	0.00
1	-	58	30	0.1	18	50	0.56	#N/A	26.42	0.01
1	-	59	20	0.1	8	50	0.56	#N/A	26.41	0.04
1	-	60	15	0.1	13	50	0.56	#N/A	26.44	0.00
2		1	30	0.05	18	100	0.56	9.28		0.01
2		2	30	0.05	18	50	0.56	#N/A		0.02
2		3	30	0.05	18	215	0.56	#N/A		0.04

2		4	30	0.1	18	100	0.56	21.32		0.09
2		5	30	0.1	18	215	0.56	#N/A		0.07
2		6	30	0.1	18	50	0.56	#N/A		0.04
2		7	30	0.02	18	100	0.56	3.36		0.02
2		8	30	0.02	18	50	0.56	#N/A		-0.01
2		9	30	0.02	18	215	0.56	#N/A		0.01
2		10	30	0.05	55	100	0.56	12.44		0.09
2		11	30	0.05	55	50	0.56	#N/A		0.03
2		12	30	0.05	55	215	0.56	#N/A		0.11
2		13	30	0.1	55	100	0.56	23.91		0.06
2		14	30	0.1	55	50	0.56	#N/A		0.04
2		15	30	0.05	35	100	0.56	10		0.01
2		16	30	0.05	18	100	0.56	9.28		0.03

2		17	60	0.1	18	100	0.56	21.32	1.55	0.06
2		18	30	0.05	18	100	0.56	9.28		0.05
2		19	30	0.1	55	215	0.56	#N/A		0.06
2		20	30	0.1	18	215	0.56	#N/A		0.04
2		21	30	0.1	18	100	0.56	21.32		0.01
2		22	30	0.05	18	100	4.63	9.28		0.00
2		23	30	0.1	55	215	4.63	#N/A		0.00
2		24	15	0.1	55	100	4.63	23.91	5.46	0.64
2		25	15	0.01	55	100	4.63	#N/A	5.55	0.77
2		26	15	0.04	55	100	4.63	#N/A	5.69	0.60
2		27	15	0.08	55	100	4.63	#N/A	5.79	0.60
2		28	15	0.005	55	100	4.63	#N/A	6.02	0.61

2		29	15	0.06	55	100	4.63	#N/A	6.25	0.49
2		30	15	0.02	55	100	4.63	4.05	6.47	0.50
2		31	15	0.1	55	100	4.63	23.91	6.61	0.57
2		32	15	0.1	5	100	4.63	#N/A	6.79	0.78
2		33	15	0.01	55	100	4.63	#N/A	7.10	0.57
2		34	15	0.06	7	100	4.63	#N/A	7.34	0.50
2		35	15	0.04	11	100	4.63	#N/A	7.59	0.61
2		36	15	0.08	5	100	4.63	#N/A	7.89	0.65
2		37	15	0.02	23	100	4.63	#N/A	8.23	0.51
2		38	15	0.1	5	100	4.63	#N/A	8.59	0.65
2		39	30	0.05	18	100	0.56	9.28	8.63	0.12
2		40	30	0.05	18	50	0.56	#N/A	8.67	0.04
2		41	30	0.05	18	215	0.56	#N/A	8.71	0.20

2		42	30	0.05	55	50	0.56	#N/A	8.73	0.08
2		43	30	0.1	18	215	0.56	#N/A	8.80	0.31
2		44	30	0.1	18	50	0.56	#N/A	8.85	0.06
2		45	30	0.02	18	100	0.56	3.36	8.84	0.03
2		46	30	0.02	18	215	0.56	#N/A	8.82	0.02
2		47	30	0.1	18	100	0.56	21.32	8.87	0.11
2		48	15	0.005	27	158	4.63	#N/A	8.82	0.18
2		49	15	0.02	56	316	4.63	#N/A	9.42	1.38
2		50	15	0.02	17	275	4.63	#N/A	9.27	0.81
2		51	15	0.02	36	316	4.63	#N/A	9.55	1.28
2		52	15	0.04	47	316	4.63	#N/A	10.34	1.58
2		53	15	0.02	8	100	4.63	#N/A	10.39	0.44

2		54	15	0.02	8	50	4.63	#N/A	10.47	0.17
2		55	60	0.02	8	215	4.63	#N/A	10.35	0.07
2		56	15	0.02	8	25	4.63	#N/A	10.48	0.12
2		57	15	0.02	8	130	4.63	#N/A	10.39	0.32
2		58	15	0.02	8	115	4.63	#N/A	10.33	0.30
2		59	15	0.05	55	100	4.63	12.44	10.77	0.53
2		60	15	0.05	55	100	4.63	12.44	11.40	0.61
2		61	15	0.04	11	100	4.63	#N/A	11.95	0.48
2		62	15	0.1	5	100	4.63	#N/A	12.72	0.74
2		63	15	0.01	55	100	4.63	#N/A	13.10	0.51
2		64	15	0.1	5	100	4.63	#N/A	13.70	0.65
2		65	15	0.01	55	100	4.63	#N/A	14.07	0.55
2		66	15	0.06	7	100	4.63	#N/A	14.69	0.55

2		67	15	0.04	11	100	4.63	#N/A	15.01	0.42
2		68	15	0.08	5	100	4.63	#N/A	15.64	0.49
2		69	15	0.02	23	100	4.63	#N/A	15.88	0.45
2		70	15	0.1	5	100	4.63	#N/A	16.51	0.61
3	1	1	30	0.1	18	100	0.56	21.32		0.02
3	1	2	30	0.1	55	100	0.56	23.91		0.00
3	1	3	30	0.02	55	100	0.56	4.05		-0.09
3	1	4	30	0.05	55	100	0.56	12.44		-0.01
3	1	5	30	0.05	55	100	0.56	12.44		0.01
3	1	6	30	0.05	55	215	0.56	#N/A		-0.06
3	1	7	30	0.05	18	50	0.56	#N/A		-0.07
3	1	7.5	30	0.02	18	50	0.56	#N/A		0.00
3	2	2	15	0.02	55	100	4.63	4.05	6.34	0.26

3	2	3	15	0.02	55	100	4.63	4.05	6.73	0.35
3	2	5	15	0.02	18	50	4.63	#N/A	6.94	0.16
3	2	6	15	0.1	18	50	4.63	#N/A	7.14	0.17
3	2	7	15	0.05	18	50	4.63	#N/A	7.42	0.18
3	2	8	15	0.05	55	50	4.63	#N/A	7.68	0.20
3	2	9	15	0.02	18	215	4.63	#N/A	7.54	0.69
3	2	10	15	0.1	18	215	4.63	#N/A	8.69	1.17
3	2	11	15	0.05	18	215	4.63	#N/A	9.50	0.83
3	2	12	15	0.05	18	215	4.63	#N/A	10.92	1.01
3	2	13	15	0.02	55	100	4.63	4.05	11.34	0.26
3	2	14	15	0.02	18	50	4.63	#N/A	11.66	0.22
3	2	15	15	0.1	18	50	4.63	#N/A	11.95	0.28
3	2	16	15	0.1	18	50	4.63	#N/A	11.97	0.01

3	2	17	15	0.05	18	50	4.63	#N/A	12.48	0.26
3	2	18	15	0.05	55	50	4.63	#N/A	12.91	0.24
3	2	19	15	0.02	55	215	4.63	#N/A	12.64	0.75
3	2	20	15	0.1	55	215	4.63	#N/A	14.18	1.18
3	2	21	15	0.05	18	215	4.63	#N/A	15.19	0.94
3	2	22	15	0.05	55	215	4.63	#N/A	16.61	0.96
3	3	2	15	0.05	18	215	4.63	#N/A	17.00	0.65
3	3	3	15	0.05	55	215	4.63	#N/A	17.97	0.86
3	3	4	15	0.05	55	215	4.63	#N/A	18.99	0.95
3	3	5	15	0.05	55	215	4.63	#N/A	19.99	0.78
3	3	6	15	0.05	55	215	4.63	#N/A	21.01	0.87
3	3	7	15	0.05	55	215	4.63	#N/A	21.97	0.80
3	3	8	15	0.1	18	100	4.63	21.32	22.40	0.48

3	3	9	15	0.1	18	100	4.63	21.32	22.88	0.47
3	4	2	30	0.1	55	100	0.56	23.91		0.20
3	4	4	30	0.1	55	100	0.56	23.91		0.10
3	4	6	30	0.05	55	215	0.56	#N/A		0.14
3	4	8	30	0.05	55	215	0.56	#N/A		0.13
3	4	10	30	0.1	18	100	0.56	21.32		0.07
3	4	11	30	0.1	18	100	0.56	21.32		0.08
3	4	13	180	0.1	18	100	0.56	21.32		0.09
4	5	1	15	0.02	18	100	4.63	3.36	7.29	0.29
4	5	2	15	0.03	25	100	4.63	#N/A	7.73	0.37
4	5	3	15	0.05	35	100	4.63	10	8.13	0.44
4	5	4	15	0.07	44	100	4.63	#N/A	8.53	0.35
4	5	5	15	0.1	55	100	4.63	23.91	8.93	0.51

4	6	1	15	0.05	35	100	4.63	10		0.50
4	6	2	15	0.05	35	100	4.63	10		0.60
4	6	3	15	0.05	35	100	4.63	10		0.58
4	6	4	15	0.02	18	100	4.63	3.36		0.52
4	6	5	15	0.1	55	100	4.63	23.91		0.69
4	7	1	30	0.02	18	100	0.56	3.36		-0.03
4	7	2	30	0.02	18	100	0.56	3.36		0.03
4	7	3	30	0.05	35	100	0.56	10		0.01
4	7	5	30	0.03	25	100	0.56	#N/A		0.03
4	7	7	30	0.07	44	100	0.56	#N/A		0.04
4	8	1	180	0.03	25	100	0.56	#N/A		0.00
4	8	3	180	0.03	25	100	0.56	#N/A		-0.01
4	9	1	30	0.05	35	50	4.63	#N/A	13.06	0.24

4	9	2	30	0.05	35	100	4.63	10	14.70	0.55
4	9	3	30	0.05	35	100	4.63	10	16.28	0.54
4	9	4	30	0.05	35	50	4.63	#N/A	17.14	0.28
4	9	5	30	0.05	35	215	4.63	#N/A	19.68	0.90
4	9	8	30	0.05	35	215	4.63	#N/A	22.27	0.76
4	11	1	30	0.02	18	50	4.63	#N/A	22.74	0.04
4	11	2	30	0.02	35	50	4.63	#N/A	23.21	0.09
4	11	3	30	0.02	55	50	4.63	#N/A	24.16	0.20
4	11	4	30	0.05	55	50	4.63	#N/A	25.12	0.24
4	11	5	30	0.05	35	50	4.63	#N/A	26.09	0.21
4	12	2	30	0.05	35	100	4.63	10	30.07	0.61
4	12	3	30	0.05	35	100	4.63	10	31.69	0.48
4	12	4	30	0.05	35	100	4.63	10	33.10	0.43

5	1	1	15	0.02	18	100	4.63	3.36	6.07	0.93
5	1	2	15	0.03	25	100	4.63	#N/A	6.63	0.81
5	1	3	15	0.05	35	100	4.63	10	7.07	0.60
5	1	4	15	0.07	44	100	4.63	#N/A	7.45	0.62
5	1	5	15	0.1	55	100	4.63	23.91	7.92	0.62
5	1	6	15	0.03	25	100	4.63	#N/A	8.61	0.60
5	1	7	15	0.02	18	100	4.63	3.36	8.79	0.47
5	2	2	30	0.07	35	100	4.63	#N/A	9.56	0.55
5	2	3	30	0.07	18	100	4.63	#N/A	10.74	0.56
5	2	4	30	0.07	55	100	4.63	#N/A	12.24	0.57
5	2	5	30	0.02	35	100	4.63	3.91	12.64	0.32
5	2	6	30	0.02	55	100	4.63	4.05	13.22	0.29
5	2	7	30	0.02	18	100	4.63	3.36	13.28	0.28

5	2	8	30	0.05	55	100	4.63	12.44	14.99	0.57
5	2	9	30	0.05	18	100	4.63	9.28	16.50	0.49
5	2	10	30	0.05	35	100	4.63	10	18.00	0.49
5	2	11	30	0.1	18	100	4.63	21.32	19.43	0.56
5	2	12	30	0.1	55	100	4.63	23.91	20.84	0.54
5	2	13	30	0.1	35	100	4.63	22.1	22.04	0.45
5	3	2	30	0.02	55	100	4.63	4.05	22.60	0.28
5	3	3	30	0.02	18	100	4.63	3.36	22.59	0.22
5	3	4	30	0.02	35	100	4.63	3.91	23.08	0.26
5	3	5	60	0.02	18	100	4.63	3.36	23.08	0.20
5	3	6	60	0.02	35	100	4.63	3.91	23.37	0.16
5	3	7	60	0.02	55	100	4.63	4.05	23.95	0.18
5	4	2	30	0.07	35	100	5.88	#N/A	26.26	0.56

5	4	3	30	0.07	18	100	5.88	#N/A	27.80	0.60
5	4	4	30	0.07	55	100	5.88	#N/A	29.03	0.48
5	4	5	30	0.02	35	100	5.88	3.91	29.63	0.29
5	4	6	30	0.05	35	100	5.88	10	31.01	0.52
5	4	7	30	0.1	35	100	5.88	22.1	32.23	0.50
5	4	8	30	0.05	18	100	5.88	9.28	33.59	0.45
5	5	2	30	0.05	35	100	3.39	10	33.97	0.10
5	5	3	30	0.05	18	100	3.39	9.28	34.33	0.11
5	6	3	30	0.02	35	100	3.39	3.91	48.00	0.67
5	6	4	30	0.05	35	100	3.39	10	48.83	0.61
5	6	5	30	0.02	55	100	3.39	4.05	49.54	0.51
5	6	6	30	0.05	55	100	3.39	12.44	50.29	0.54
6	1	2	30	0.05	35	100	3.39	10	3.73	1.66

6	1	3	30	0.1	35	100	3.39	22.1	4.70	1.79
6	1	4	30	0.02	35	100	3.39	3.91	7.33	1.15
6	1	5	30	0.05	55	100	3.39	12.44	8.34	1.40
6	1	6	30	0.05	18	100	3.39	9.28	12.28	0.74
6	1	7	30	0.02	18	100	3.39	3.36	13.24	0.76
6	1	8	30	0.02	55	100	3.39	4.05	13.32	0.82
6	1	9	30	0.1	55	100	3.39	23.91	14.09	1.65
6	1	10	30	0.1	18	100	3.39	21.32	19.17	1.28
6	2	4	30	0.05	35	100	0.56	10	24.51	0.44
6	2	7	60	0.05	35	100	0.56	10	25.11	0.13
6	3	2	30	0.05	35	100	0.56	10	25.61	0.17
6	3	4	30	0.05	35	100	0.56	10	25.91	0.27
6	3	6	30	0.05	18	100	0.56	9.28	26.44	0.15

6	3	8	30	0.05	55	100	0.56	12.44	26.74	0.17
6	3	10	30	0.05	18	100	0.56	9.28	27.21	0.07
6	4	3	30	0.05	18	100	0.56	9.28	27.50	0.40
6	4	5	30	0.05	55	100	0.56	12.44	27.97	0.64
6	4	7	30	0.05	35	100	0.56	10	28.99	0.44
6	4	9	30	0.02	35	100	0.56	3.91	29.80	0.16
6	4	11	30	0.1	18	100	0.56	21.32	30.29	0.45
6	4	13	30	0.1	35	100	0.56	22.1	31.09	0.56
6	4	15	30	0.02	18	100	0.56	3.36	32.28	0.22
6	4	17	30	0.1	55	100	0.56	23.91	32.79	0.57
6	4	19	30	0.02	55	100	0.56	4.05	34.03	0.24
6	5	3	30	0.05	35	100	4.63	10	34.34	1.40
6	5	4	30	0.02	18	100	4.63	3.36	37.88	0.87

7	1	2	30	0.05	35	100	4.63	10	3.13	1.10
7	1	3	30	0.1	55	100	4.63	23.91	3.81	1.14
7	1	4	30	0.02	18	100	4.63	3.36	5.24	1.12
7	1	6	30	0.05	35	100	4.63	10	7.57	1.39
7	2	2	30	0.02	35	100	0.56	3.91	11.42	0.18
7	2	4	30	0.05	18	100	0.56	9.28	11.47	0.36
7	2	6	30	0.1	18	100	0.56	21.32	12.20	0.55
7	3	3	30	0.05	18	100	0.56	9.28	14.84	0.69
7	3	5	30	0.1	35	100	0.56	22.1	15.65	0.80
7	3	7	30	0.05	55	100	0.56	12.44	16.46	0.72
7	3	9	30	0.02	18	100	0.56	3.36	17.43	0.23
7	3	11	30	0.05	35	100	0.56	10	17.74	0.57
7	3	13	30	0.1	18	100	0.56	21.32	18.52	0.54

7	3	15	30	0.02	55	100	0.56	4.05	19.40	0.29
7	3	17	30	0.1	55	100	0.56	23.91	19.96	0.61
7	3	19	30	0.02	35	100	0.56	3.91	20.80	0.18
7	4	2	30	0.05	35	100	5.88	10	16.94	1.41
7	4	3	30	0.1	55	100	5.88	23.91	19.53	1.30
7	4	4	30	0.02	55	100	5.88	4.05	22.06	1.41
9	2	2	15	0.05	35	100	4.63	10		0.85
9	2	3	15	0.05	35	100	4.63	10		0.81
9	2	5	15	0.05	18	100	4.63	9.28		1.03
9	2	7	15	0.02	55	100	4.63	4.05		0.82
9	3	5	15	0.02	18	100	5.88	3.36	2.92	1.46
9	3	6	15	0.05	35	100	5.88	10	2.95	1.48
9	3	7	15	0.1	55	100	5.88	23.91	2.97	1.48

9	3	8	15	0.05	55	100	5.88	12.44	2.83	1.42
9	3	15	15	0.05	18	100	5.88	9.28		0.00
9	4	2	15	0.05	55	100	0.56	12.44	2.07	1.03
9	4	4	15	0.1	18	100	0.56	21.32	1.40	0.70
9	4	6	15	0.05	35	100	0.56	10	1.41	0.71
9	4	8	15	0.07	35	100	0.56	#N/A	1.28	0.64
9	4	10	15	0.02	55	100	0.56	4.05	0.63	0.32
9	4	13	15	0.05	55	100	0.56	12.44	1.02	0.51
9	4	16	15	0.07	55	100	0.56	#N/A	1.00	0.50
9	4	18	15	0.05	35	100	0.56	10	0.73	0.37
9	4	20	15	0.1	55	100	0.56	23.91	0.92	0.46
10	2	2	15	0.05	55	100	0.56	12.44		0.25
10	2	4	15	0.05	35	100	0.56	10		0.17

10	2	6	15	0.05	18	100	0.56	9.28		0.15
10	2	8	15	0.1	55	100	0.56	23.91		0.22
10	3	2	30	0.05	35	100	0.56	10		0.03
10	3	4	30	0.07	35	100	0.56	#N/A		0.15
10	3	6	30	0.02	35	100	0.56	3.91		0.06
10	3	8	30	0.1	35	100	0.56	22.1		0.19
10	4	2	15	0.05	55	100	0.56	12.44		0.57
10	4	4	15	0.02	55	100	0.56	4.05		0.12
10	4	6	15	0.07	55	100	0.56	#N/A		0.57
10	5	2	15	0.05	55	100	0.56	12.44		0.28
10	5	4	15	0.05	55	215	0.56	#N/A		0.67
10	5	6	15	0.05	55	50	0.56	#N/A		0.18
10	6	2	15	0.05	55	215	3.39	#N/A		2.91

10	6	3	15	0.05	55	50	3.39	#N/A		0.68
10	6	4	15	0.05	55	100	3.39	12.44		1.23
10	7	2	15	0.05	55	215	5.88	#N/A		3.35
10	7	3	15	0.05	55	50	5.88	#N/A		0.87
10	7	4	15	0.05	55	100	5.88	12.44		1.48
10	8	2	15	0.05	55	100	4.63	12.44		1.21
10	8	3	15	0.05	55	50	4.63	#N/A		0.68
10	8	4	15	0.05	55	215	4.63	#N/A		2.66